

Techniques and Software for the
Characterization of the Misalignments of
Canadian-Made ATLAS sTGC Quadruplet
Muon Detectors

John Paul Flores



Department of Physics
McGill University
Montréal, Québec, Canada

November 16, 2021

A thesis presented for the degree of Masters of Science

©2021 John Flores

Abstract

The development of techniques and software for the characterization of the misalignments of Canadian-made ATLAS small-strip Thin Gap Chamber (sTGC) quadruplets during Long Shutdown 2 of the Large Hadron Collider are discussed. Two major methods, the χ^2 minimization method and the matrix method, are explored. Comparisons between the two methods are performed using Monte Carlo methods, and the χ^2 minimization method is chosen as the standard characterization method for the Canadian sTGCs. Misalignment results of the sTGC quadruplets using this method are also presented.

Abrégé

Le développement de techniques et de logiciels pour la caractérisation des désalignements des quadruplés de la “small-strip Thin Gap Chamber” (sTGC) pour ATLAS fabriqués au Canada pendant le “Long Shutdown 2” du LHC est discuté. Deux méthodes principales, la méthode de minimisation de χ^2 et la méthode matriciel, sont explorées. Les comparaisons entre les deux méthodes sont effectuées à l’aide des méthodes de Monte Carlo, et la méthode de minimisation de χ^2 est choisie comme méthode de caractérisation standard pour les sTGC Canadiens. Les résultats de désalignement des quadruplés sTGC qui utilisent cette méthode sont présentés aussi.¹

¹Thanks to Paul Savage and Elizabeth Hughes for assisting with this translation.

Acknowledgements

First and foremost, I'd like to thank my M.Sc supervisor, Prof. Andreas Warburton. He has been an unfailing and consistent supporter since day 1, and this thesis would not be possible without his support. His steady guidance, countless revisions, and enlightening discussions taught me a lot about particle physics, and his patient and stoic disposition provided constant reassurance. Despite his busy schedule, his door and Zoom room were always open. He never gave up on me, and I thank him for that.

I would also like to thank Prof. Brigitte Vachon and Dr. Tony Kwan. Prof. Vachon has been a true inspiration throughout this process, with her encyclopedic knowledge of everything to do with ATLAS and her endless enthusiasm driving the lab forward. Dr. Kwan was always willing to provide an immense amount of assistance, no matter how small the topic, and his steady and meticulous hand guided the lab successfully throughout all of its sTGC testing. The NSW sTGC lab would not be possible without these two individuals.

Dr. Benoit Lefebvre and Waleed Ahmed both contributed to the base software of this thesis. Dr. Lefebvre provided the framework for all of the analysis performed using sTGCs,

while Waleed Ahmed designed the Monte Carlo Simulation program used for testing. Without them, no part of this thesis would have been possible.

I would like to further thank the members of the ATLAS group at McGill, who introduced me to the world of academia. On a more personal note, I'd like to acknowledge John McGowan, Charlie Chen, Luis Pinto, Lia Formenti, Dr. Tony Kwan, and Kyle Amirie (Belle II). These six were true friends as I navigated grad school and made the journey much less arduous. I wish you all the best in the future.

In closing, I would like to thank my parents, Eddie and Zenaida, my grandparents, Roberta and Arnulfo, and my brother, Michael, for their love and support throughout the entirety of my education. And of course, I would thank the staff and students of STA from the 2020 - 2021 school years, particularly the Graduating Classes of 2020 and 2021. I am not sure if you learned anything from me, but I definitely learned a lot from you. To my AP Calculus class, *memento mori*.

Statement of Contribution

The author made no contribution to the work described in the following chapters: Introduction (Chapter 1), Principles of Particle Detection (Chapter 2), The ATLAS Experiment at the LHC (Chapter 3), and sTGC Production and Quality Control (Chapter 4). The Monte Carlo simulation generator detailed in Chapter 5 was developed by Waleed Ahmed.

The author contributed to lab operations between May and August 2019, particularly with respect to setting up quadruplets for cosmic testing. The author developed the matrix method and χ^2 minimization method programs, described in Chapter 5, from templates provided by Dr. Tony Kwan and Dr. Benoit Lefebvre. Furthermore, the experiments in Chapter 6 were performed by the author using cosmics data collected by the McGill NSW sTGC Lab. Finally, the misalignment results and discussion in Chapter 6 and Appendix B were compiled by the author.

Contents

1	Introduction	1
1.1	The Standard Model of Particle Physics	1
1.1.1	Fermions	5
1.1.2	Bosons	8
1.2	Thesis Outline	10
2	Principles of Particle Detection	12
2.1	Particle Interactions	13
2.2	Ionization Detectors	19
2.2.1	Proportional Ionization Counters and Charpak Chambers	21
2.3	Scintillators and Photomultiplier Tubes	25
3	The ATLAS Experiment at the LHC	28
3.1	The Large Hadron Collider at CERN	28
3.2	ATLAS	30

3.2.1	Long Shutdown 2	33
3.2.2	The New Small Wheel	35
3.2.3	Micromegas	37
4	sTGC Production and Quality Control	40
4.1	Small-Strip Thin Gap Chambers	40
4.1.1	Description	40
4.1.2	The Canadian Production Line	43
4.2	The sTGC Lab at McGill	44
4.2.1	The McGill Test Bench	45
4.2.2	Gas Rack	46
4.2.3	Slow Control and State Machine	48
4.2.4	Cosmic Ray Tests	52
4.3	sTGC Construction Non-Conformities	54
4.3.1	Definition and Tolerance	55
5	Developing Methods for Deriving Layer Misalignments	57
5.1	Basic Framework	57
5.1.1	Monte Carlo Modifications	62
5.1.2	Performance Metrics	63
5.2	Matrix Method	65

5.2.1	Derivation	65
5.2.2	Implementation	68
5.3	χ^2 Minimization Method	70
5.3.1	Algorithm Description	71
5.3.2	The χ^2 Functions	72
5.3.3	Implementation and Statistics Experiments	77
5.4	χ^2 Phase-Space Plotter	82
6	Characterizing Method Performance	86
6.1	Statistics Experiments	87
6.1.1	Description of Experiment	87
6.1.2	Results	89
6.1.3	Discussion	89
6.2	Consistency Experiments	91
6.2.1	Methods	92
6.2.2	Results	94
6.2.3	Discussion	110
6.3	Characterization of sTGC Quadruplets using χ^2 Minimization	112
6.3.1	Future Work	118
7	Summary and Conclusion	121

A Gitlab Links	123
B Misalignment Results of Modules	124
C Supplementary Plots	130

Chapter 1

Introduction

1.1 The Standard Model of Particle Physics

The Standard Model is an example of a quantum field theory. Formally, quantum field theories describe the universe and its constituents using quantum fields. These quantum fields are the basis of both matter particles and the interactions between matter. In any given quantum field theory, the interactions between quantum fields are described by a Lagrangian. Terms in the Lagrangian represent the different ways these quantum fields can interact with each other. Excitations of these underlying quantum fields are then interpreted as different elementary particles [2, 3].

The Standard Model describes two main types of elementary particles. Matter and the forces by which they interact consist of fermions and bosons. Bosons come in two types:

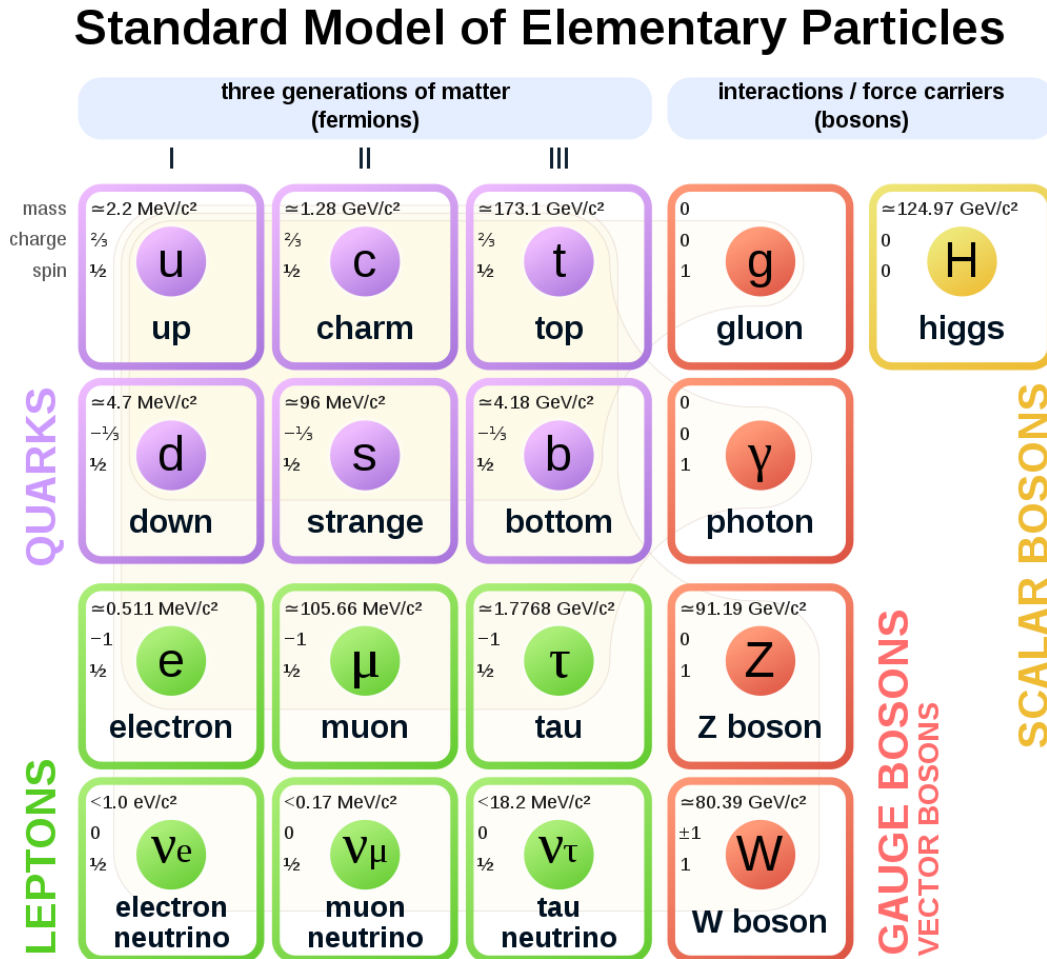


Figure 1.1: The Standard Model of Particle Physics. Three generations of leptons and quarks comprise most of what is thought of as “matter”, while gauge bosons mediate the weak, strong, and electromagnetic forces. The Higgs field, which manifests as the Higgs boson during certain interactions, imparts mass onto massive particles. Gravity is notably absent from the Standard Model. Source: Taken from [1].

force-carrying gauge bosons and the scalar Higgs boson, while fermions also come in two fundamental types: leptons and quarks. Bosons can also be characterized as having integral

spin, while fermions have half-integral spin. Combinations of two or more quarks can also form non-elementary particles, termed hadrons. Hadrons, once again, can be subdivided into mesons and baryons, depending on their quark composition. While hadrons are important particles in and of themselves, quarks and leptons stand as the true “building blocks of nature” according to the Standard Model.

In addition to the elementary particles already described, the Standard Model also predicts the existence of anti-matter. In 1928, Dirac theorized the existence of anti-matter as the negative energy solutions to his eponymous Dirac equation [4]. According to the Standard Model, every charged particle admits a corresponding anti-particle, characterized with the same mass but opposite charge. For example, the electron’s anti-particle is the positron, and the up quark’s anti-particle is the anti-up quark. Some neutral particles, like the neutrino, photon and Z boson, are their own anti-particle. When a particle interacts with its anti-particle, both particles are annihilated, creating a burst of energy carried away as a boson. This boson may then further decay into other particles, such as a Z boson decaying into an electron-positron pair. Anti-particles can also be created pair-wise with their matter counterparts in processes such as pair production, when a photon is in the presence of an atomic nucleus [5].

The Standard Model also accounts for interactions between matter particles. Physicists today recognize four fundamental interactions/forces of nature: electromagnetism, the weak nuclear force, the strong nuclear force, and gravitation. Electromagnetism acts upon charged

particles as classically described by Maxwell's Laws [6, 7]. The weak and strong nuclear forces govern the formation and decay of subatomic particles, such as pions and kaons. Each of these three forces are, in the Standard Model, governed by a gauge boson. Notably, however, gravity is absent from the Standard Model. Despite the enormous efforts of many physicists to unify the Standard Model with gravity [8, 9, 10, 11], there is so far no universally-accepted effective quantum field which describes the action of gravity on matter. Physicists, therefore, turn to Einstein's theory of general relativity.

The theory of general relativity stands as one of the two pillars of modern physics, with the other being the Standard Model. Developed in the 1920s, Einstein's theory describes how the gravitational force can be modelled as the warping of space-time [12]. Massive objects bend space-time, thus causing nearby objects to follow the geodesics of this bent space-time, as if acted upon by an attractive force. In short, as said by John Archibald Wheeler, "space-time tells matter how to move; matter tells space-time how to curve." [13] General relativity, at its core, is a non-quantum theory, as it posits a pseudo-equality between time and space. Quantum theories, however, treat space and time as two distinct objects; therefore, general relativity and quantum theories are generally incompatible with each other. Moreover, in the quantum regime, gravitational forces are extremely small when compared to the other three forces. At the scales relevant to particle physics, general relativity predicts that gravity would have a negligible effect on particle interactions. Modern theories attempting to reconcile the two have yet to gain any traction, due to difficulties in producing falsifiable hypothesis for

testing. Gravity, therefore, does not play a significant role in particle physics [14, 15].

1.1.1 Fermions

Fermions are one class of particles in the Standard Model. All fermions carry half-integer spins and obey the Pauli Exclusion Principle: two fermions may not share the same quantum state. There are two fundamental types of fermions: quarks and leptons. Together, quarks and leptons make up the 3 major subatomic particles: protons, neutrons, and electrons. Some fermions, such as electrons and quarks, carry electric charge, while others, such as the neutrino, are electrically neutral. However, while all fermions interact via the weak force, only quarks are affected by the strong force. The fundamental fermions are divided in three generations each containing two quarks and two leptons, as shown in Figure 1.1.

Quarks compose most of what we often think of as “matter”. The 6 quarks, identified by generation, are up/down, strange/charm, and top/bottom. Different combinations of two or more of these quarks build hadrons. For example, protons are made up of two up quarks and one down quark, while neutrons are made up of one up quark and two down quarks. Protons and neutrons are known as baryons: hadrons that are also considered fermions due to their half-integer spin. Quarks can also form quark-antiquark pairs, known as mesons. Mesons, such as the pion and kaon, have integer spins, and are thus bosonic hadrons. These multi-quark states are held together by the strong nuclear force. Individual quarks are never found in nature; they are always bound in some multi-quark state. This co-dependence,

also known as confinement, is a consequence of the strong nuclear force, which gets stronger as quarks become separated [16]. Should two quarks become sufficiently separated, a new quark-antiquark pair is created from the expended energy.

Quarks also undergo a curious phenomenon known as quark mixing. When quarks decay, they often decay to a same-generation quark (ie. down prefers to decay to up, charm to strange, bottom to top). However, during weak interactions, these quarks can also decay to quarks of a different generation (eg. strange decays to up). Cabibbo first described the mixing of down and strange quarks into up quarks in 1963 [17] (although at the time, the quark model was not fully developed). This result suggests that the quark generations have a potential to “mix” when acted upon by the weak force. In 1973, Cabibbo’s work was expanded on by Kobayashi and Maskawa, who observed that a three-generation model would solve many of the symmetry-violating paradoxes plaguing particle physics at the time, thereby predicting the existence of a third quark generation not discovered at the time [18]. Both the top and the bottom quarks were discovered at Fermilab, with the bottom quark being discovered in 1977 by Lederman et al. [19], and the top quark being discovered in 1995 by the Collider Detector at Fermilab (CDF) and the DØ groups [20]. The relative probabilities of each of the three generations of quarks decaying into one another are codified in the CKM Matrix. For their work on quark mixing, Kobayashi and Maskawa (but notably, not Cabibbo) were awarded the 2008 Nobel Prize in Physics [21].

Leptons, on the other hand, are fermions that do not undergo strong interactions. Like

the quarks, they are separated into three generations. The three generations of leptons are electrons, muons, and tau particles, each with a respective neutrino. Electrons, muons, and tau particles all carry a negative charge, while the neutrinos are neutral (*neutr-* for neutral + *-ino*, a diminutive suffix) [22]. Of the charged leptons, electrons were the first to be discovered, by J.J. Thomson in 1897, providing the first indications that atoms were not indivisible [23].

The three charged leptons most notably differ in terms of their masses and decay times. Electrons are the least massive and most stable of the three charged leptons, with an average lifetime of over 6.6×10^{28} years [24]. Muons were discovered by Anderson and Neddermeyer in 1936 as components of cosmic rays [25]. Their discovery was independently corroborated by Street and Stevenson in 1937 in a cloud chamber experiment [26]. Muons decay much quicker, often decaying into an electron, an electron anti-neutrino, and a muon neutrino in $2.2 \mu\text{s}$ [27, 28]. Finally, the tau particle was discovered by the Stanford Linear Accelerator Center (SLAC) and the Lawrence Berkeley National Laboratory (LBL) in experiments between 1974 and 1977 [29]. Tau particles are very short-lived, lasting only 290 fs [27, 30]. Their large mass, on the order of GeV, is heavy enough to decay into mesons.

Neutrinos behave very differently from their charged leptonic counterparts. As uncharged leptons, they do not interact electromagnetically, interacting solely through the weak nuclear force. There are three “flavours” of neutrinos that match the charged leptons: electron, muon, and tau. While theoretically massless according to the Standard Model, Kahita

and McDonald showed experimentally that neutrinos do in fact have mass. At the Super-Kamiokande neutrino observatory in Japan [31] and the Sudbury Neutrino Observatory in Canada [32], neutrinos were shown to oscillate between the three flavours.

When interacting with the weak force, neutrinos are described to be one of the three flavours of neutrino. In other words, the “electron”, “muon”, and “tau” neutrinos are flavour eigenstates of the weak force. However, as neutrinos propagated through space, the flavour of neutrinos were observed to change. The propagation of neutrinos through space are described via mass eigenstates, while weak interactions between neutrinos and other particles are described in terms of flavour eigenstates. In a manner similar to the CKM Matrix for quarks, these flavour and mass eigenstates are related via the neutrino mixing matrix, U_{li} . In other words, there is no one-to-one association between any given flavour eigenstate and any given mass eigenstate. Current experiments by tritium decay set the upper mass squared limit of the mass eigenstate mostly associated with the electron neutrino to be 1.1 eV [27, 33, 34].

1.1.2 Bosons

Bosons are the other class of particles described in the Standard Model. All bosons carry integral spins, and do not follow the Pauli Exclusion Principle. In other words, they can share quantum states, thus following Bose-Einstein Statistics. Bosons can be further divided into gauge (vector) bosons and the Higgs boson.

Gauge bosons are the spin 1 carriers of the three fundamental forces described by the Standard Model. The electromagnetic interaction is mediated by the photon, while the strong force is carried by gluons. While the photon and gluon are theoretically massless, experiments have set an upper bound of approximately 1.3 MeV [27, 35] on the gluon and 10^{-18} eV for the photon [27, 36]. Finally, the weak nuclear force is mediated by the W^\pm and Z bosons. These gauge bosons are both massive and unstable: the W^\pm boson has a mass of 80.379 ± 0.012 GeV, while the the Z boson has a mass of 91.1876 ± 0.0021 GeV [27, 37].

The Higgs boson is not so much a force carrier but a manifestation of an underlying field, the Higgs Field. Proposed by Peter Higgs and Francois Englert in 1964 [38, 39], the Higgs Field provides a mechanism by which matter particles could have mass. The Higgs boson would be a quantum excitation of this underlying Higgs field, and was discovered in 2012 by ATLAS and CMS independently, to 5.9 and 5.8 sigma significance, respectively [40, 41] at a mass of 125.10 ± 0.14 GeV. The Higgs field is the only known scalar field of the Standard Model, and thus the Higgs boson is the only scalar (spin-0) boson. This discovery by CMS and ATLAS led Higgs and Englert to win the 2013 Nobel Prize in Physics [42].

The interactions between bosons and other matter particles are captured by the Standard Model Lagrangian. While the mathematics of quantum field theories can be dense, a useful heuristic when studying particle physics are the Feynman vertices. The Feynman vertices, shown in Figure 1.2, succinctly list all the potential interactions between the different gauge bosons detailed by the Standard Model. For example, photons (γ) can

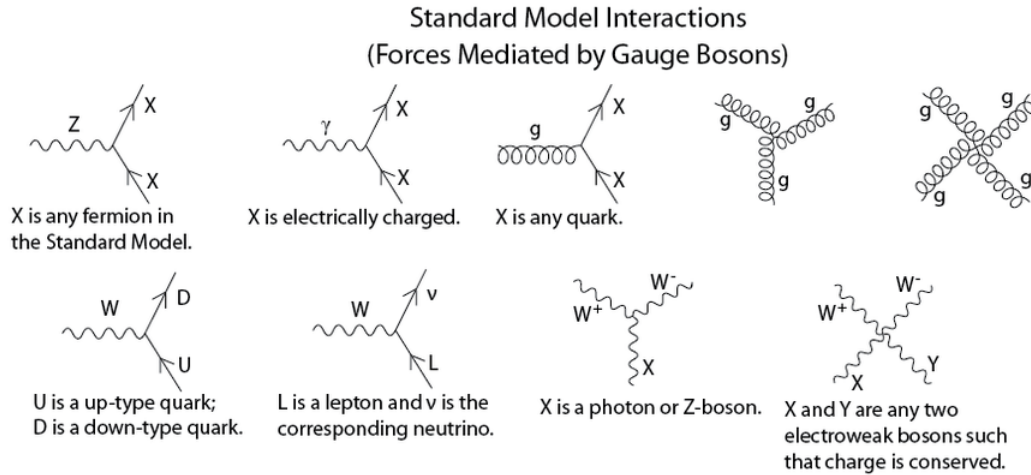


Figure 1.2: Feynman vertices of the Standard Model. These vertices serve as visualizations of the interactions between gauge bosons and matter particles. Adapted from [43].

interact with electrically charged particles, while gluons (g) can interact with quarks. When thinking of potential particle interactions, other considerations, such as charge conservation, lepton number conservation, and spin conservation, must also be taken into account.

1.2 Thesis Outline

In this thesis, the development of techniques and software for the characterization of the misalignments of Canadian-made ATLAS small-strip Thin Gap Chamber (sTGC) quadruplets during Long Shutdown 2 of the Large Hadron Collider is discussed. In this chapter, a brief, non-quantitative overview of the Standard Model was presented. This

provides the basis for Chapter 2, where the principles of particle detection, with reference to models of particle interaction, proportional ionization counters, scintillators, and photomultiplier tubes, will be presented.

The ATLAS Experiment at the LHC will be discussed in Chapter 3, where the motivation behind the small-strip Thin Gap Chamber will be elucidated. Chapter 4 will discuss the production of small-strip Thin Gap Chambers and their quality control testing in the New Small Wheel Lab at McGill University. Of particular interest will be the description of construction non-conformities and measures of misalignment, two of which will be focus points of this thesis.

In Chapter 5, the two fundamental frameworks for determining this misalignment will be derived. The specific implementation of these methods will be discussed, with descriptions of the initial experiments performed during testing. The results from these experiments will provide motivation for the experiments detailed in Chapter 6. Chapter 6 will focus on the experiments that characterize the methods' accuracy, error, and consistency, and ultimately argue for the use of the χ^2 minimization method over the matrix method. The chapter will conclude with the results from the misalignment predictions. Finally, Chapter 7 will provide a brief summary of this thesis.

Chapter 2

Principles of Particle Detection

When studying the Standard Model, physicists are unable to probe the subatomic world as with other physical experiments. In particular, particle physicists often rely not on direct measurement of particles, but on measuring the effects of certain particles on the surrounding material. Thus, a thorough understanding of particle interactions with different media can allow physicists to observe the production and trajectory of particles. Generally speaking, there are five different groups of particles: photons, light charged particles, heavy charged particles, hadrons, and neutrinos. Carefully tuning an apparatus to the observation of one of these five groups can allow experiments to identify particles, shield themselves from background radiation, as well as give accurate information as to the position, momentum, and energy of a given particle.

2.1 Particle Interactions

While travelling through a medium, particles can undergo a variety of interactions with their surroundings. The probability that a given particle undergoes a certain interaction can be quantified using the cross section, often denoted as σ . It is analogous to the classical idea of a cross section in that particles with larger cross-sections will have a greater probability of interacting (ie. colliding) compared to particles with smaller cross-sections. Thus, it is represented in units of area, such as barns (100 fm^2). Because particles can interact with a material via different processes, each process can have its own cross section, again representing the probability a certain process will occur.

As the force carrier of electromagnetism, photons can interact with an absorber material in different ways, depending on the photon's energy and the absorber material. At low energies ($\ll 1 \text{ MeV}$), photons tend to interact with the absorber material by ionizing the material. The ejection of valence electrons by the full absorption of a photon is known as the photoelectric effect, the discovery of which awarded Albert Einstein the 1921 Nobel Prize in Physics [21]. Photons can also elastically scatter off atoms, a process known as Rayleigh scattering [44]. At medium energies (around 1 MeV), photons tend to scatter off atomic electrons inelastically, losing energy but continuing through absorber material. This process is known as Compton scattering [45]. Finally, at high energies ($\gg 1 \text{ MeV}$), photons can undergo pair production. In the presence of atomic nuclei, photons can spontaneously create an electron-positron pair given that the energy of the photon is greater than the mass of the

pair (~ 1.022 MeV). The cross section's dependence on incident photon energy is illustrated in Figure 2.1.

In addition to the energy of the photon itself, the electron density and thickness of the absorber material will also determine how photons will interact. Materials with higher electron density have more electrons per unit volume, increasing the probability of interaction. Electron density tends to increase with atomic number; high- Z materials such as lead are more likely to fully absorb incident photons than low- Z materials such as carbon. A comparison between the overall interaction cross sections of carbon and lead is illustrated in Figure 2.1. Practically speaking, although choosing high electron density materials are one way to ensure photon attenuation, experimentalists can also choose to use thicker layers of absorber materials. Photon attenuation is a probabilistic process, so even a low electron density material can still serve as a radiation shield if there is enough of it.

In contrast, the interactions of charged particles with matter depend on the mass of the charged particle itself; light charged particles, with masses on the order of that of the electron (~ 511 keV) can excite absorber atoms, ionize absorber atoms, and emit Bremsstrahlung radiation (*braking radiation*), Cherenkov radiation, and transition radiation [27, 46]. The excitation and ionization of absorber atoms is attributed to the collision of light charged particles with atomic electrons, exciting them to a higher energy level or “knocking” them out of the atom altogether. Next, Bremsstrahlung is the emission of photons by charged particles accelerating due to the presence of an atomic nuclei, and is the predominant energy

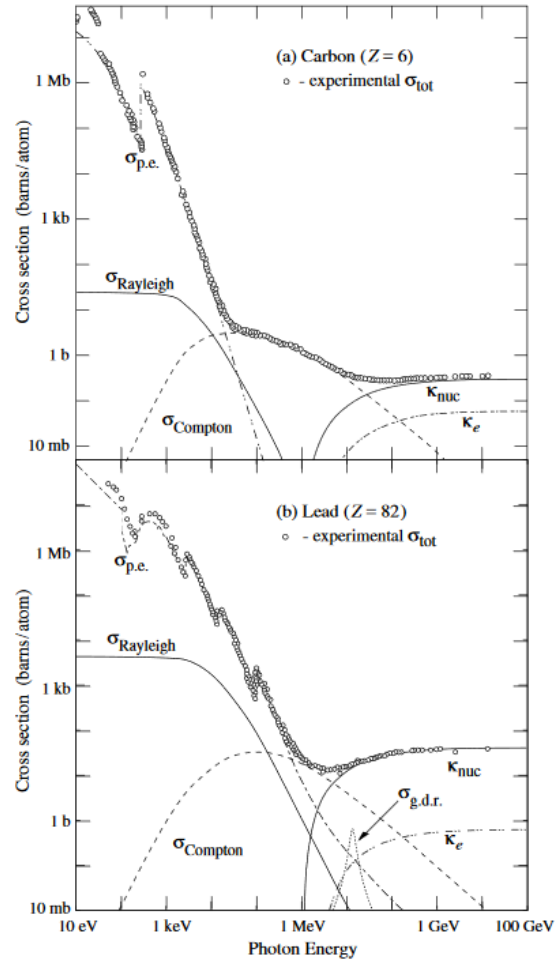


Figure 2.1: (a) Photon cross sections as a function of energy, with carbon as the absorber material. (b) Photon cross sections as a function of energy, with lead as the absorber material. σ and κ represent the cross section: $\sigma_{\text{p.e.}}$ (photoelectric effect), σ_{Rayleigh} (Rayleigh scattering), σ_{Compton} (Compton scattering), and κ_e and κ_{nuc} representing pair production. The photoelectric effect is the predominant interaction at low photon energies, while pair production dominates at high energies. Compton and Rayleigh scattering dominates medium-energy photon interactions. Lead is shown to have generally higher interaction cross-sections than carbon. Source: Figure adapted from [27].

loss mechanism for high-energy electrons [27]. Bremsstrahlung is experienced by all charged particles, but light-charged particles in particular will radiate more due to their smaller mass. In addition to the above, light anti-matter particles, such as positrons, travelling through an absorber can also undergo annihilation with electrons. This effect becomes important at low velocities. Cherenkov radiation is a kind of “electromagnetic sonic boom”, describing the radiation emitted when an electron travels through an absorber material faster than the speed of light in that absorber material. Transition radiation is produced when charged particles travel between materials with different refractive indices. To an observer in the absorber’s reference frame, the transition between two indices changes the velocity of the particle, which can be thought of as apparent acceleration. This apparent acceleration causes the charged particle to radiate. Cherenkov and transition radiation are small contributors to the energy loss of a particle travelling through matter, but can be used for particle identification [47, 48, 49].

Heavy charged particles, on the other hand, are less affected by interactions involving deceleration. Therefore, the main interactions of heavy charged particles (eg. muons, tau particles, protons, etc.) are atomic excitation and ionization. Atomic excitation involves “soft”, inelastic collisions with bound atomic electrons. These bound atomic electrons jump to higher energy quantum states within the atom’s orbitals. If enough energy is transferred between the particle and the electron, the electron (or electrons) may be “knocked” completely out of the atom, ionizing the material and sending out a secondary electron(s).

These secondary electrons and the particle may continue further into the material, ionizing more atoms.

Finally, charged hadrons (eg. protons, charged pions, etc.) undergo all the interactions associated with heavy charged particles, with the additional possibilities of strong force and nuclear interactions. Uncharged hadrons (neutrons, neutral pions, etc.) can interact via the weak and strong forces, in addition to potential nuclear interactions. Low-energy neutrons, for example, drive nuclear fission by colliding with fissile nuclei. The resultant fission ejects, in addition to nuclear fragments, neutrons and gamma ray photons. The sum effect of these interactions on a hadron travelling through an absorber material can be characterized by the nuclear interaction length, λ_I , and nuclear collision length, λ_T , of said material. Neutrinos, as uncharged leptons, interact solely through the weak interaction. Thus, neutrino interactions are very rare and therefore difficult to detect.

The behaviour of different particles through matter can be characterized by stopping power, or energy loss per length. The Bethe-Bloch equation provides a mathematical model for the stopping power of heavy, charged, non-hadronic particles, such as muons. For an incident particle with energy E , travelling a distance x into a medium with a speed v , and charge z , the Bethe-Bloch equation is given as

$$\left\langle \frac{dE}{dx} \right\rangle = \frac{4\pi}{m_e c^2} \cdot \frac{nz^2}{\beta^2} \cdot \left(\frac{e^2}{4\pi\epsilon_0} \right)^2 \cdot \left[\ln \left(\frac{2m_e c^2 \beta^2}{I \cdot (1 - \beta^2)} \right) - \beta^2 \right], \quad (2.1)$$

where $\beta = \frac{v}{c}$ is the speed of the particle relative to the speed of light, m_e is the mass of the

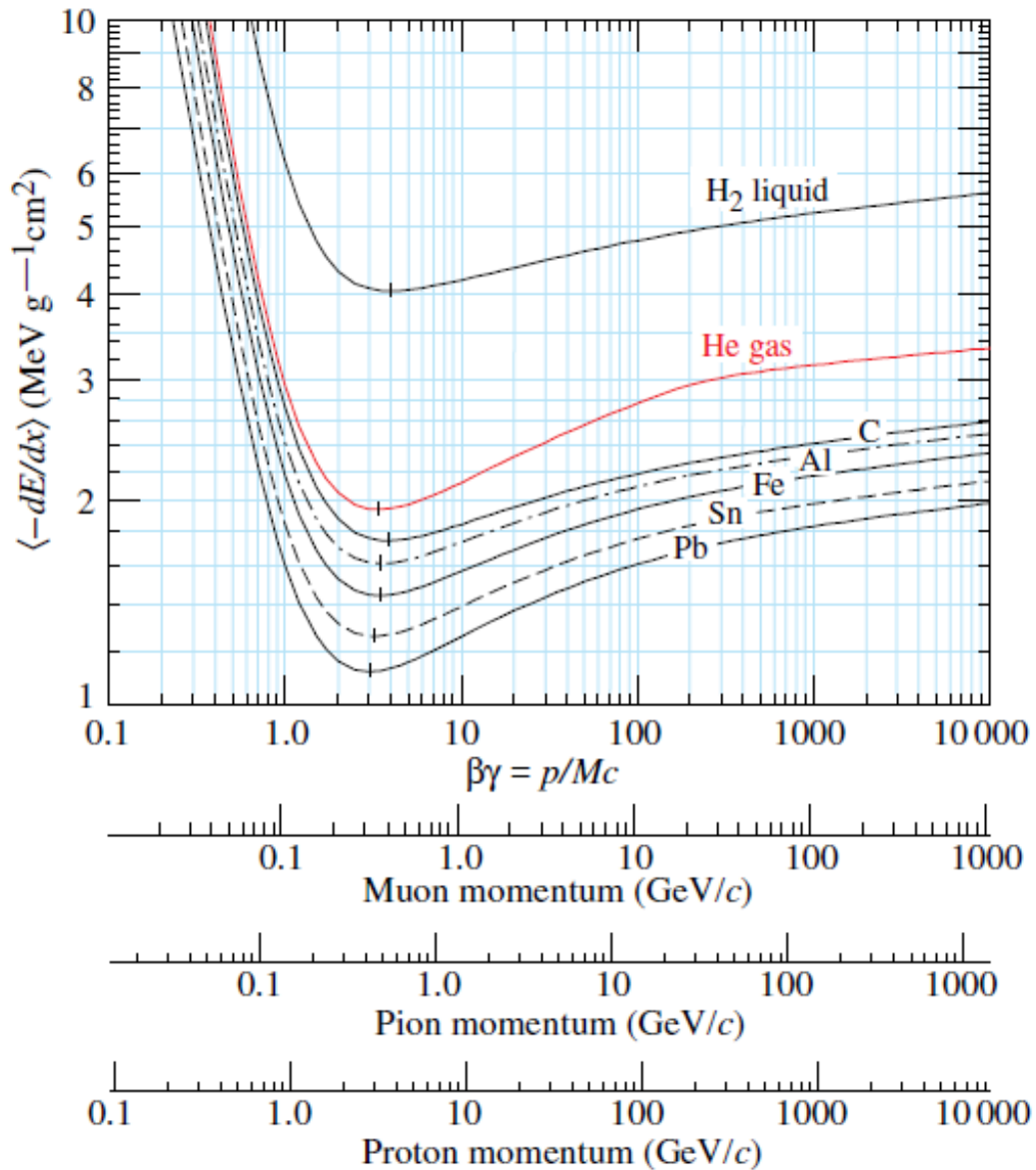


Figure 2.2: Energy Loss per Length of different materials as a function of $\beta\gamma$, according to the Bethe-Bloch equation. The equation provides good agreement with experiment when $\beta > \alpha z$ and up to energies of 100s of GeV. Source: Taken from Particle Data Group [27].

electron, c is the speed of light, n is the electron density of the absorber material, e is the charge of the electron, ϵ_0 is the vacuum permittivity, and I is the mean excitation potential of the target medium. Equation 2.1 is plotted for different interaction media in Figure 2.2. The equation is also independent of particle type [27]. The Bethe-Bloch equation has shown good agreement with experiment when $\beta > \alpha z$, up to energies of hundreds of GeV, where α is the electromagnetic fine-structure constant and z is the charge of the incident particle. The Bethe-Bloch equation also posits that energy loss is independent of incident particle mass. Thus, it serves as a good model of the interactions of heavy, charged particles, such as the muon.

2.2 Ionization Detectors

Understanding how muons interact is essential to the development of muon detectors. How can a physicist take advantage of the known characteristics of a muon travelling through a medium to extract information about said muon? As heavy, charged particles, an apparatus that detects trails of ionization left by muons would provide the best result.

Ionization detectors are detectors that use the remnants of ionization trails to detect heavy, charged particles [46]. They are often gas-tight containers with a well-defined electric field. These electric fields are generated using specific anode and cathode configurations, depending on the desired detector application; additional electrodes may be added to further modify the electric field. When heavy charged particles travel through the detector medium,

they ionize the gas inside the container, creating electron-ion pairs. In the presence of an electric field, these electron-ion pairs drift apart. When electrons hit an anode (or ions hit a cathode), a change in voltage across the electrode is measured. This change in voltage can then be interpreted as a signal for an ionization event. The diffusion rate of the electrons and ions is based on the electric field, the diffusion coefficient of the electron or ion in the chosen gas, and the pressure of the gas. The electrons and ions drift at different rates, with electrons accelerating much faster than ions due to their larger charge-to-mass ratio. If the drift velocities of both the ions and the electrons are known (in addition to the drift length), this difference in diffusion time can provide important positional information as well.

Visualisation of a Townsend Avalanche

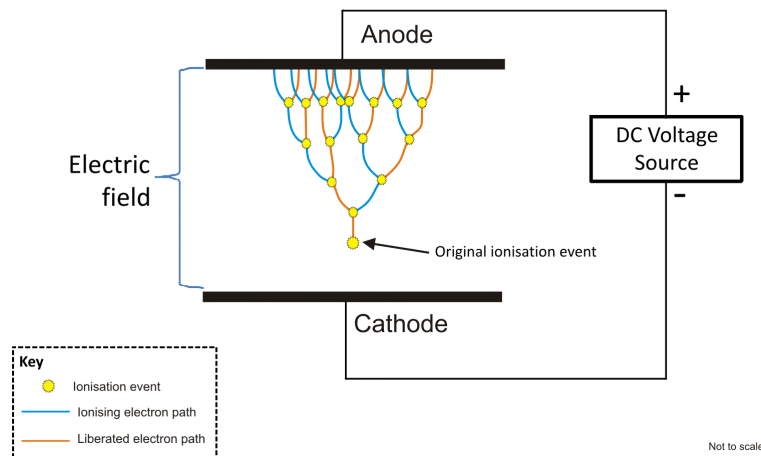


Figure 2.3: A Townsend avalanche, stemming from a single ionization event. The electric field accelerates liberated electrons, leading to more ionization events and increasing the signal. Source: Taken from [50].

The strength of the electric field can lead to avalanche events in a detector. If the electric field strength is increased significantly, liberated electrons can ionize other atoms. This effect can then propagate, causing a significant increase in the number of charge carriers compared to the initial ionization event. This is known as a Townsend avalanche, as illustrated in Figure 2.3 [51, 52]. The ratio of total charge liberated compared to the primary ionization event is called the gas amplification factor, A . This factor tends to increase exponentially with voltage, with some gas detectors reaching $A \sim 10^6$, allowing an initially minute signal to be detected [46, 52].

2.2.1 Proportional Ionization Counters and Charpak Chambers

Proportional ionization counters are ionization chambers that use gas amplification to amplify a signal with a well-defined gas amplification factor [46, 52]. To create a proportional counter, the magnitude of the applied voltage must be carefully considered. If the applied voltage is too low, the Townsend avalanche will not form, leading to weak signals. These detectors are known as ionization chambers. If the applied voltage is too high, all ionization events will lead to a large number of Townsend avalanches, and thus signal proportionality to the initial ionization event is lost. This voltage range is known as the Geiger regime [53]. While there are experiments that may call for one of these other regimes, keeping the signal proportional to the initial ionization events can provide important information that may be lost in other regimes. The range of voltage which

achieves this is known as the proportional regime [46, 52]. The effect of applied voltage on signal strength is illustrated quantitatively in Figure 2.4.

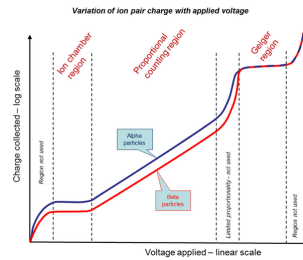


Figure 2.4: Effect of applied voltage on signal strength. As alpha and beta particles have different charges, signal strength differs in the proportional counting region (regime). In the Geiger region, proportionality to the original charge is lost. Source: Taken from [54].

The simplest proportional counter consists of a single anode wire held at high voltage surrounded by a grounded chamber. The electric field is formed by the high voltage applied to the anode wire and is proportional to $\frac{1}{r}$. Electrons liberated by an ionization event will drift towards the anode wire, while ions drift towards the grounded electrode. As the electrons approach the wire, they accelerate due to the increasing electric field of the anode, creating the avalanches that characterize a proportional counter.

In 1968, Georges Charpak, a CERN physicist, linked up multiple proportional counters to create his eponymous Charpak Chambers, also known as multi-wire proportional chambers (MWPCs) [55]. By placing multiple anode wires holding high voltage at regular intervals, a predictable electric field is created. Thus, a larger area could be instrumented with similar or even higher resolution. Charpak's insight was that these anode wires are

not completely capacitively coupled, allowing each anode wire to act as an independent proportional detector. When detecting an ionization event, the main negative pulse of the main anode wire will also induce smaller positive pulses on neighbouring wires, as shown in Figure 2.5. Measuring which wire a pulse is induced on provides positional information in the wire plane perpendicular to the wire directions. The addition of a secondary measurement apparatus (eg. cathode strips/pads) can provide additional positional information in the wire plane, often parallel to the wires.

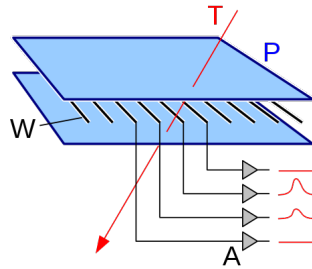


Figure 2.5: A schematic of a multi-wire proportional chamber. W - anode wires, which hold high voltage to create a uniform electric field P - cathode planes, which work in tandem with the anode wires to create the uniform electric field. Cathode strips or pads (not shown) can be added to provide additional information. T - Travelling particle, which creates ionization events to be detected by the chamber. A - amplifier, showing the pulse induced by a travelling particle. Note that pulses are induced in two wires, with the wire closest to the particle trajectory having the higher signal amplitude. Source: Taken from [56].

When designing MWPCs, there are important variables and potential setbacks to be aware of. Because position detection requires a regular, well-understood electric field, the anode wires creating the electric field must be well-aligned [55]. Even a slight wire

displacement will affect the field lines significantly enough to have a measurable effect on spatial resolution and the signal amplitude. For example, for a 5 mm anode wire gap, a displacement (in the out-of-wire-plane direction) of one wire by less than 200 μm and a displacement (in the out-of-wire-plane direction) of all wires by less than 300 μm is acceptable [57]. Furthermore, while one might be tempted to arrange the anode wires as close together as possible to improve resolution, the electrostatic repulsion between wires creates a mechanical limit to how close the anode wires can be placed. Furthermore, wire sagging due to the wire's own mass must also be minimized. To compensate for these effects, wires are often placed under relatively high tension (for their diameter), leading to potential failure points following improper operation. For example, 1 m long, 15 μm diameter anode wire operating at 5 kV and separated by 1 cm between wires must have at least 0.49 N of tension applied to the wire for stability [58]. Wires are usually placed a maximum of 2 mm or more apart to account for this effect [59]. Wire sagging is inversely proportional to the tension applied to a wire; in the above example, applying 0.49 N of tension to the wire reduces sagging to 34 μm [58], which is several orders of magnitude below the anode-cathode distance of roughly 10 mm. Increasing tension accounts for both electrostatic repulsion and sagging, but is limited by the wire's tensile strength.

2.3 Scintillators and Photomultiplier Tubes

Another method of radiation detection is through the use of scintillators and photomultiplier tubes [27]. Scintillators are materials that absorb energy, in this case from radiation, and re-emit that energy in the form of visible light. Common types of scintillators used in particle physics include pure crystals, plastics, noble gases, organic liquids, and organic crystals. Pure crystals are the most widely used scintillators, and are often alkyl halides (such as sodium iodide or cesium iodide). Crystals can also be doped to increase light yield [60]. For example, thallium-activated sodium iodide is often used to detect gamma rays [61]. Organic materials can also serve as scintillators. For example, the KamLAND experiment uses a pseudocumene and dodecane mix to detect neutrinos [62, 60], while the 8pi spectrometer at TRIUMF used plastic scintillators as beta particle detectors [63]. Noble gases can also act as scintillators, emitting photons in the UV range [64, 60].

The photons released by scintillators are often amplified through the use of a photomultiplier tube, or PMT. PMTs convert photons into electric signals through the use of photocathodes and dynodes. Photons striking a photocathode release electrons, which are accelerated through a focussing electrode to a dynode [65]. Dynodes are materials that, when struck by an electron, release more than one electron, depending on the energy of the incident electron. Example materials are beryllium oxide and gallium phosphide [65]. The number of secondary electrons emitted is called the secondary-electron emission coefficient (g). These secondary electrons are then accelerated towards a second dynode, and the

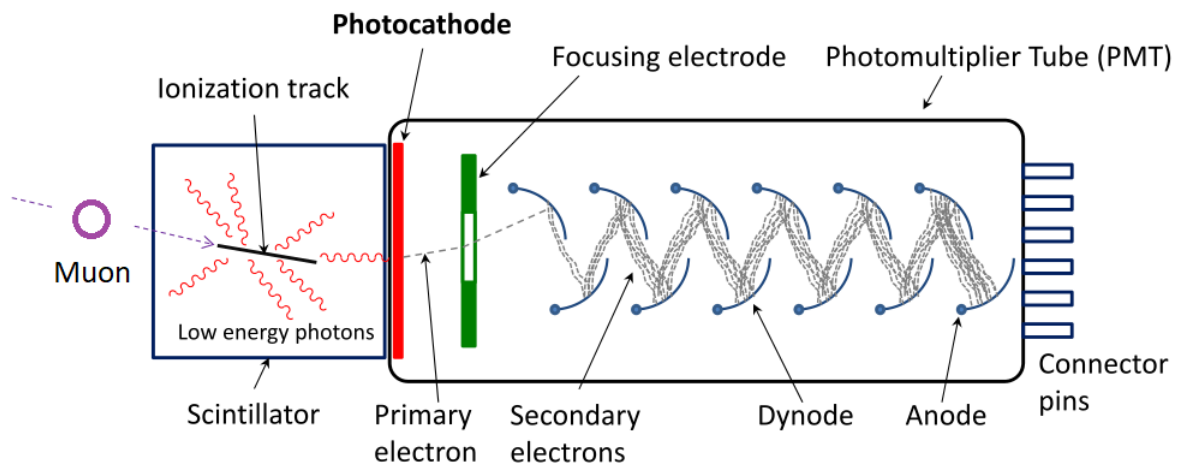


Figure 2.6: (Left) Photomultiplier Tubes. Source: Taken from [65]. (Right) Schematic of a scintillator-PMT array in operation. A muon leaves a track of ionized particles in the scintillator, which is converted to photons. These photons are converted to electrons and amplified in the PMT. Source: Adapted from [66].

process repeats for as many dynodes as there are in the PMT. Thus, the amplification of an n -dynode PMT is $A = g^n$, with a typical amplification of approximately 10^7 [65]. A typical scintillator-PMT array is shown in Figure 2.6.

Due to this exponential amplification, great care must be taken when manufacturing PMTs. Dynodes must have a high specificity, only emitting electrons when struck by incident electrons. The undesirable current that results from thermionic emission of electrons by dynodes is known as dark current and must be minimized as much as possible [65]. At the same time, dynodes must also have a high g -value to achieve a high signal amplification. Furthermore, the combination of scintillators and PMTs necessitates care from the experimentalist's side as well. For example, the system must be isolated from ambient light. Scintillators may fluoresce in response to light, causing false signals to appear. More important, however, is the potential for the amplification of ambient light by the PMT. Moreover, due to the sensitive nature of PMTs, a large number of photons entering a PMT may damage the component irreparably. To remedy this, scintillator-PMT systems are often coated with a visible light-opaque material.

The principles discussed in this chapter will be relevant when discussing the topic of this thesis: measuring the misalignment of small-strip Thin Gap Chamber layers in quadruplets destined for the New Small Wheel of the ATLAS experiment at the LHC.

Chapter 3

The ATLAS Experiment at the LHC

3.1 The Large Hadron Collider at CERN

The Large Hadron Collider (LHC) is a 27.6 km circular particle accelerator straddling the Franco-Swiss border near Geneva, run by the European Organization for Nuclear Research (CERN). Upon its completion in 2010, the LHC displaced Fermilab's Tevatron collider as the world's highest-energy particle accelerator. Its purpose is to explore the Standard Model in the TeV range, with specific hopes to discover the Higgs boson and possible Beyond the Standard Model physics. To this end, the LHC has achieved a 13 TeV collision energy, with an approximate $10^{34} \text{ cm}^{-2}\text{s}^{-1}$ instantaneous luminosity.

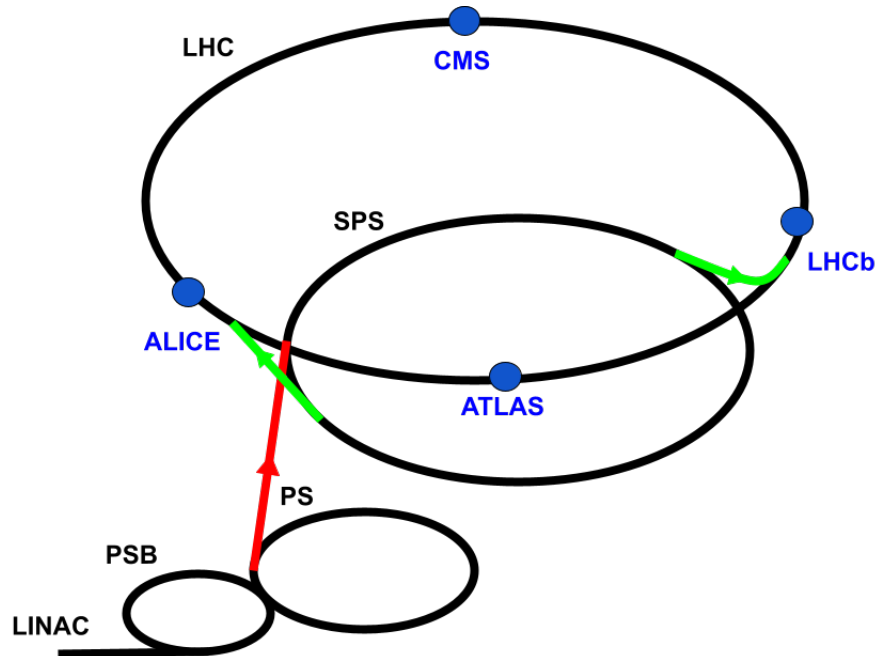


Figure 3.1: (Top) Aerial view of the LHC landscape, with its underground path shown in yellow. Major experiments are labelled. Source: Taken from [67]. (Bottom) Schematic of the path of protons or lead ions from initial injection to the LHC main beam line. The linear accelerator (LINAC) injects protons into the Proton Synchrotron Booster, which is connected to the Proton Synchrotron (PS). The red line connects the PS to the Super Proton Synchrotron (SPS). The green lines each take half of the SPS protons and inject them into the Large Hadron Collider (LHC) in opposite directions. The blue dots on the LHC line are the four major CERN experiments.

The LHC starts by transferring either proton bunches or lead-208 ions into larger and larger accelerators before being injected into the LHC main beam line. Proton bunches start at a linear accelerator (LINAC) and are then injected into the Proton Synchrotron Booster (PSB), the Proton Synchrotron (PS) and the Super Proton Synchrotron (SPS) successively, before being injected into the main beam line of the LHC. This path is traced out in Figure 3.1. The protons accelerated by the pre-LHC complex are split into two beams and injected in opposite directions. While in the LHC, the particles continue to accelerate until they reach the target energy. From there, the proton beams are then focused via magnets to create smaller cross-sectional areas. This increases the chance of interaction when the two proton beams eventually cross over. When the beams are ready to collide, they are redirected for collisions at one of the four major LHC experiments. These four experiments are: A Toroidal LHC Apparatus (ATLAS) [68], the Compact Muon Solenoid (CMS) [69], the Large Hadron Collider beauty (LHCb) [70], and A Large Ion Collider Experiment (ALICE) [71].

3.2 ATLAS

The ATLAS detector [72] is a 7000 ton, $46 \times 25 \times 25$ m³ apparatus, displayed in Figure 3.2. used to probe proton-proton collisions. By centering proton-proton collisions within the main chamber, resultant particles and their decay products can be observed by ATLAS' many calorimeters, radiation trackers, and detectors. Define z to be a cylindrical coordinate in the direction of the beamline, and center the perpendicular r -axis at the point of collision.

Define θ to be the angle from the r axis in the $r - z$ plane. It becomes helpful to define

$$\eta = -\ln \tan \frac{\theta}{2}, \quad (3.1)$$

as the pseudorapidity when referring to the different measurement devices in ATLAS, with technical documents referring to different parts of the detector.

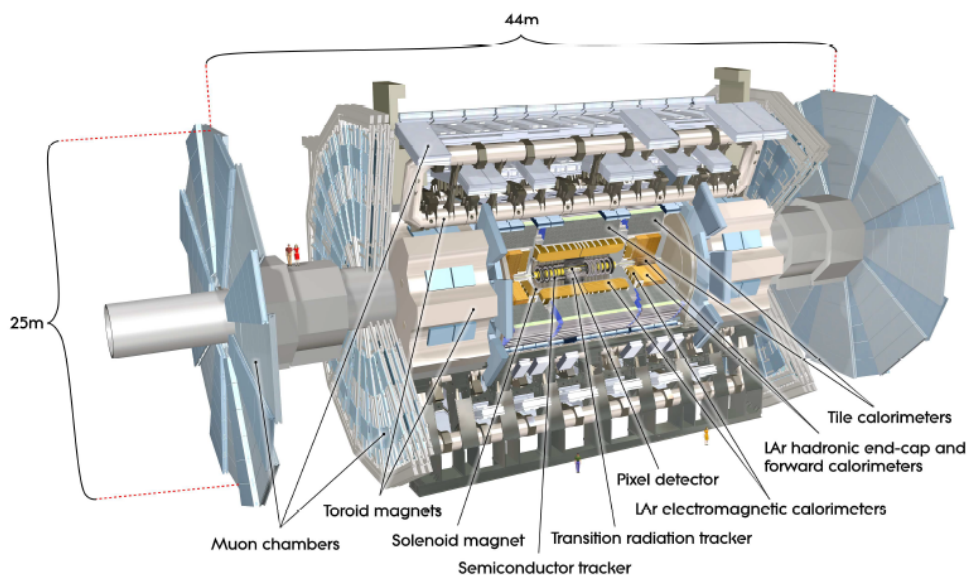


Figure 3.2: Artist's depiction of the ATLAS Detector. Figure taken from The ATLAS Collaboration [73].

While the ATLAS detector comprises multiple different systems, we will focus in this thesis on the muon spectrometer system. The muon spectrometer measures the energy and trajectory of outgoing muons, thus providing data on interactions at the collision point. According to the New Small Wheel Technical Design Report, the muon spectrometer must

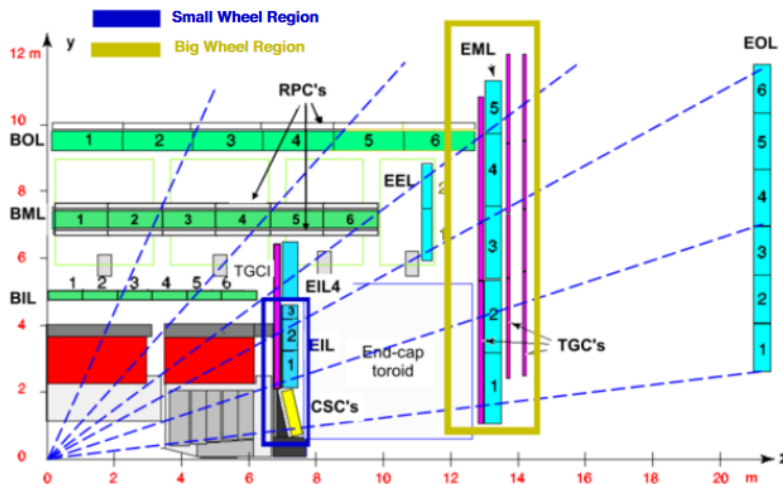


Figure 3.3: Diagram of the distribution of muon detector technologies in ATLAS. Blue dashed lines represent pseudo-rapidity in 0.5 increments. Current Small and Big Wheel Regions are boxed in blue and yellow, respectively. Taken from the New Small Wheel Technical Design Report [74].

have a high efficiency and resolution, and also needs to reject background from non-muon sources. For example, efficiency should be better than 97% for muons with transverse momentum greater than 10 GeV, online track segment reconstruction efficiency should be better than 95%, and the position resolution should be better than 100 μm [74]. The muon spectrometer system comprises three different detector technologies that work together to provide information on muons produced in proton-proton collisions. For $\eta < 1.05$, Resistive Plate Chambers (RPCs) are used to detect muons. For $1.05 < \eta < 2.4$, Thin Gap Chambers (TGCs) are used. To add a layer of redundancy, Monitored Drift Tubes (MDTs) and Cathode Strip Chambers (CSCs) are also used for $\eta < 2.7$. The different muon

detector technologies at the end caps of ATLAS are organized into two “wheels”: aptly named the Big Wheels and the Small Wheels. The setup of the two wheels is illustrated in Figure 3.3.

3.2.1 Long Shutdown 2



Figure 3.4: Timeline of the planned upgrades for the High Luminosity LHC. Source: Taken from [75].

Since its initial runs in 2010, the LHC has performed two data runs. In 2013, the CERN Council formally announced high-luminosity upgrades to the LHC to be a top priority at the European Strategy for Particle Physics [76]. To that end, the LHC has begun the process of upgrading to the High-Luminosity LHC (HL-LHC), as shown by the LHC/HL-LHC Plan

in Figure 3.4. At present (mid-2021), the LHC is in the middle of Long Shutdown 2 (LS2). During LS2, the LHC will be increasing its collision energy and nominal luminosity. Collision energy will increase to either 13.5 TeV (or similar) before being raised to 14 TeV, or collision energy will increase to 14 TeV immediately for Run 3. Nominal luminosity will increase to 350 fb^{-1} . In other words, more high-energy collisions will be happening per second at any given experiment. Consequently, the four major experiments, including ATLAS, must upgrade their apparatus to cope with this increased luminosity.

Several upgrades are planned for ATLAS during LS2 [77]. The scintillation counters on the end cap calorimeters are to be replaced. At $\eta < 1.05$, the Barrel Inner Small (BIS) 7/8 sites, chambers consisting of drift tubes for muon identification, are adding 16 RPC trigger chambers. These new RPCs will have an improved spatial and time resolution when compared to the current RPCs. The MDTs will also be replaced with sMDTs (small Monitored Drift Tubes). These upgrades are all in an effort to cope with the increased luminosity of the LHC.

One of many upgrades the ATLAS collaboration will undertake will be to replace the Small Wheels (SW) of the muon spectrometer. The SW are apparatuses meant to provide a Level-1 trigger to the ATLAS detector. Level-1 triggers are hardware-based signals meant to trigger the event selection and data recording process by various other detectors [78]. Data from the 2012 run (Run 1) suggests that $\sim 90\%$ of muon triggers from the SW are fake, produced by low-energy protons being picked up by the SW [74]. This places its Level-1 muon

trigger rate at 8-9 times the barrel trigger rate, creating inefficiencies. Further extrapolation of the 2012 data suggests that the high luminosity and high energy conditions post-LS2 will be met with lower efficiencies and resolution [74]. The replacement for the SW must also be capable of online track reconstruction for triggering. This means that it should have an angular resolution of 1 mrad or better and an efficiency of 95% or higher. Furthermore, the SW replacement must be very high efficiency for $1.3 < \eta < 2.5$ [74].

3.2.2 The New Small Wheel

In response to these challenges, the ATLAS team has designed the New Small Wheel (NSW). The NSW will completely replace the SW and provide better efficiency and resolution at higher luminosities and energies. The NSW comprise of a combination of small-strip Thin Gap Chambers (sTGCs), and Micro Mesh Gaseous Structure chambers, also known as Micromegas (MM). Micromegas will be discussed in the following subsection, while sTGCs will be described in greater detail in Chapter 4. The New Small Wheel consists of 8 “large sectors” and 8 “small sectors” that coordinate to provide information on a muon’s trajectory through the end-cap.

Several definitions are important to keep in mind. Recall that the r direction is the cylindrical coordinate perpendicular to the ATLAS beam line, while the z direction is parallel to the beam line. Individual chambers are termed “planes”; as will be discussed later, these chambers will be assembled in groups of four to form quadruplets, or “quads” for

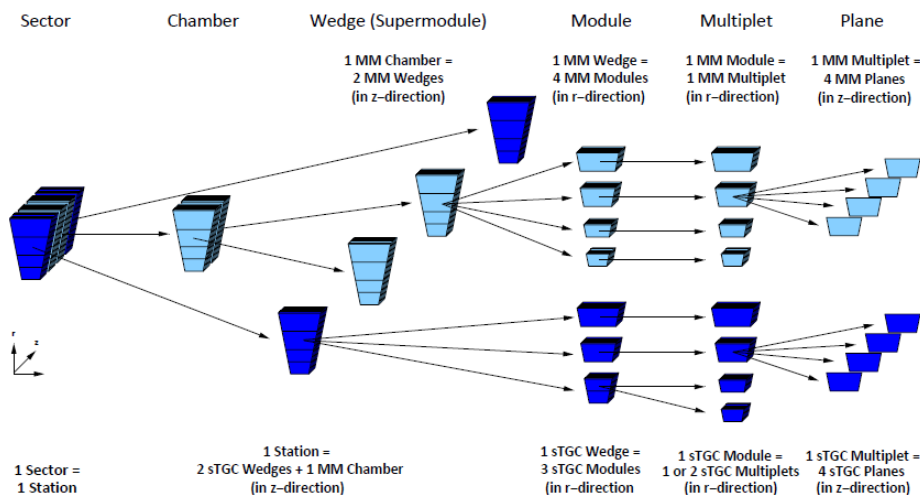


Figure 3.5: Main structural components of the New Small Wheel. Planes/chambers are grouped into multiplets/quadruplets, which are then grouped into wedges. MM and sTGC wedges come together to form a sector. Source: Taken from [74].

short. Groups of two MM quads or three sTGC quads are then connected to form “wedges”, depending on the type of detector. When they are installed into the NSW, two MM wedges are sandwiched between two sTGC wedges (ie. sTGC-MM-MM-sTGC), creating a “sector”. This places the sTGC quadruplets approximately 35 cm apart, allowing for more precise track reconstruction. Depending on their z-distance from the ATLAS interaction point, wedges can also be classified as “confirm” or “pivot”. In order to keep track of produced wedges, quadruplets are named according to four criteria: which sector they belong to, where along the wedge they are placed (with increasing values denoting increasing r-distance from the interaction point), whether they are “confirm” or “pivot”, and their production order. A schematic detailing the breakdown of object types is shown in Figure 3.5.

3.2.3 Micromegas

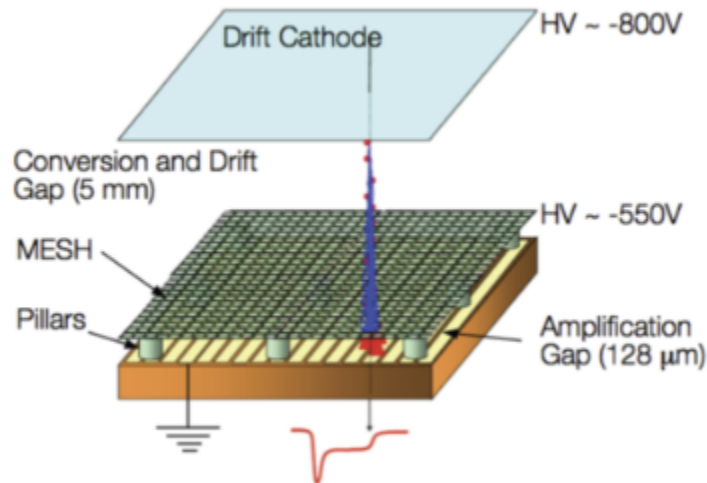


Figure 3.6: Schematic of the working principle of Micromegas. Electrons produced by events in the drift gap are accelerated towards the mesh and amplified in the amplification gap. A Townsend avalanche amplifies the initial signal. Spark-protected Micromegas ground the mesh as opposed to the readout electrodes. Source: Taken from I. Giomataris et al. [79].

Micromegas were first developed by Ioannis Giomataris and Georges Charpak as a high-resolution detector for high luminosity experiments [79]. The structure of a typical Micromegas chamber is shown in Figure 3.6. A relatively large (\sim mm) conversion and drift gap is the site of ionization events. A mesh separates Micromegas' conversion and drift gap from its amplification gap. When a muon travels through the conversion gap, electron-ion pairs are formed, and the electrons travel towards the mesh. After passing through the mesh, the electrons experience a much larger electric field in the amplification gap (\sim μm). The electric field can reach up to 40 kV / cm; this accelerates the electrons

quickly, leading to amplification via a Townsend avalanche. Readout electrodes collect the amplified electrons, and the corresponding ions are evacuated by the mesh.

The advantages of Micromegas are in its resolution and its low lag time. The evacuation of ions from the amplification gap happens on the order of hundreds of nanoseconds, while the spatial resolution is on the order of hundreds of microns. This lag time is quick compared to other technologies, which will be advantageous in the high particle flux environments of the post-LS2 LHC.

The Micromegas that will be installed into the New Small Wheel will also be spark protected. Spark-protected Micromegas are protected in two ways: resistive strips and mesh grounding [80]. Resistive strips are added on top of a thin insulator above the copper collection electrode. Signals are therefore capacitively coupled to the electrode, as opposed to being directly exposed to it. While this decreases signal height, this increases the gas gain at which the Micromegas can be operated. This reduces spark intensities by about three orders of magnitude [80]. Furthermore, in contrast to the old design, spark-protected Micromegas ground the mesh while applying a positive high voltage to the resistive strips. In the previous design, if the mesh was not grounded, the mesh potential would change in the event of a spark, slowing the rate at which ions are evacuated from the amplification gap [80]. This could lead to a signal being induced by the leftover ions in all strips.

As discussed above, Micromegas form one component of the muon chamber wedges that will be installed into the New Small Wheel. The other component, small-strip Thin Gap

Chambers, will be the focus of this thesis.

Chapter 4

sTGC Production and Quality

Control

4.1 Small-Strip Thin Gap Chambers

4.1.1 Description

Small-strip Thin Gap Chambers are variants of the Multiwire Proportional Chambers developed by Charpak. As such, the structure and principles of operation are largely similar. A single sTGC chamber plane consists of three sets of electrodes contained in a gas-tight container, as shown in Figure 4.1. Inside this gas-tight chamber, 50 μm gold-plated tungsten wires with 1.8 mm pitch run through the chamber. Electrode strips are placed on a 1.6 mm thick PCB and positioned 1.4 mm below the anode wire plane.

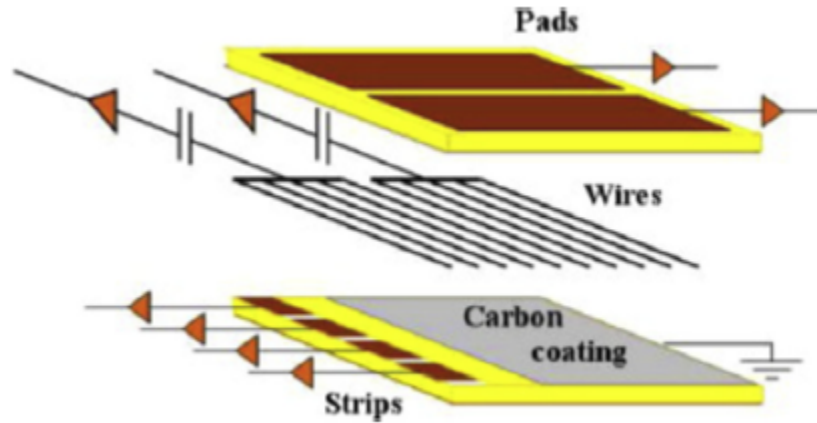


Figure 4.1: The original design structure of small-strip Thin Gas Chambers. Electrons produced by events in the gas are collected by the anode wires. Source: Taken from I. Giomataris et al. [79].

The strips are perpendicular to the wires and are spaced with a pitch of 3.2 mm, much smaller than the pitch of the Thin Gap Chambers already in use in ATLAS (hence “small-strip” TGCs). A 100 μm thick G-10 plane is sprayed with a graphite-epoxy mixture, placed on top of the strips, and grounded. This has the same effect as the resistive strips found in spark-protected Micromegas: it capacitively couples the strips to the signals inside the chamber while reducing sparking. Finally, large rectangular pads are placed at the top of the chamber to provide coarse positional data.

These electrodes work together to produce precision positional information. During operation, the chamber will be filled with a 45-55 pentane- CO_2 mixture (by volume), and the wires will be held at 2900 V. When held at 2900 V, each wire acts like its own independent proportional ionization detector. When a muon passes through the chamber

during operation, the muon will cause a cascade of ionization events. As electrons approach the wires, Townsend avalanches will amplify the signal. The pentane-CO₂ mixture acts as a quenching gas: a gas which absorbs excess photons within the chamber. If photons propagate too far in the chamber, they may trigger Townsend avalanches far away from the initial ionization event, which could be misinterpreted as muon-triggered avalanches. By quenching these photons, signals from muons are suitably localized, thus improving spatial resolution [81]. Ions are evacuated via the grounded G-10 plane while capacitively coupled strip signals give positional information perpendicular to the wires. Together, one plane achieves a spatial resolution of 0.52 mm in the direction perpendicular to the wires (in the wire plane) and 0.92 mm in the direction perpendicular to the cathode strips (in the wire plane).

When referring to sTGCs, a plane is considered to be a single sTGC chamber. In order to construct track information, four of these sTGC planes will be glued together in a quadruplet, or “quad”. When a muon travels through a quad, positional information is read out from each of the four chambers. Because the quads are stacked with a known distance between wire planes, this information can then be used to construct the path of the muon. The pads of the four chambers will then produce coincidence data to complement the track reconstruction. Three out of four pad coincidence is required to positively identify a muon track. sTGCs will be primarily used for Level-1 triggering with 1 mrad angular resolution, which is to be used for quick online track reconstruction to feed the trigger system. The MM chambers discussed

in the previous section will be primarily used for precision offline track reconstruction [74].

4.1.2 The Canadian Production Line

The production of both MMs and sTGCs was an international effort. Micromegas were to be produced in France, Germany, Greece, Italy, and Russia. sTGC modules were to be produced in Canada, Chile, China, Israel, and Russia. Canada was tasked with making 64 quads¹ and 6 spares. In Canada, the University of British Columbia and TRIUMF in Vancouver, British Columbia, prepared the cathode planes. These were shipped to Carleton University in Ottawa, Ontario, where the full sTGC quadruplets were manufactured. Finally, these quadruplets were sent to McGill University for quality control, characterization, and shipment to CERN. Quality control at McGill was performed in the ATLAS sTGC Lab at McGill. The lab was outfitted with a gas rack and test bench, connected to surrounding hardware via Slow Control, custom-built software built with LabView.

Specific quad type requirements were given to each of the participating countries. As alluded to in Subsection 3.2.2, all sTGC quads made for the NSW are named in the form: Q[S/L]X[P/C]YY. [S/L] denote whether the quad is to be used in a “small sector” wedge or a “large sector” wedge. X is an integer between 1 and 3 denoting the r -distance: 1 represents the quad closest to the interaction point in r on the wedge, while 3 represents the quad that is farthest away in r . [P/C] denotes whether the quad is a “pivot” or a “confirm” quad.

¹From this point on, when referring to a “quad”, it is implied that it is an sTGC quadruplet unless otherwise specified.

Finally, YY denotes the production number. For example, QS3P16 is a quad for the small sector wedge as a pivot quad, and it was the 16th QS3P quad to be manufactured. Quads in different sectors and with different r -distances will have different dimensions. Canada's sTGC quads are to be of the QL2C, QL2P, and QS3P variety.

4.2 The sTGC Lab at McGill

At the sTGC Lab at McGill, quads that are manufactured at Carleton University are tested before shipment to CERN. Tests are performed not only to ensure proper physical construction, but also to characterize each sTGC quad under operating conditions. Thus, noise measurements, gas leak tests, and anomalous channel measurements are taken for each sTGC quadruplet. The main method of quality assurance, however, is by way of a cosmic ray test.

During a cosmic ray test, the quadruplet is brought up to operating conditions and set up to detect muons created by cosmic rays. Cosmic rays mimic ATLAS conditions, and during a cosmic ray test, data from roughly 2 million cosmic events are collected over a period of 6 hours. These cosmic rays pass through and are converted to electric signals by the tested sTGC. The electrical signals produced are then fed through Front End Boards (FEBs), which are read out by a field-programmable gate array (FPGA) and subsequently sent to the in-lab computer. Cosmic rays and these tests will be discussed in more detail in Subsection 4.2.4. Cosmic ray tests at McGill are performed in the McGill Test Bench,

a testing apparatus that provides trigger information to the quad and all the necessary auxiliary functions for proper operation. A pentane-CO₂ gas mixture required for operation is provided by the Gas Rack, and the entire system is controlled by Slow Control.

4.2.1 The McGill Test Bench

The main testing apparatus of the ATLAS sTGC Lab at McGill is the Test Bench, also referred to as the hodoscope. The Test Bench, shown in Figure 4.2, is a 2.6 x 2.6 x 2.2 m³ aluminium structure outfitted with four sliding shelves, with the top sliding shelf holding the quadruplet being tested. A forklift is positioned in front of the Test Bench, which assists in positioning the quad in the test bench. The top shelf is also outfitted with fans, connections to high voltage, connections to the gas rack (to be discussed in Subsection 4.2.2) and the KC705 FPGA [82]. This KC705 collects data from the FEBs during testing and sends it to the in-lab computer to be stored in a binary file. The three other shelves hold auxiliary instruments used for testing, including an oscilloscope and an Ethernet modem. The entire structure also serves as a convenient electrical ground when working with ESD-sensitive electronics.

At the top and bottom of the Test Bench are scintillator-photomultiplier tube arrays. Each of these two layers comprises four 160 x 65 x 2.5 cm³ pieces of plastic scintillator connected to PMTs via waveguides. When a muon passes through both sets of arrays, a signal is sent to the KC705 data acquisition system, serving as an external trigger signal

[83].

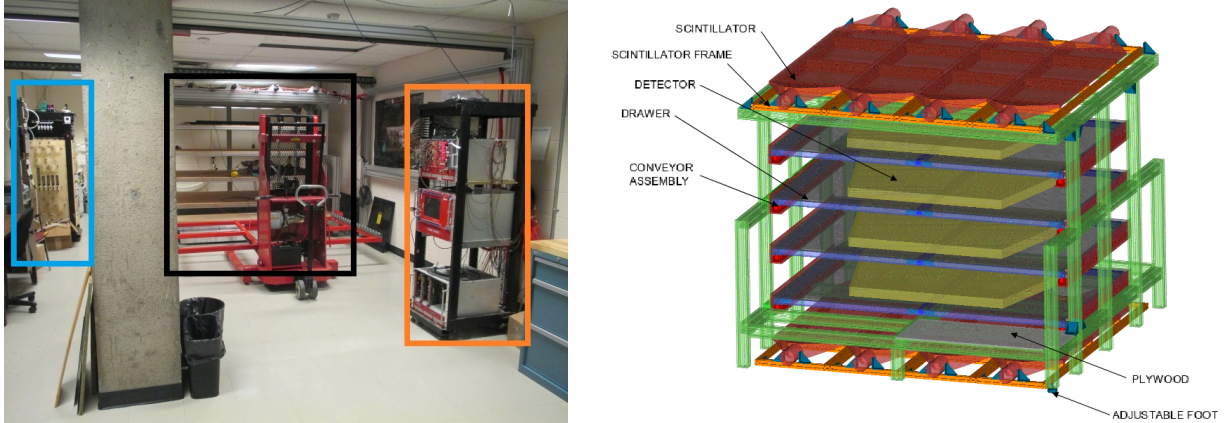


Figure 4.2: (Left) The Test Bench (black rectangle) as seen in the lab. Also visible are the gas rack (blue rectangle) and the NIM crate (orange rectangle) . (Right) Schematic of the Test Bench at McGill Source: Taken from B. Lefebvre (2019) [83].

4.2.2 Gas Rack

The gas rack at the ATLAS sTGC Lab at McGill was developed by Keyes et al. to regulate the pentane-CO₂ mixture used in the sTGC [84]. The gas rack uses a Peltier thermoelectric cooler to provide the necessary pentane concentration required for operation, while a recovery system allows tests to be done safely and with less waste. In addition to providing a pentane-CO₂ mixture to the sTGC, the gas rack can also be set to send CO₂ to the quad, used when flushing the quadruplet before and after testing.

The pentane volume fraction of a CO₂/pentane mixture, as a function of temperature (T), can be calculated via Amagat's and Dalton's laws for ideal gases [84],

$$\text{vol \% (T)} = \frac{V_{\text{pentane}}}{V_{\text{total}}} = \frac{p_{\text{pentane}}(\text{T})}{p_{\text{total}}}, \quad (4.1)$$

where V and p are the volume and pressure of the specified gases, respectively. sTGCs require a 45-55% pentane-CO₂ mixture (by volume) to operate. By assuming atmospheric pressure and using the known vapour pressure of pentane as a function of temperature, any desired volume fraction of the pentane-CO₂ mixture can be achieved via appropriate cooling or warming. To produce this mixture, CO₂ from a tank is connected via dip tubes and bubbling stones to a room temperature pentane tank, known as the mixing tank. Mass flow controllers are positioned at key points in the gas lines. This produces a saturated pentane-CO₂ mixture, which is connected via a quick disconnect pipe to the CP-200 Peltier condenser apparatus. This condenser has a 200 Watt cooling capacity at 0°C. The condenser's cold plate is placed in thermal contact with a copper plate, which in turn is placed in thermal contact with six copper pipes. The saturated gas mixture flows through these pipes, cooling to approximately 14°C. Excess pentane is condensed out and falls back into the mixing tank, achieving the desired 45-55% mixture. This mixture is flushed into the sTGC via four main lines, filling the quad for cosmic ray tests.

During testing, the highly flammable gas is exhausted from the sTGC through a refrigerator. Inside the flammable-proof refrigerator is a recovery vessel held at 0°C. At this temperature, some, but not all, of the pentane condenses out of the mixture, allowing roughly 50% of the used pentane to be recovered. Excess gas is vented outside the building

through an acrylic exhaust box. The exhaust box dilutes the pentane in the mixture before venting it, reducing the flammability of the released gas.

Several important safety measures are also present in the gas rack, to protect the gas system from pressure, pentane, and power outages. A pressure release valve connected to the CO₂ bottle protects the gas system from unexpected pressure spikes, while an over-pressure bubbler connected to the sTGC feed lines maintain the sTGC pressure below 0.5 kPa above ambient. This reduces the likelihood of over-pressure damage to the sTGC and the gas system in general. The pentane recovery tank ensures the safe recovery of pentane, while the dilution box allows vented gas to be below the lower explosive limit of pentane. The nylon tubing and fittings used through the gas system are resistant to chemical attack from pentane, while explosive gas sensors also provide readings and isolate pentane vessels in the event of a pentane leak. Finally, a built-in fail-safe closes all valves if power is lost for any reason. Specifically, the mixing apparatus is isolated in the event of a power outage via solenoids. A diagram of the entire gas system, including safety measures, is shown in Figure 4.3. The combination of these automatic safety measures allows quality control tests to be performed safely within the lab.

4.2.3 Slow Control and State Machine

The sTGC lab is equipped with a slow-control system and state machines, which, in combination with various sensors throughout the lab, allow for both automatic and manual

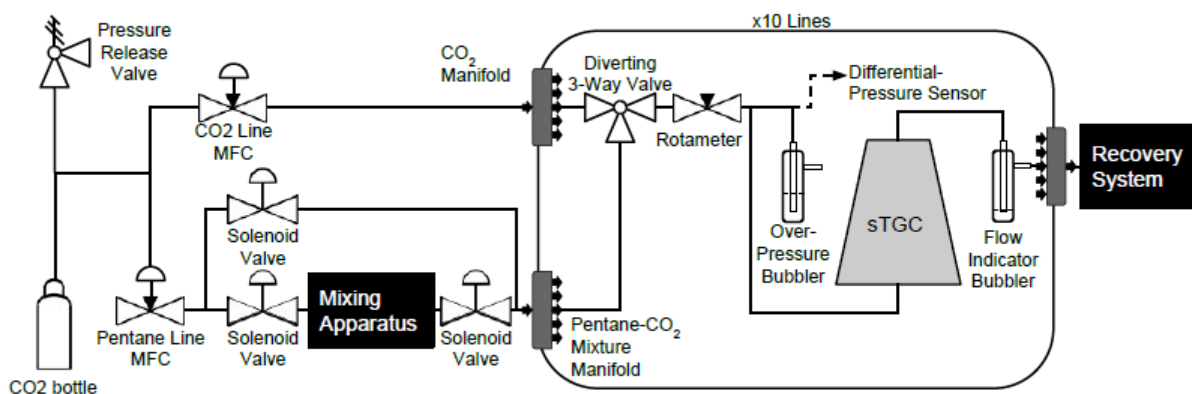


Figure 4.3: Diagram of the Gas System developed by Keyes et al.. The mixing apparatus is mainly driven by a Peltier condenser to achieve the desired pentane concentration. The recovery system allows for the safe recovery and disposal of used pentane. Source: Taken from Keyes et al. (2017) [84].

interaction with the lab environment. The slow control system, which is distinct from ATLAS global slow control, is software which reads environmental sensors to keep track of and respond to different conditions in the gas system. Slow control can trigger safety actions depending on different conditions and can also trigger the emergency pentane tank isolation actions described in the previous section. In addition to allowing users to control gas flow and composition, low voltage power to the FEBs, power to the scintillator-PMT arrays, and high voltage ramp up and down to the sTGC, slow control can also determine when to turn off the voltage supplies or bypass the pentane mixer in the event of a failed testing run. These failsafes allow for safe shutdowns in the event of power outages, as the computer is supported by an uninterruptable power source (UPS). A high voltage/current live plotter, developed by Charlie Chen, used data from slow control to find potential

sparkling within an sTGC during testing. Finally, slow control provides SMS and email messages to operators in the event of errors during operation.

To allow users to quickly obtain information about the operational state of the lab, slow control is connected to a state machine [84] programmed in LabVIEW [85]. The state machines monitor and control a variety of lab variables, including gas flow, power to the scintillator/PMT arrays, high voltage to the sTGCs, low voltage to the FEBs. Via a NIM crate, sensors throughout the lab are also monitored. Three Virtual Instruments make up the state machine: a data acquisition (DAQ) panel, an HV/LV control panel, and a state machine panel. The DAQ panel reads and calibrates raw data from the NIM crate. The HV/LV control panel controls the high voltage/low voltage systems complete with readouts and controls for ramp up and ramp down. The ability for user-defined ramp-up and ramp-down is important when working with sTGCs, where current surges could induce magnetic forces on the wires carrying the voltage, possibly snapping or deforming them. Finally, the state machine panel provides a brief summary of the entire system state, as well as allowing users to control the gas system. Each of the gas rack's ten lines have their own state machine, which allows users to both control and monitor individual gas line flow. Moreover, temperature readings from the FEBs are also displayed on-screen, to ensure temperatures do not exceed 40°C during operation.

Sensors feeding into the NIM crate allow slow control and the state machines to monitor and control the lab. The NIM crate has four input modules and two output modules, assigned

to different parts of the lab environment. These modules are listed in Table 4.1. Most important within the relays is an output module linked to the emergency relay. This relay can be triggered by slow control or directly via the input sensors also plugged into the NIM crate, such as the combustible gas detector or the exhaust flow sensor. The emergency relay isolates both the pentane mixing tank and the recovery tank in the event of an emergency, while simultaneously ramping down high voltage in the sTGC as fast as safely possible. The NIM crate also features a compact DAQ system, which directly measures pressure and mass flow in each of the gas lines, the exhaust flow, and CO₂ bottle pressure, as well as monitoring for potential pentane leaks. In summation, these sensors allow slow control and the state machines to interact with the various parts of the lab, providing not only user interaction but also layers of safety.

Model Number	Description	Input/Output	Associated Components
NI-9203	Current Input Module	20 mA, 200 kS/s, 8-Channel	Gas line pressure sensors; Combustible gas detectors
NI-9205	Voltage Input Module	10 V, 250 kS/s, 16-bit, 32-Channel	MFCs; CO ₂ tank pressure; Exhaust sensor; Emergency relay trip; Humidity / Ambient pressure
NI-9213	Thermocouple Temperature Input Module	78 mV, 75 S/s aggregate, 16-Channel	Solenoid valve temperatures; Gas mixer internal temperature
NI-9217	PT100 RTD Temperature Input Module	0 Ω to 400 Ω , 400 S/s aggregate, 4-Channel	Pentane recovery fridge; temperature
NI-9263	Voltage Output Module	10 V, 100 kS/s/ch simultaneous, 4-Channel	MFC control
NI-9481	Relay Output Module	SPST Relay, 60 VDC (1 A) / 250 Vrms (2 A), 4-Channel	Emergency relay; Peltier system fan; CAEN HV power supply interlock

Table 4.1: NIM Modules used by the sTGC NSW Lab. Source: Taken from [84].

4.2.4 Cosmic Ray Tests

The sTGC lab uses all of the preceding elements to help with the quality control and characterization of sTGC modules. Several tests, such as noise measurements and gas leak tests, are performed with a non-powered sTGC; that is, a module with no high voltage applied. The main test performed during quality control is the cosmic ray test. During a cosmic ray test, the quad is in a fully operational mode, similar to the conditions used in the ATLAS experiment. Cosmic rays serve as the muon source, and data is collected as if the quadruplet was already part of the NSW. Although muons bombard the sTGC at a much lower rate than during ATLAS running conditions, these cosmic ray tests still provide valuable insight that allow quality controllers to characterize the quad's efficiency, dead channels, and misalignment.

Cosmic rays are high-energy protons and other atomic ions that originate from outer space. When interacting with certain parts of our atmosphere, the protons produce many particles which radiate down to earth. In the case of the muon, approximately one muon per square cm reaches the Earth's surface per minute [86]. Although this luminosity is nowhere near the high luminosities generated at the LHC, the muons still provide a well-characterized source of muons that can be used during quality control testing.

Cosmic ray tests begin by priming the quadruplet for operation. All of the following information is available in the McGill sTGC Cosmics Testing Handbook [87]. After loading a quadruplet into the test bench, electronics and gas lines are attached. From the gas rack,

four lines are connected to each of the quadruplet's four layers. High voltage cables from the lab are also attached to the quadruplet's wires. Next, front-end boards (FEBs) are attached to the quadruplet by way of GFZ connectors. The GFZ connectors allow for high-fidelity connection between the adaptor boards of the quadruplet and the front-end boards. Heat sinks are also temporarily attached to the FEBs to keep the operating temperature below 40°C. Fans are also oriented towards the front-end boards for cooling. The FEBs are then attached to a low voltage power source and the KC705. After all the relevant lines are attached, a preliminary volume flush can begin. This overnight preliminary volume flush clears the quad of any air before later perfusing it with the pentane-CO₂ mixture. It also allows for immediate noise tests the following day. Slow control is set to a low flow rate of CO₂ across all lines, and allowed to flush overnight.

The day after a full CO₂ flush, the quadruplet is then filled with the pentane-CO₂ mixture. At least five quadruplet volumes of the pentane-CO₂ mixture are flushed into the quad to ensure that any excess CO₂ from the previous night's flush is removed. Because the QS3 and QL2 quadruplets are different in volume, different amounts of pentane-CO₂ are required for the quadruplets: 17.5 L for QS3 and 24.1 L for QL2. Next, the FEBs are powered on, and the in-lab computers are configured to start data collection. The KC705 is turned on, and measurements of the FEB temperatures are taken to ensure the temperature does not exceed 40°C. If the FEBs and in-lab computer are properly configured, a cosmic run can begin. From the state machine, the high voltage sources to the PMTs are turned on.

The quadruplet HV plotter is also turned on and starts live-plotting the voltage within the quad. With the quadruplet flushed and ready for a cosmics test, high voltage is applied to the quadruplet. A slow ramp-up allows dust and debris to be removed before reaching the target voltages. Tests are performed at 2900 and 3100 V. During each test, eight separate data-taking runs each containing 250 000 events in each layer of the quad are performed. Four are taken at 2900 V and another four are taken at 3100 V, for a total of 2 million analyzed events per sTGC quad. The data is kept in a binary file which must be processed before analysis.

At this point, the raw data from the quad consists solely of signal strengths from each of the electrodes, and must be further processed to provide positional data in a ROOT file. ROOT is an object-oriented program developed by CERN [88] typically used for particle physics analyses. Software produced by Dr. Benoit Lefebvre allows the data to be processed into a ROOT file [83]. The characterization of these sTGC modules and the accompanying software formed the bulk of Lefebvre’s doctoral work. The resultant ROOT file, henceforth referred to as the “processed ROOT file”, contains low-level data for each of the events.

4.3 sTGC Construction Non-Conformities

The ability of an sTGC detector to produce positional information is directly related to its conformity to design parameters. Any potential construction non-conformity can affect the performance of the sTGC and lead to inaccurate results in the New Small Wheel. As

no real-world detector is perfect, one of the main goals of the sTGC lab at McGill is to characterize the degree to which sTGC modules are misaligned.

4.3.1 Definition and Tolerance

Based on Dr. Benoit Lefebvre’s doctoral work [83], there are four major construction non-conformities: a constant offset, pitch scale, non-parallelism, and rotation in the wire plane, as shown in Figure 4.4. To simplify this project, we are focused solely on two specific non-conformities: a constant offset and a rotation. To ensure the desired performance within the New Small Wheel, the quadruplets must conform to certain tolerances. These tolerances are outlined in Table 4.2. The measurement process must be sensitive enough to detect offsets and rotations on the order of these tolerances.

Non-Conformity	Tolerance
Constant Offset	$\pm 75 \mu\text{m}$
Rotation	$\pm 0.004^\circ$
Pitch Scale	$\pm 75 \mu\text{m}$
Non-Parallelism	$\pm 75 \mu\text{m}$

Table 4.2: Construction Tolerances on Non-Conformities for Quadruplet Assembly. Source: Taken from B. Lefebvre (2019) [83].

The decision to exclude non-parallelism and pitch scales is for two reasons. First, because layers are glued into doublets first before being glued into quadruplets, it stands to reason that these doublets may be rotated and offset with respect to each other when glued together. In short, these linear effects are more likely to occur due to simple manufacturing error, while

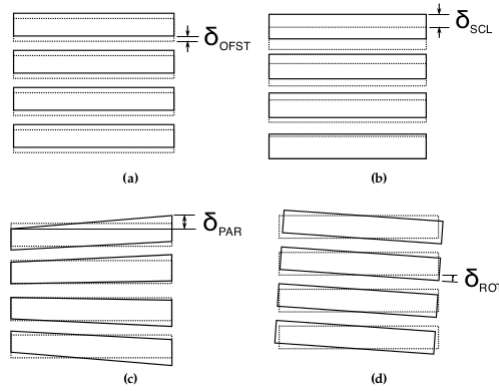


Figure 4.4: Four types of sTGC non-conformities. Displayed in dotted lines are the proper positions of a layer’s strips when perfectly aligned, while the solid lines are the positions after some misalignment by δ . Constant offset (a) and rotation (d) assume layers are perfectly constructed, but misaligned when glued together, while pitch scale (b) and non-parallelism (c) are non-conformities internal to the quadruplet’s layer. Source: Taken from B. Lefebvre (2019) [83].

non-parallelism and pitch scales require other specific internal structures to be misaligned. In this case, it is unlikely for these misalignments to be global. Secondly, non-parallelisms and pitch scales are non-linear effects that are more difficult to model and characterize. Methods to conduct a proper study of these effects are discussed in Chapter 7.

Chapter 5

Developing Methods for Deriving Layer Misalignments

5.1 Basic Framework

When a muon passes through the four layers of a quadruplet, the quadruplet registers a hit on each layer, as shown in Figure 5.1. However, assuming that the muon follows a linear path through the quad, if one layer is misaligned, the hit on the misaligned layer will be registered at a different point, as shown in Figure 5.2. To determine the degree of misalignment on an sTGC quadruplet, two layers must act as reference layers. These two layers are considered to have no misalignment; thus, its data points can be used to construct tracks. For any given layer, l , define an n -point track to be the track constructed using n layers, two of which

must be the pre-defined fixed layers. 3-point tracks use the three non- l layers, while 4-point tracks use all four layers, including l .

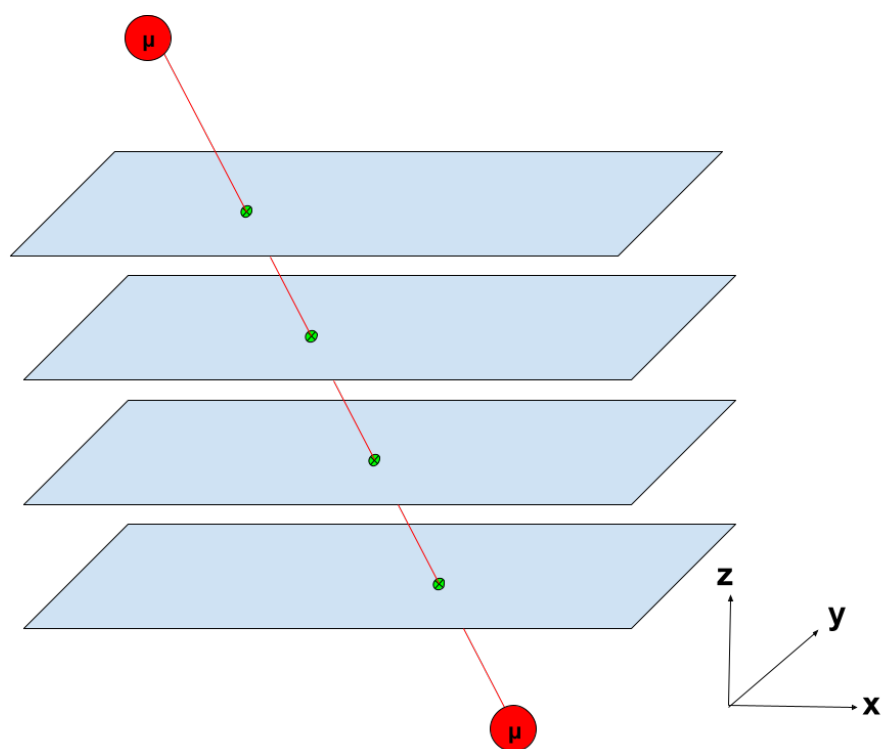


Figure 5.1: A muon (red) travels through four small-strip Thin Gap Chambers (blue parallelograms), which is recorded as a hit by each chamber, represented by the green dots. The hits can then be used to reconstruct the muon's track.

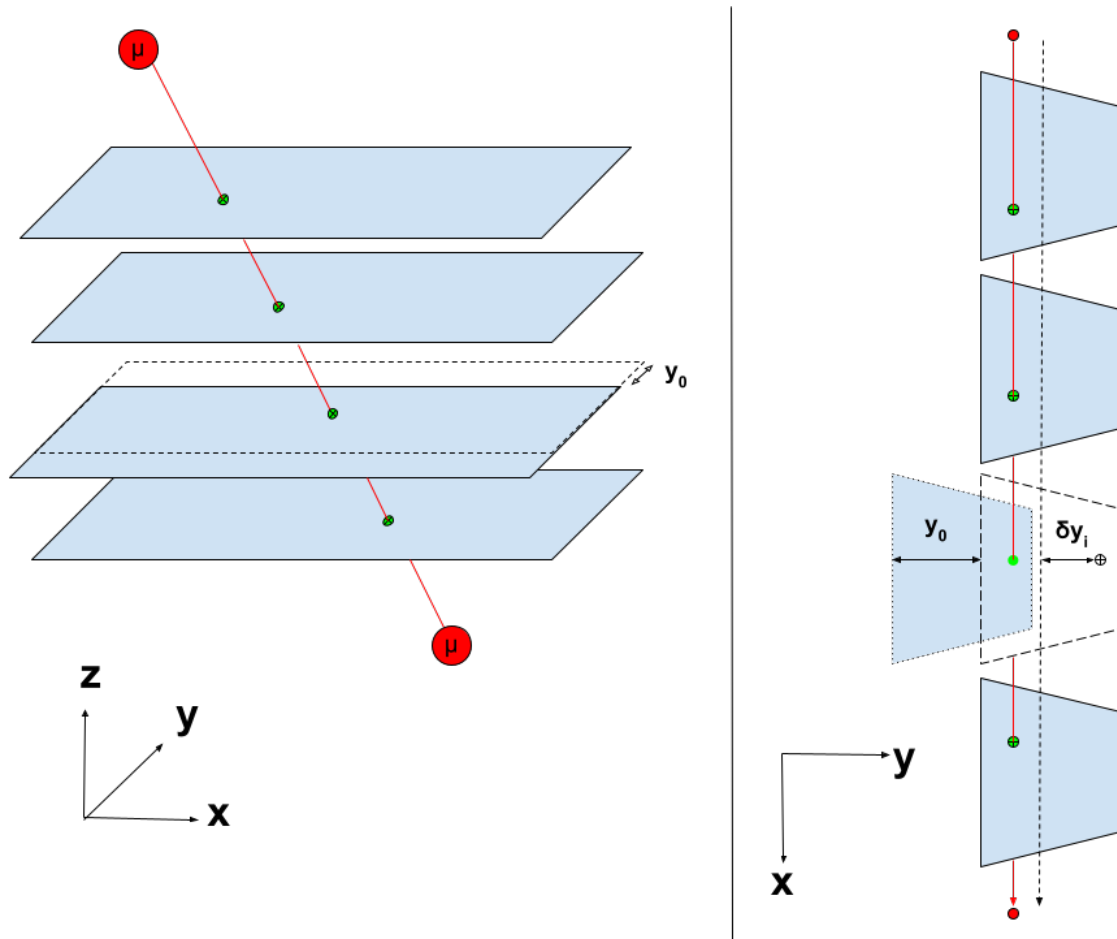


Figure 5.2: (Left) A muon travels through four small-strip Thin Gap Chambers (sTGCs), where the third layer is offset by y_0 . The information from the third layer is displaced with respect to the rest of the gaps. (Right) The same muon travels through four sTGC layers, with the chambers blown apart and the third layer displaced by y_0 . Here, the proper positioning of the third layer is marked by the dashed trapezoid. The spot where the muon should be registered on a properly positioned third layer is marked in green, while the spot where the muon is registered by the displaced layer is marked by the black \otimes . The vertical dashed line shows the best fit line created by the four hits, and the residual is given by δy_i .

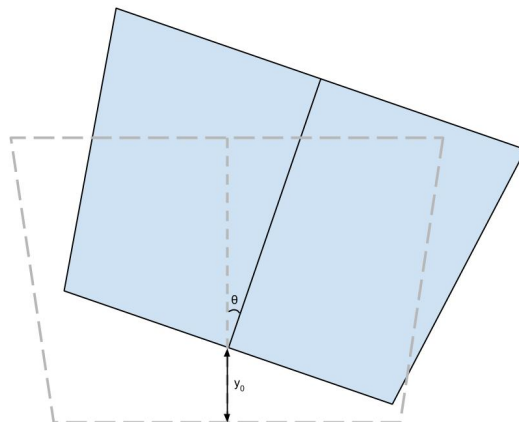


Figure 5.3: A sTGC layer displaced by y_0 and rotated by angle θ in blue, with the proper position in grey, dashed lines.

At the event level, we define a residual, δy_i for a given layer, l , as the difference between the y -coordinate of the i th data point and the y -coordinate of the reconstructed track for that layer

$$\delta y_i = y_{\text{data}} - y_{\text{track}}, \quad (5.1)$$

where y_{data} is the y -position of the hit measured by that quadruplet layer and y_{track} is the y -position predicted from the reconstructed track. An inclusive residual uses a 4-point track, while an exclusive residual uses a 3-point track. Misaligned layers can pull the track fit away from the true values, causing aligned layers to read non-zero residuals. Thus, residual analysis provides a way to determine the misalignment of layers within a sTGC quadruplet.

Ultimately, we wish to characterize the layers of a quadruplet by two parameters, θ and

y_0 , where θ is the rotational offset and y_0 is the constant y -offset of the layer, as shown in Figure 5.3. Assuming these are the only non-conformities for a given layer, the data points can be transformed as

$$Y_{\text{fixed}}(\theta, y_0) = Y_{\text{data}} \cos \theta - X_{\text{data}} \sin \theta - y_0, \quad (5.2)$$

where X_{data} and Y_{data} are the x - and y -positions measured by a given quadruplet layer. The goal of this project is to create a program which can calculate the construction non-conformities in a quad using data from cosmic ray data as input. In essence, we ask: how do we determine the rotational and constant y -offset for the two non-fixed layers of a quadruplet?

In order to answer this question, two methods for determining the misalignments were considered. The methods for deriving layer misalignments from data are discussed here: the matrix method and the χ^2 minimization method. In short, the matrix method directly solves for θ and y_0 by solving an over-determined linear system, whereas the χ^2 minimization creates a χ^2 metric for each data set and seeks to minimize it with respect to θ and y_0 for each layer. However, data from the sTGC quadruplets cannot be the subject of this study, because their inherent misalignments are unknown. In order to evaluate the performance of the two methods, Monte Carlo simulations of cosmic runs were created.

5.1.1 Monte Carlo Modifications

Monte Carlo is a technique by which events with known random distributions are simulated, usually using computer software. In this case, muons passing through a sTGC quadruplet were simulated. The Monte Carlo generator (MCgen) was written by Waleed Ahmed as a way to simulate data collected by a quad with a known defect. The code allows the user to set several parameters, such as quadruplet type (QS3 vs QL2) and number of events simulated. MCgen outputs a processed ROOT file, unlike the binary files produced in cosmic muon tests. Nevertheless, the processed ROOT file allowed for manipulation of slightly higher-level behaviour, such as introducing geometric defects, than would be possible with the binary file. During the course of this thesis' work, MCgen was modified to accommodate the construction non-conformities described above: an individual layer's offset and rotation.

First, the x - and y -positions of a track in layer l are extracted. Let l_m be a layer into which we wish to introduce some rotation and offset. Let x_{old} and y_{old} be the x - and y -positions of the track on layer l_m . In order to simulate some construction y -offset, y_0 and some construction rotational offset, θ , the positions are transformed into a new coordinate, (x_m, y_m) according to

$$\begin{pmatrix} x_m \\ y_m \end{pmatrix} = \begin{pmatrix} \cos \theta & \sin \theta \\ -\sin \theta & \cos \theta \end{pmatrix} \begin{pmatrix} x_{old} \\ y_{old} + y_0 \end{pmatrix}. \quad (5.3)$$

This equation is replicated on a second misaligned layer, if desired. It should be noted that

no more than two layers can technically be misaligned with respect to the quadruplet, as without an external reference, misalignment is only relative to two fixed layers. Generating processed Monte Carlo ROOT files in this way is the main method of generating data for this project.

After Monte Carlo generation, all methods take advantage of the `CosmicsAnalysis` framework, produced by Dr. Benoit Lefebvre over the course of his PhD work [83]. `CosmicsAnalysis` files are ROOT files containing high-level information, such as residual plots, track information, and efficiency plots, that are generated by interpreting data taken from either Monte Carlo or cosmics test-stand runs using the `CosmicsAnalysis` software. Of particular interest to this study is the track information, in addition to the plots of inclusive and exclusive residuals, as described in Section 5.1. The flow of data for this project is summarized in Figure 5.4.

5.1.2 Performance Metrics

The performance of the methods will be determined via a variety of metrics. First, the most critical metric is accuracy. By producing Monte Carlo simulations of data with known rotation and offset, the results of the two analyses can be compared to Monte Carlo. Second, we wish to observe the behaviour of the errors with increasing statistics. We expect the error of y_0 and θ to decrease with increasing statistics, to some systematic limit. This provides confidence that the methods are converging to some meaningful value.

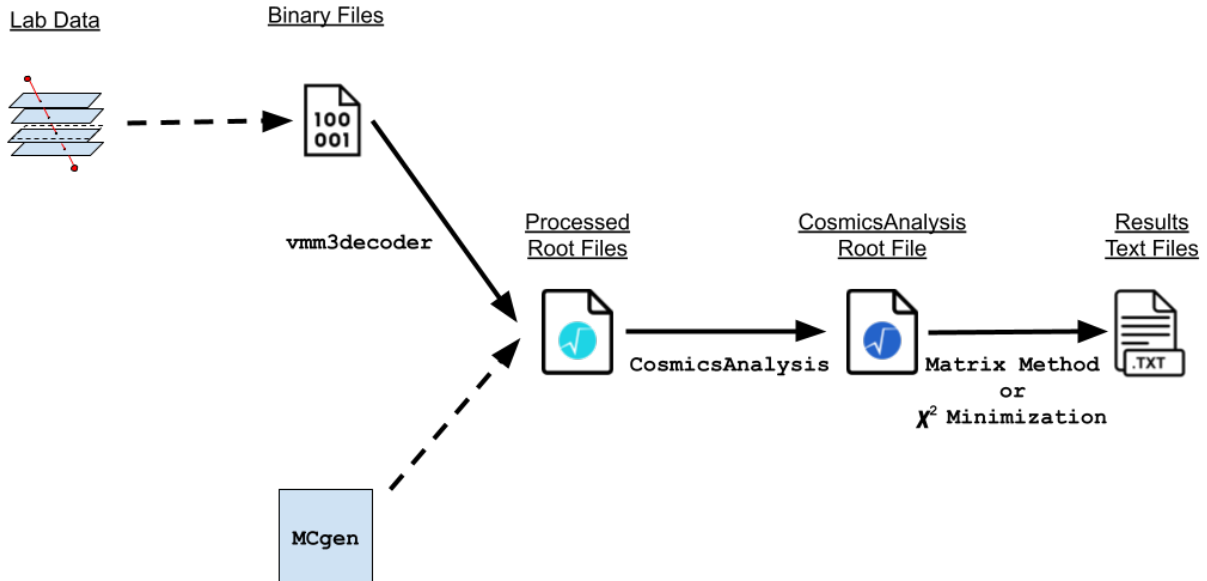


Figure 5.4: Flow of data to a misalignment prediction. Monte Carlo files are generated by MCgen for testing of the various programs. MCgen was developed by Waleed Ahmed. vmm3decoder translates binary files from the lab into low-level processed ROOT files. CosmicsAnalysis takes low-level processed ROOT files and generated high-level data for storage in CosmicsAnalysis ROOT files. Both were developed by Dr. Benoit Lefebvre [83].

Finally, consistent performance over small and large misalignments provides confidence in the predicted misalignment values when the program is eventually used on the sTGC quadruplets. A description of the matrix method and the χ^2 minimization method follows.

5.2 Matrix Method

5.2.1 Derivation

The derivation that follows is taken from the Appendix of Benoit Lefebvre's PhD thesis [83]. As described above, the matrix method uses linear transformations of fit parameters to determine the misalignment of a given quadruplet. Let (z_i, y_i) be the z and y coordinates of the hits on i arbitrarily spaced detector planes (with equal errors). Define the following sums over the spatial coordinates of each layer, i :

$$S_{zy} = \sum_i z_i y_i \quad S_y = \sum_i y_i \quad S_z = \sum_i z_i \quad S_{zz} = \sum_i z_i^2. \quad (5.4)$$

The track can be described as a line, $y_i = mz_i + b$, with slope and offset equal to

$$m = \frac{NS_{zy} - S_z S_y}{NS_{zz} - (S_z)^2} \quad b = \frac{S_{zz} S_y - S_z S_{zy}}{NS_{zz} - (S_z)^2}, \quad (5.5)$$

where N is the number of points used for the fit. The residual for a given layer, i , from the constructed track is therefore

$$\delta y_i = y_i - (mz_i + b),$$

or, described in matrix form as

$$y_{res}^* = My, \quad (5.6)$$

where y_{res}^* is a vector describing the residuals of the layers, y is a vector describing the y -coordinates of the layer hits, and M is a matrix defined as

$$M_{ij} = \delta_{ij} + \frac{z_i(S_z - Nz_j) + z_j S_z - S_{zz}}{NS_{zz} - (S_z)^2}. \quad (5.7)$$

where δ_{ij} is a Kronecker delta (0 if $i \neq j$, 1 if $i = j$). Because z -displacements are fixed in the sTGC quadruplets, M is a fixed matrix for any given sTGC. Normally, over a large number of events and a perfect detector, we would expect

$$\langle y_{res}^* \rangle = 0. \quad (5.8)$$

In other words, over a large number of events, we expect the average of the residuals to tend to 0. Consider a detector with a construction defect, such that y is displaced to $y + y_0$ (assume y_0 captures both rotational and offset defects). Because this is written as a linear system, equation 5.6 would become

$$y_{res}^* = My + My_0. \quad (5.9)$$

Thus, the statistical mean of the residuals would shift by

$$\langle y_{res}^* \rangle = \langle My_0 \rangle = My_0. \quad (5.10)$$

Because neither M nor y_0 are statistical, we may now determine the construction defects of a sTGC quad using the residuals, y_{res}^* by

$$M^{-1} \langle y_{res}^* \rangle = y_0.$$

However, the matrix M is singular. Physically, we interpret this as a need for an external reference. Construction defects are only meaningful in the context of a “correct” alignment; in other words, two layers must be considered “fixed” as external reference in order for the other two displacements to make sense.

This is accomplished by setting two of the elements of $\langle y_0 \rangle$ and y_{res}^* to 0. The corresponding columns in M are also zeroed; this new matrix, M^* now defines the system as

$$\langle y_{res}^* \rangle = M^* y_0. \quad (5.11)$$

This new system is now over-determined. The solution for an over-determined system is given as

$$y_0 = ((M^*)^T M^*)^{-1} (M^*)^T \langle y_{res}^* \rangle, \quad (5.12)$$

where y_0 gives the misalignment of each of the unfixed layers with respect to the fixed layers in terms of slopes and offsets.

5.2.2 Implementation

The matrix method program takes, as input, a `CosmicsAnalysis` file, the z -direction spacing between the gas layers, and which two of the four layers are to be considered “fixed” for the misalignment. We also include a flag which indicates whether to use inclusive or exclusive residuals. When implementing this method, it was assumed that the z -spacing between adjacent wire planes is fixed at 10.8 mm.

From the `CosmicsAnalysis` file, the code performs a linear fit on the value of the y -residuals as a function of the x -coordinate. This fit is performed on all four layers. The slopes and offset values, as well as their corresponding errors of the fits are placed into four-vectors, with each element representing one layer.

Next, constructing the matrix M , as defined in Eq. 5.7. M turns out to be the same matrix for all quadruplets, as it is assumed that the gas volume spacing is fixed, giving

$$M = \begin{pmatrix} 0.3 & -0.4 & -0.1 & 0.2 \\ -0.4 & 0.7 & -0.2 & -0.1 \\ -0.1 & -0.2 & 0.7 & -0.4 \\ 0.2 & -0.1 & -0.4 & 0.3 \end{pmatrix}. \quad (5.13)$$

Two of these layers have a residual value of 0, as they were chosen to be fixed. Thus, those fixed layers, represented by columns, are removed from the matrix M . Define this new matrix to be M^* . For example, if layers 1 and 4 were fixed, then M^* would be

$$M_{1,4}^* = \begin{pmatrix} -0.4 & -0.1 \\ 0.7 & -0.2 \\ -0.2 & 0.7 \\ -0.1 & -0.4 \end{pmatrix}.$$

The resultant solution would then be

$$y_0 = \begin{pmatrix} -\frac{2}{3} & 1 & 0 & -\frac{1}{3} \\ -\frac{1}{3} & 0 & 1 & -\frac{2}{3} \end{pmatrix} \langle y_{res}^* \rangle, \quad (5.14)$$

dependent on $\langle y_{res}^* \rangle$ extracted from the data.

The errors of these values are then calculated. All operations performed on the residuals are linear transformations of the data. Therefore, error is propagated by adding in quadrature. To simplify the code, M^* and the error vectors are element-wise squared, matrix multiplied, then square rooted. This is functionally the same as adding the errors in quadrature.

Finally, to convert a slope and accompanying error, m and δm , found from the matrix method to angles, θ and $\delta\theta$, arctangent and its derivative are used, giving

$$\theta = \arctan(m) \quad \delta\theta = \frac{\delta m}{1 + m^2}. \quad (5.15)$$

The results of the code are the rotation and offset of the two unfixed layers, with associated errors. A typical output from the program is shown in Figure 5.5. A more in-depth characterization of the matrix method is performed in Chapter 6.

```
Layer 2 has angle = -0.000132515 +- 6.69318e-06 radians  
Layer 2 has offset = -37.4788 +- 3.25011 um  
Layer 3 has angle = -0.000155756 +- 2.32882 radians  
Layer 3 has offset = -240.221 +- 1.77628 um
```

Figure 5.5: Typical output of the matrix method.

5.3 χ^2 Minimization Method

The χ^2 minimization method is based on code by the Chinese New Small Wheel group and their misalignment studies [89]. Essentially, by defining some χ^2 metric as a function of a presumed θ and y_0 , the $\theta - y_0$ phase-space can be explored to determine a minimum χ^2 value. The χ^2 minimization method assumes that the χ^2 surface on $\theta - y_0$ phase-space is concave, and that the program can converge on this minimum.

5.3.1 Algorithm Description

In the code developed by the Chinese NSW group, ROOT's TMinuit is used to minimize χ^2 with respect to θ and y_0 . TMinuit is a ROOT package designed to determine the absolute minimum of a χ^2 or log-likelihood function. TMinuit was similarly used in this project.

The code takes as input a CosmicsAnalysis file and the two layers to be considered “fixed” in this data. The CosmicsAnalysis file also must have included a “tracks” TTree, which is built when an optional switch is used in the CosmicsAnalysis program. In its current iteration, the code also includes an optional argument for the maximum number of events to analyze from the CosmicsAnalysis file. This feature is helpful when investigating the effect of statistics on misalignment results. After reading the file, the code creates a TChain object including all the tracks from the file. The code reads the analysis tag and the detector geometry from that CosmicsAnalysis file. Then, for each non-fixed layer, the code will undergo minimization.

In alignment with the Chinese NSW group, a χ^2 function is minimized. Due to the structure of TMinuit and its use of an error function, 4 separate χ^2 functions are coded for the 4 possible layers (termed `l1chi2function`, `l2chi2function`, `l3chi2function`, and `l4chi2function`). In other words, separate error functions exist for layer 1, 2, 3, and 4. All functions, however, follow the same general structure. Future work could go into abstracting the four functions into one with another parameter for cleaner code.

5.3.2 The χ^2 Functions

The χ^2 functions are a set of functions that output a χ^2 value for a given set of parameters and a tracks TTree. In the case of misalignment analysis, these parameters are θ (the candidate angle offset of a given layer), y_0 (the candidate y -offset of a given layer), and which of the layers are considered fixed. By outputting this χ^2 value over a wide set of possible θ and y_0 , TMinuit is able to determine the parameter values that minimize the χ^2 value.

The track must pass several checks in order to be included in the χ^2 calculation. The track must have each layer's hit x -coordinate be between -600 and 600, as this is the range of the sTGC quadruplet's x -values. The track must have exactly 4 hits for each track, and have non-zero errors for the Y -values. Moreover, the track's points must be non-saturated, where saturation refers to the maximum electrical signal that a strip, wire, or pad can output. Should a signal be saturated, the linearity of running in a proportional mode is lost, leading to inaccurate results [83]. Finally, the charge cluster size, defined as the number of adjacent strip channels that have non-zero signal during an event, must be between 3 and 5. A cluster size less than 3 should not be possible, as the FEBs collect data from both neighbouring strips when a strip is triggered. Cluster sizes greater than 5 are likely to not be caused by a single muon, but rather by high-energy electrons (ie. δ -rays) produced by primary ionization that continue to ionize further away from the initial ionization events caused by the muon [83]. Only tracks that fulfill all of these conditions can be used to calculate the χ^2 .

For simplicity, consider the data from one track only. Let l_a, l_b be the first and second

layers to be fixed, l_c be the current layer to be analyzed for misalignment, and let $x(l)$ and $y(l)$ be the x - and y -value, respectively, of the hit of the l -th layer, as taken from the track data. Define scaleZ to be

$$\text{scaleZ} = \frac{l_c - l_a}{l_b - l_a}. \quad (5.16)$$

Since we assume l_a and l_b to be perfectly aligned, we can extrapolate, from the data, a y -value for l_c . The extrapolated y -value from the linear fit is

$$y(l_c)_{\text{linear fit}} = \text{scaleZ} \times (y(l_b) - y(l_a)) + y(l_a). \quad (5.17)$$

However, l_c is assumed to be misaligned. Again, let θ be the angle offset of a given layer and y_0 be the displacement of a given layer. The $y(l_c)$ extracted from data is then transformed according to the model

$$y(l_c)_{\text{model}} = y(l_c) \cos \theta - x(l_c) \sin \theta - y_0. \quad (5.18)$$

The difference between these two values is the residual, δy , given as

$$\delta y = y(l_c)_{\text{model}} - y(l_c)_{\text{linear fit}}. \quad (5.19)$$

This calculation is carried out for each of the tracks that passed the checks above, which we

will label i , with N being the total number of passed tracks. The output of this function is the sum of the squared residuals over all tracks, with each residual being weighted by the error in the y -measurement of the track, σ_y . This sum is termed the χ^2 , defined as

$$\chi^2 = \sum_i^N \frac{\delta_y^2}{\sigma_y^2}. \quad (5.20)$$

The mean residual, $\bar{\delta y}$ and the standard deviation, $\bar{\sigma}_y$ are also calculated, for logging purposes, and are defined as

$$\bar{\delta y} = \frac{1}{N} \sum_i^N \delta y \quad (5.21)$$

$$, \bar{\sigma}_y = \frac{1}{N} \sum_i^N \delta y^2. \quad (5.22)$$

Equation 5.20 is then utilized by TMinuit to get a χ^2 value for a wide variety of (θ, y_0) points. By comparing the χ^2 of these points, the program systematically steps through the phase-space until it arrives at a global minimum. The θ and y_0 at that point is the predicted value of the rotation and offset of the layer. Errors are automatically calculated by TMinuit. This calculation is then carried out for the other unfixed layer. In addition to displaying the misalignments of the quadruplet's unfixed layers, the program also prints the χ^2 of the (θ, y_0) configurations used during the minimization process.

There are two major versions of the χ^2 minimization code, termed "1-pass" and "3-pass".

At early stages in development, small data sets were used to test the code. After a single “1-pass” TMinuit minimization, however, the program displayed poor results and large errors in the results. This led us to consider using multiple minimizations to reduce errors. When developed, the code used three sequential minimizations. First, χ^2 is minimized with respect to θ , holding $y_0 = 0 \mu\text{m}$, initialized at $\theta_0 = 0$. The result is θ' . Then, minimize χ^2 with respect to y_0 , holding $\theta = \theta'$, initialized at $y_0 = 0 \mu\text{m}$. The result is y'_0 . Finally, minimize χ^2 with respect to θ and y_0 , initialized using θ' and y'_0 . The result of this final minimization would be the output values of the offset and rotation. The step size of the minimization is also reduced in the third iteration by a factor of 1000. This was meant to increase the precision of the final results and reduce the error bars. The minimizations were bounded to explore strictly between ± 0.6 mrad and between $\pm 10^4 \mu\text{m}$.

Upon initiating this project, it was decided that the core structure of the code should be implemented for only one layer to start. In other words, the base algorithm would be designed assuming only one middle layer (in this case, Layer 2) is misaligned and always choosing Layers 1 and 4 to be fixed. The base code could then be extended to be able to analyse two layers at once, while also being able to choose which layers to fix. This would allow for easier code development and debugging. After this step was completed, the code was extended to predict the misalignments of both unfixed layers.

In addition to the predicted misalignment values, the program outputs a number of quantities for logging purposes. The program will output the tested angle, offset, and χ^2

```

-----
Angle, Offset, Chi2
0.000133037,-0.271985,4.91663e+06,
-----
Angle, Offset, Chi2
0.000152516,-0.264163,4.91664e+06,
-----
COVARIANCE MATRIX CALCULATED SUCCESSFULLY
FCN=4.91663e+06 FROM MIGRAD STATUS=CONVERGED 67 CALLS 68 TOTAL
EDM=9.45867e-06 STRATEGY= 1 ERROR MATRIX ACCURATE

EXT PARAMETER STEP FIRST
NO. NAME VALUE ERROR SIZE DERIVATIVE
1 angle 1.33037e-04 3.52477e-05 3.34279e-02 -8.24373e-02
2 offset -2.70681e-01 1.17545e-02 6.52069e-04 -6.62911e+00
EXTERNAL ERROR MATRIX. NDIM= 25 NPAR= 2 ERR DEF=1
1.244e-09 -3.561e-07
-3.561e-07 1.382e-04
PARAMETER CORRELATION COEFFICIENTS
NO. GLOBAL 1 2
1 0.85888 1.000 -0.859
2 0.85888 -0.859 1.000
=====
Layer 2 has angle = 0.000095 +- 0.000034 radians
Layer 2 has offset = -77.160755 +- 11.459173 um
=====
Layer 3 has angle = -0.000133 +- 0.000035 radians
Layer 3 has offset = -270.681486 +- 11.754513 um
=====
Analyzed Events: 59110/539322
=====
*** Goodbye! ***

```

Figure 5.6: Typical output from the χ^2 minimization method. (A) shows the last two entries in the χ^2 log. This tuple is printed at every tested point by the minimizer. (B) shows the results from the minimization with errors. (C) shows the ratio of analyzed events.

value at every tested point. It will also output the number of events actually kept by the program after the various checks and cuts. A typical output from the program is shown in Figure 5.6. These features will assist with characterizing the method in later experiments.

5.3.3 Implementation and Statistics Experiments

Due to success by the Chinese NSW group [89], it is known that the method was practically sound. Thus, during implementation, the accuracy of the method, defined as the ability of the code to predict the misalignment hard-coded into each of the simulations, was used as a metric to ensure code development was progressing correctly. In addition to this, it is expected that the error in the predicted θ and y_0 should decrease to some systematic error with number of events analysed, with predictions that converge with greater statistics. Additionally, the effect of the order of the first two minimizations was also explored, as the two initial minimizations are asymmetric. Finally, while the Monte Carlo outputs a half-million events, several remappings and cuts, implemented by Dr. Benoit Lefebvre and described in Subsubsection 5.3.2, are performed to filter out incomplete data. Thus, the percentage of events kept after all these cuts is also of interest.

To evaluate accuracy, Monte Carlo simulations were used. By hard-coding an offset and rotation within the generator's code, data with known offsets and rotations could be generated. Four such simulations were created with 1 000 000 triggers each, with a range of offsets and rotations. This corresponds to roughly half a million events. Rotations and offsets were chosen both within and outside the range of tolerance to characterize the misalignment software's ability to detect both small and large non-conformities. A fourth simulation with no built-in offset and rotational misalignment was also tested. All simulation and testing was performed on the lxplus computing cluster, available to all CERN users.

At the McGill sTGC lab, 500 000 cosmic events are captured per quadruplet per voltage level. To determine the code's performance over varying numbers of events up to half a million, the misalignment software was also tested using different numbers of events. The code performed 11 predictions for each simulation, taking larger and larger subsets of the simulation each time to calculate the misalignment.

Results

To investigate the behaviour of results with increasing statistics, the four Monte Carlo simulations were used as input into the χ^2 minimization code. At 10^5 kept events, corresponding to roughly 500 000 MC-generated triggers, the minimization code was able to predict the angle and offsets of the MC runs when they were within the range of tolerance. Figure 5.7 shows that, for a zero-misalignment run at 500 000 events, the code was able to predict the offset and rotation. Similar results were found for simulations where a non-zero rotation or offset fell within the range of tolerance, as shown in Figure 5.8. Accuracy did not decline when the true rotation and offset misalignments were outside of the range of tolerance, as demonstrated in Figures 5.9 and 5.10.

As shown in the Figures 5.7 and 5.8, the uncertainty decreases monotonically with increasing kept events, as expected. At 1 000 000 triggers (the number of triggers normally collected in an in-lab cosmics run), the average errors are $\delta\theta = 0.025$ mrad and $\delta y_0 = 8.3$ μm . These errors are suitable for the tolerances defined in Table 4.2, $\text{Tol}_\theta = 0.069$

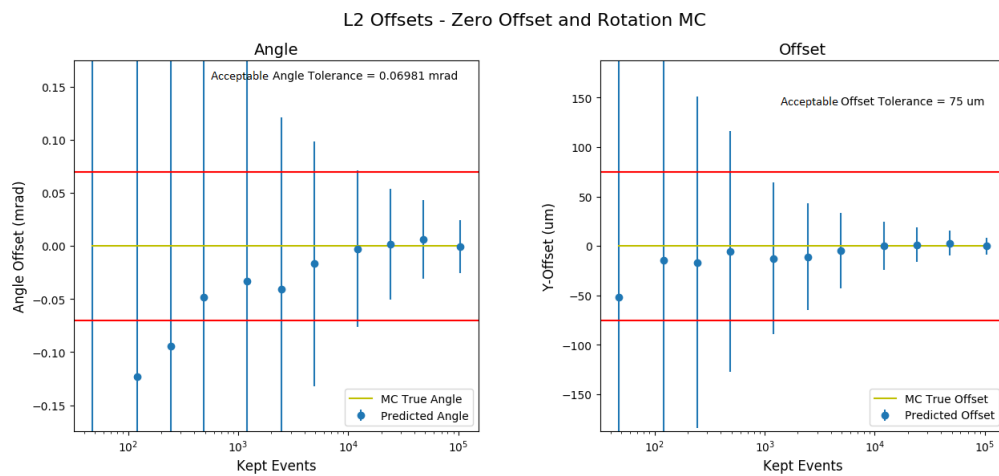


Figure 5.7: Predicted angle and offset misalignments by χ^2 minimization from a MC simulation with zero offset and rotation, as a function of analyzed (or kept) events. Range of acceptable tolerance bounds are indicated by the red lines, according to Table 4.2. While the true value of the MC offset and rotation always fell within the error bars of the predictions, more kept events lead to smaller error bars. At 10^4 kept events and above, the uncertainty is smaller the acceptable tolerance bound.

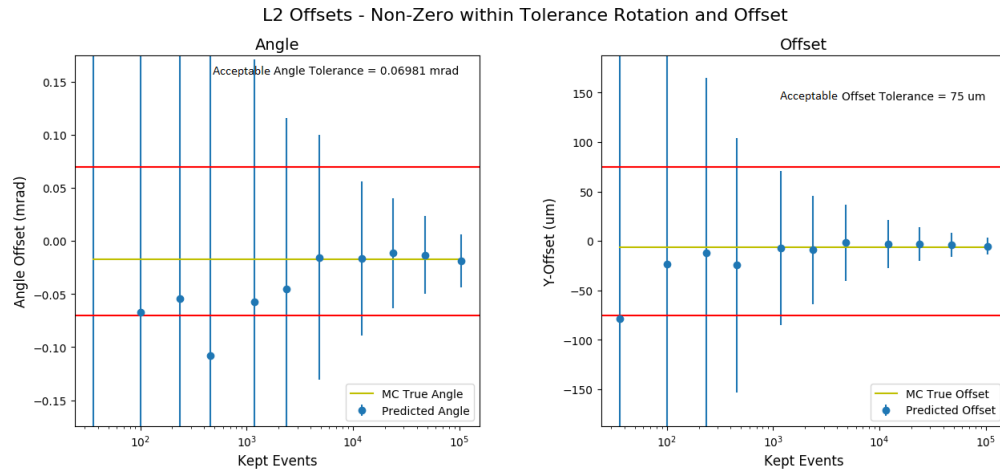


Figure 5.8: Predicted angle and offset misalignments by χ^2 minimization from a MC simulation with a non-zero rotation and offset. Range of acceptable tolerance bounded by the red lines, according to Table 4.2. The code is able to converge to the true misalignment value at 10^5 kept events.

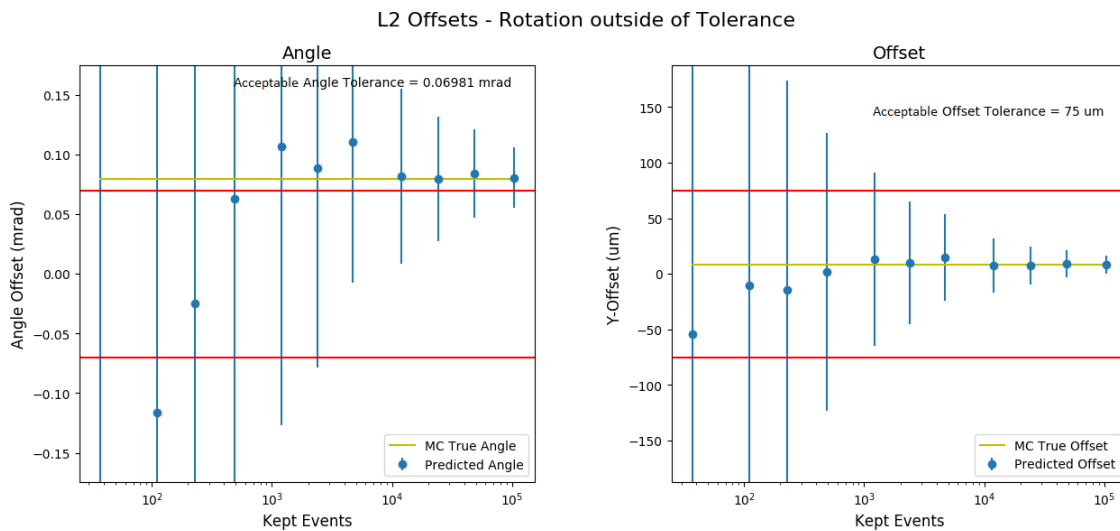


Figure 5.9: Predicted angle and offset misalignments by χ^2 minimization from a MC simulation with a large non-zero rotation and offset, with the rotational misalignment outside of the range of tolerance. Range of acceptable tolerance bounded by the red lines, according to Table 4.2.

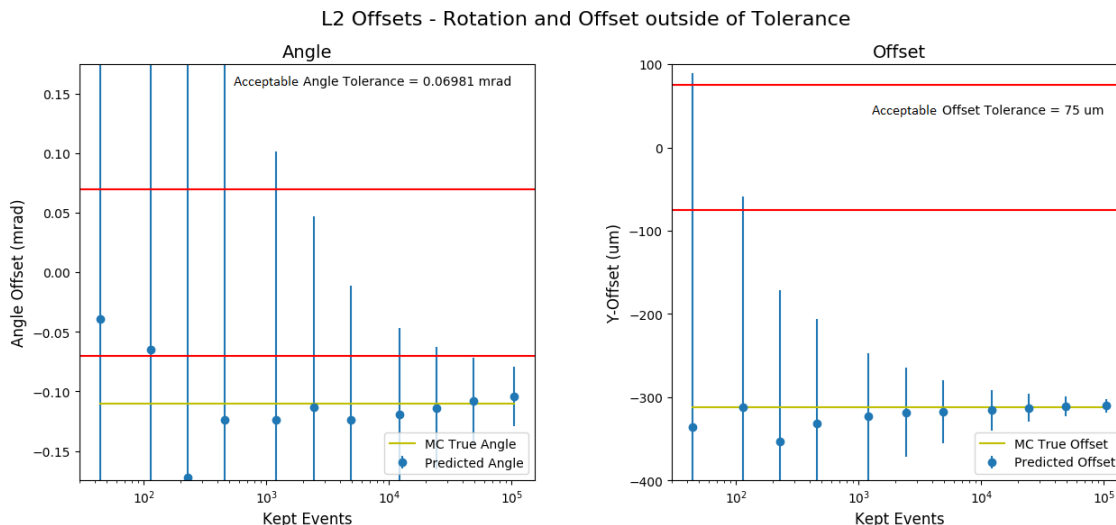


Figure 5.10: Predicted angle and offset misalignments by χ^2 minimization from a MC simulation with a non-zero outside-of-tolerance rotation and offset. Range of acceptable tolerance bounded by the red lines, according to Table 4.2.

mrad and $\text{Tol}_{y_0} = 75 \mu\text{m}$, as errors outside the range of tolerance would not give us a clear pass-fail criterion for a quadruplet. The worst-performing run in terms of accuracy of the central value was the high-offset run, as shown in Figure 5.10, with predicted values averaging 0.2 standard deviations away from the true value. Nevertheless, the prediction still agreed with the true misalignment.

The experiment also provided results regarding the checks, cuts, and order of minimization. By the end of all the cuts and checks implemented in the code, an average of 85% of events are kept for the analysis, except for at 2 000 000 MC triggers which analyzed only 49% of the events (425 828 analyzed out of 856 658 events). This smaller subset of analyzed events suggests a potential maximum number of events that can be analyzed at

once by the program, potentially due to memory leak. However, because cosmics runs only ever collect 1 000 000 triggers, this upper limit should not be reached when characterizing sTGC quadruplets. Finally, at 500 000 events, the order of minimization was shown not to affect the performance of the minimization code, as summarized in Table 5.1.

		Angle (mrad)	Offset (μm)
Trial 1	$\theta - y_0$ Result:	-0.10 ± 0.02	-310 ± 8
	$y_0 - \theta$ Result:	-0.10 ± 0.02	-310 ± 8
	True (MC) Value:	-0.10990	-312.00
Trial 2	$\theta - y_0$ Result:	0.08 ± 0.03	8 ± 8
	$y_0 - \theta$ Result:	0.08 ± 0.03	8 ± 8
	True (MC) Value:	0.07930	8.10
Trial 3	$\theta - y_0$ Result:	-0.02 ± 0.02	-5 ± 8
	$y_0 - \theta$ Result:	-0.02 ± 0.02	-5 ± 8
	True (MC) Value:	-0.01745	-6.00

Table 5.1: Results of Switching the Order of Minimization. No significant change was observed when switching the order of the first two minimizations.

5.4 χ^2 Phase-Space Plotter

In order to evaluate the effectiveness of the χ^2 minimization method of exploring the $\theta - y_0$ phase space, a phase space plotter was created. As input, the code would take the log file of a χ^2 minimization run and output a 3D plot of the phase-space exploration for both unfixed layers. The plotter would be tested first on a Monte Carlo simulation and then a real-world quadruplet.

Representative phase-space plots from the Monte Carlo simulation are shown in Figure 5.11. The plots reflect the univariate nature of the first two minimizations undertaken by the χ^2 minimization method. The method starts at $(\theta, y_0) = (0, 0)$, travelling along θ while holding y_0 constant at $0 \mu\text{m}$. It then attempts to vary the offset, and only after that does it vary both variables in order to find the minimum. A representative plot from an arbitrary sTGC quadruplet is shown in Figure 5.12.

The success of the χ^2 minimization method and the matrix method means that there are two viable methods of calculating the misalignments of a quadruplet. The question of which method should be used is subject to several different factors. Which method is more accurate? Which method gives smaller errors on accurate predictions? Are there different regimes or conditions where one method outperforms the other? These questions lead to the characterization studies described in the following chapter.

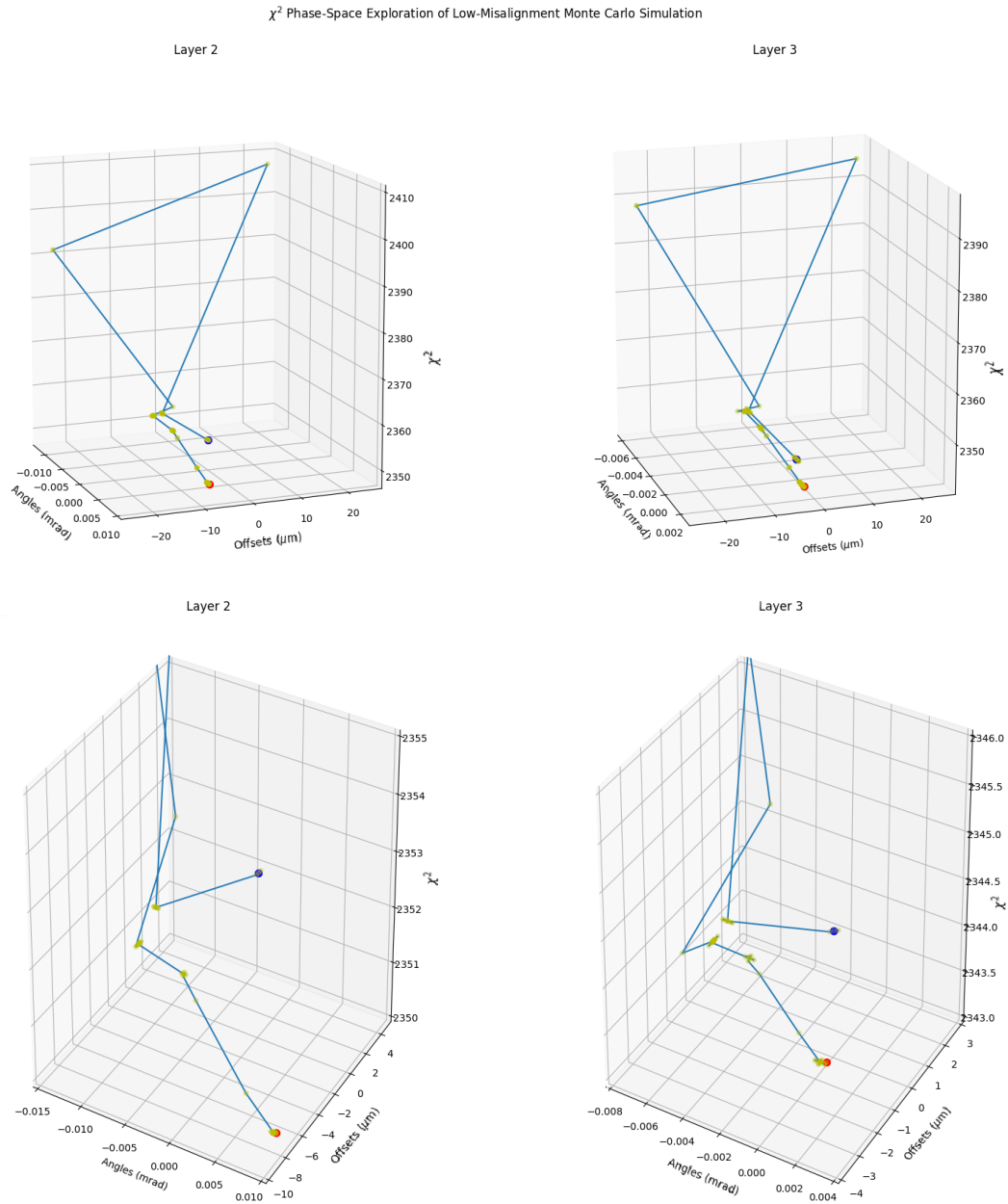


Figure 5.11: Phase-Space Exploration of the χ^2 minimization method with a Monte Carlo simulation. The method starts at $(\theta, y_0) = (0, 0)$, as shown by the blue point, and progresses to the minimal- χ^2 configuration, shown by the red point. Intermediate points are shown as yellow crosses. (Top) Overall phase space exploration. (Bottom) The same phase space exploration, zoomed in.

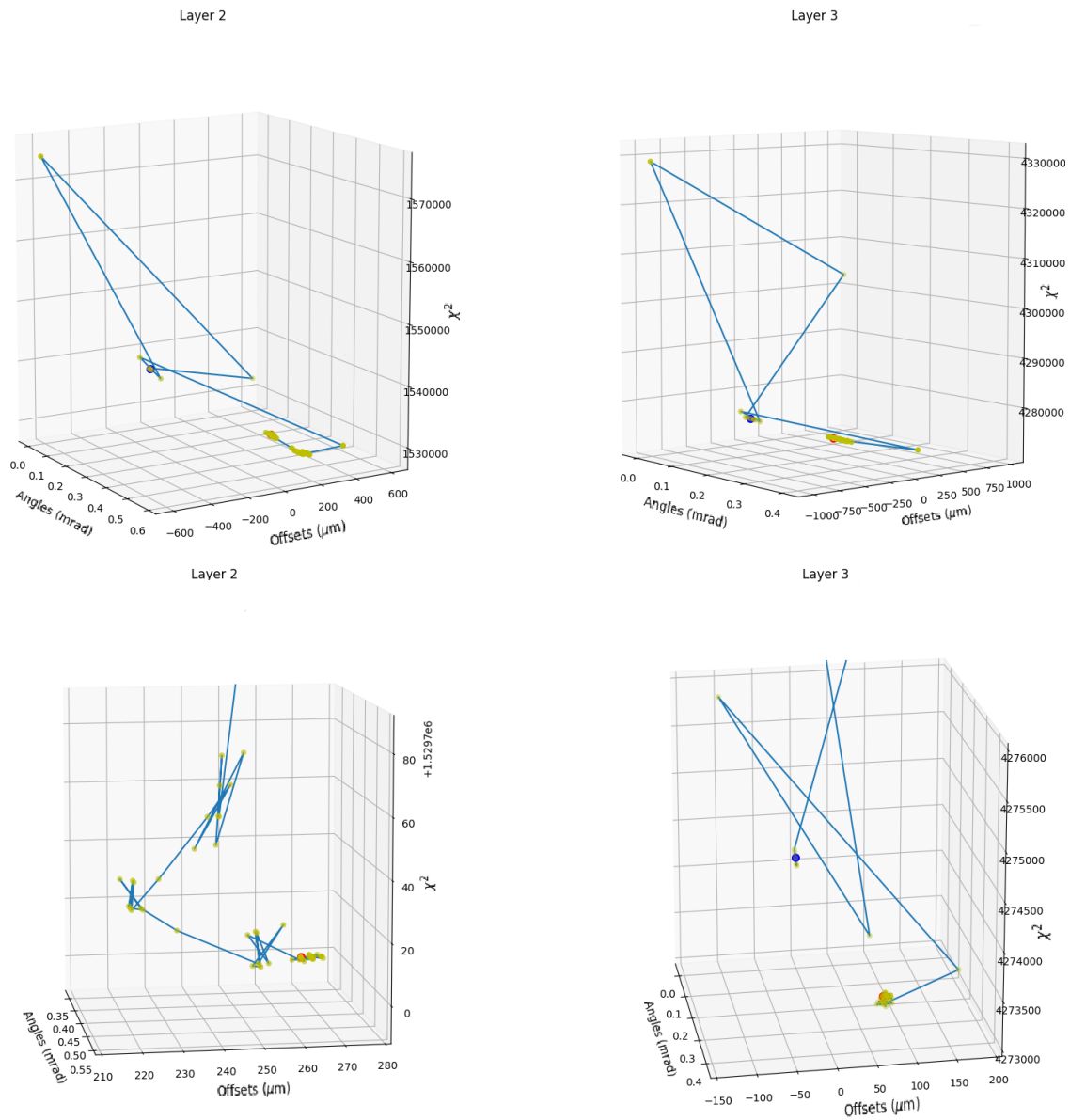
χ^2 Phase-Space Exploration of QL2C14 Quadruplet at 3100 Volts

Figure 5.12: Phase-Space Exploration of the χ^2 minimization method with quadruplet QL2C14 at 3100 Volts. The method starts at $(\theta, y_0) = (0, 0)$, as shown by the blue point, and progresses to the minimal- χ^2 configuration, shown by the red point. Intermediate points are shown as yellow crosses. (Top) Overall phase space exploration. (Bottom) The same phase space exploration, zoomed in.

Chapter 6

Characterizing Method Performance

With the matrix method and χ^2 minimization method implemented in the code, we now want to determine which method would be best to use when characterizing the sTGC quadruplets. To this end, three questions are important to consider. First and foremost, which method is more accurate in its prediction? Second, are the errors precise enough to give a meaningful conclusion? If the reported errors are larger than the rotational and offset tolerances defined in Table 4.2, the predictions are too imprecise to properly determine if a quadruplet is suitable for use in the ATLAS detector. Finally, how consistent are the different methods? Specifically, do the two methods perform differently close to zero misalignment in comparison to large misalignments? In addition to these criteria, the effect of increasing statistical power in the form of more events could also be studied. By studying the effect of statistics on both accuracy and error, we could determine if there is an optimal number of events required to

optimize the success of each of the methods.

The matrix method and χ^2 minimization method were developed at two different times, and thus were treated somewhat differently in their initial characterization studies. Thus, to put them on equal footing, the following experiment was performed using the exact same Monte Carlo simulations with a known misalignment.

6.1 Statistics Experiments

6.1.1 Description of Experiment

The motivation of this experiment is to further examine the accuracy and errors of both methods, but with the same misalignment values. Values were chosen to be around the same order of magnitude as the tolerances outlined in Table 4.2. The intention was to answer the questions above with an emphasis on exploring the effect of increasing statistics. Moreover, it could also determine the ratio of events actually kept by the χ^2 method after all the checks and cuts.

True Rotation	True Offset	Triggers				
0.07 mrad	150 μm	2 000	10 000	50 000	200 000	1 000 000
Consistent across all simulations		5 000	20 000	100 000	500 000	2 000 000

Table 6.1: Parameters of Statistics Experiment. 10 separate Monte Carlos with the same offset and rotation but different number of triggers were generated. Misalignment parameters are chosen to be the same order of magnitude as the acceptable bound of tolerance.

For this experiment, ten Monte Carlo simulations were performed. All ten simulations had the same offset and rotational misalignment, but a different number of triggers, as detailed in Table 6.1. The misalignments were outside tolerance, while the number of triggers spanned from 2000 triggers to 2 000 000, or the amount of triggers collected in a normal McGill sTGC cosmics run. Recall that the actual number of events is around half the nominal amount of triggers. The seed values were also different, meaning that different sets of events were generated for each simulation. Finally, χ^2 minimization (1-Pass) and the matrix method (using both inclusive and exclusive residuals) were run over each simulation. 3-Pass χ^2 minimization will be analyzed more closely in the next experiment.

By performing this experiment, we can determine the validity of the following hypotheses. First, it is hypothesized that the χ^2 minimization method will have better accuracy and lower errors. In order to derive the matrix method, a small-angle approximation was assumed. Thus, a simulation with a relatively large rotational misalignment may reveal the limitations of that assumption. The methods will be compared using both small and large rotational misalignments in later sections. However, the performance of the χ^2 minimization method, intuitively, must also depend on how well TMinuit explores the (θ, y_0) phase space. To address this concern, the methods will be compared with both small and large rotational misalignments in later sections. Secondly, the matrix method using inclusive residuals should outperform using exclusive residuals in all respects. Dr. Lefebvre's derivation in his PhD thesis used inclusive residuals, so this

result is expected. Admittedly, this experiment is more exploratory in nature with regards to using exclusive residuals. Thirdly, it is hypothesized that across all three methods, the errors should decrease with increasing statistics. Preliminary glimpses of this were seen with the previous χ^2 tests during development, but this behaviour should also naturally extend to the matrix method. Finally, at 1 000 000 triggers, the errors for all methods should be within tolerance, thus making their predictions meaningful.

6.1.2 Results

The accuracy of the predictions are displayed in Figure 6.1, with the errors plotted in Figure 6.2. All methods converge to the proper truth value as statistics increase. However, some errors seem to behave erratically. As seen in Figure 6.1 but also reflected in Figure 6.2, the error of the χ^2 method decreases uniformly with increasing statistics. However, the error of both matrix methods vary widely and inconsistently with increasing MC triggers.

6.1.3 Discussion

With respect to accuracy and error, the χ^2 minimization method performs similarly to its initial characterization tests. These results tended to outperform both versions of the matrix method. That being said, the matrix method using inclusive residuals was able to predict the misalignment across both layers, albeit with an unreasonably large error on the Layer 2 angle prediction. As expected, the use of exclusive residuals was shown to be somewhat

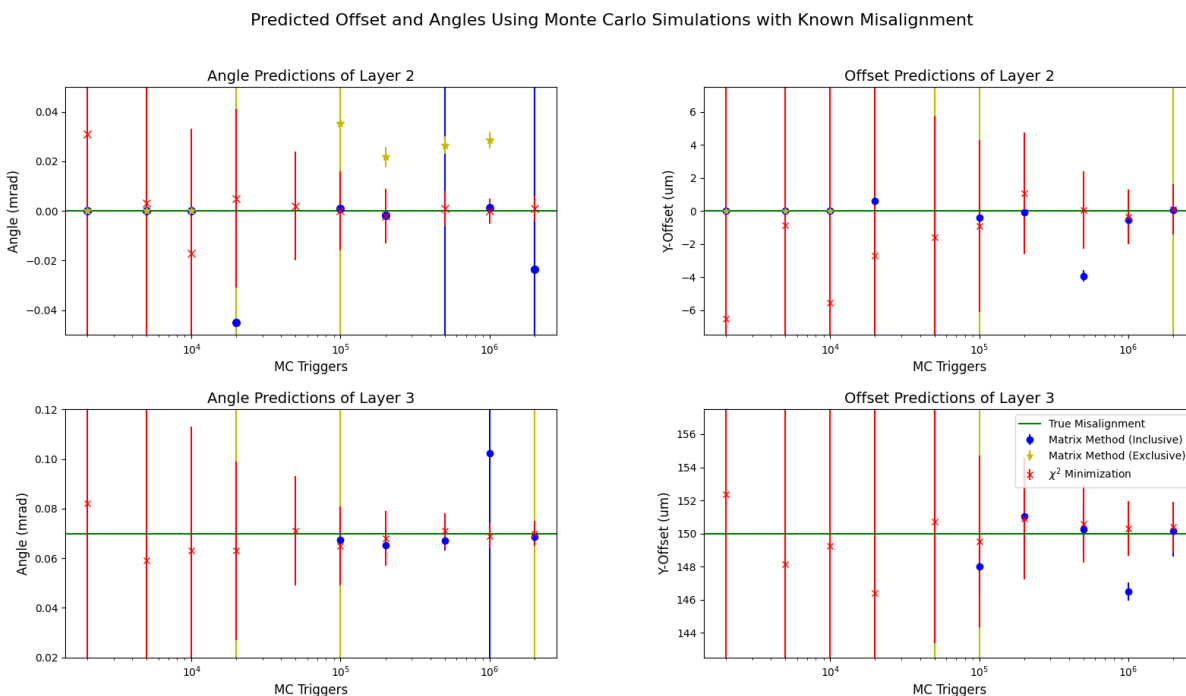


Figure 6.1: Semi-Log plot of the effect of statistics on misalignment prediction methods' accuracy. Both the χ^2 minimization method and matrix method with inclusive residuals perform well in predicting the true misalignments at high number of Monte Carlo triggers. Several exceptions are present for the matrix method using inclusive residuals, most notably the offset predictions for layer 2 at 5×10^5 triggers and for layer 3 at 10^6 triggers.

reasonable, but still not as predictive as using inclusive residuals.

As hypothesized, the χ^2 minimization errors decreased with increasing statistics across all predicted values. However, errors did not monotonically decrease for the matrix method using either set of residuals. This effect seems most pronounced with the Layer 2 Angle predictions. As seen in Figure 6.2, the errors of both matrix methods increase past 10^2 mrad at 1 000 000 MC triggers. Again, this is most evident with the Layer 2 Angle predictions of

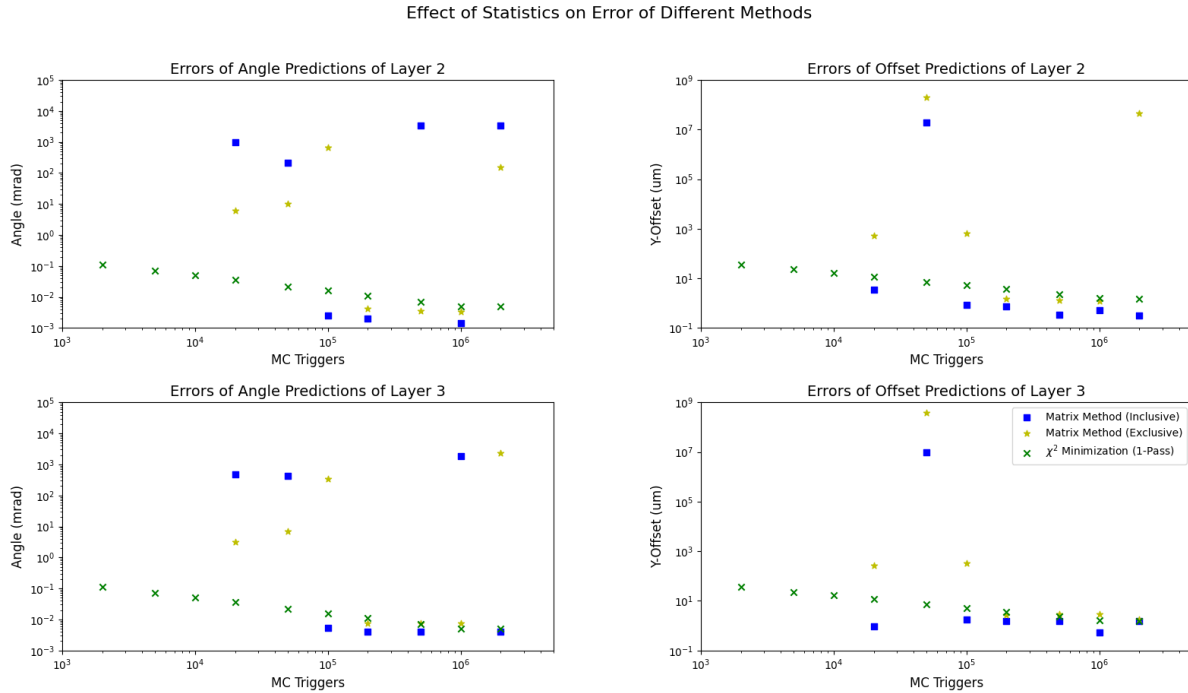


Figure 6.2: Log-Log plot of effect of statistics on the errors of misalignment prediction methods. χ^2 errors decrease monotonically, while matrix method errors can vary between different orders of magnitude.

the inclusive residual matrix method, where after 200 000 MC triggers, the central value of the predict deviates away from zero. Because no clear pattern emerges, the reasons for this deviation is unclear.

6.2 Consistency Experiments

With preliminary results suggesting the χ^2 minimization method is superior across all criteria, another crucial metric comes to mind. The erratic performance of the matrix

method is somewhat questionable. Moreover, because the methods were tested with a high rotation simulation, what if the small-angle approximation failed in this case, but could be better at smaller values? This leads to another crucial metric not explored in the statistics experiments: consistency. Consistency can be defined as the ability of a method to produce stable results in both accuracy and error across a wide range of misalignment values, both within and out of tolerance. The consistency question leads to the next experiment, whose primary purpose is to characterize the methods' accuracy and error across different regimes of misalignment.

6.2.1 Methods

	Zero	Within Tolerance			Outside of Tolerance	
Rotation (mrad)	0	0.02	0.04	0.07	0.2	0.4
Offset (μm)	0	20	40	75	150	300

Table 6.2: Possible Rotations and Offsets of Layer 3 in the Consistency Experiments. All combination of offset and rotation are explored, giving 36 different misalignment combinations.

In this experiment, 36 Monte Carlo simulations with different rotation and offset values were performed. The simulations all had 1 million triggers, to match the number of triggers performed in a standard McGill cosmics run. In all simulations, only Layer 3 was misaligned, while Layer 2 has held at zero misalignment. One rotational and one offset misalignment were chosen to be zero, three rotational and three offset were chosen to be

within tolerance, and two rotational and two offset were chosen to be outside of tolerance, as shown in Table 6.2. These values were chosen to better explore the behaviour of the different methods in different relevant regimes. From the six possible rotational and six possible offset misalignments, one unique combination of rotational and offset misalignment was chosen for each simulation. In this experiment, the simulations were used as input into all four methods: matrix method with both inclusive residuals and exclusive residuals, and both 1-Pass and 3-Pass χ^2 minimization. Finally, the accuracy and errors of the methods are compared to truth.

Several results are hypothesized. First, it is hypothesized that the χ^2 3-Pass Method should be the most accurate and have the lowest error, even when compared to the χ^2 1-Pass method. Based on the previous experiment, χ^2 1-Pass was the better performing code out of the three. Thus, the χ^2 3-Pass method should outperform the other three methods across all metrics, as it is designed to have lower error and higher accuracy than the 1-Pass method. Furthermore, with respect to both χ^2 minimizations, Layer 2 results should not be affected by changing Layer 3 misalignment, while this may present a problem for the two matrix methods. When the χ^2 method performs a minimization fixing Layers 1 and 4, it minimizes each layer separately, only taking data from Layers 1, 4, and the specific layer in question. With respect to consistency, as rotation increases, the matrix method should worsen in terms of accuracy, as the matrix method derivation depends on the small-angle approximation. Conversely, the matrix method may perform better or at least comparable

to the χ^2 method at low angles.

6.2.2 Results

Initial Observations

Initial results comparing the accuracy of all four methods are shown in Figures 6.3 and 6.4, while the errors of all four methods are compared in Figure 6.5. Accuracy here is defined as the absolute difference between truth and prediction. For the Layer 2 plots, because the true misalignment is zero, these points are taken as the absolute value of the predictions. The x -axis shows the different offset and rotation values of the Layer 3 misalignments over the 36 Monte Carlo simulations. Six points should therefore be plotted at every x -value.

Any meaningful patterns from the plots are hidden by the large absolute difference values given by the matrix method using exclusive residuals for some simulations. These results are not only higher than our desired tolerance values, but also much higher when compared to all the other methods. Moreover, the errors provided by both inclusive and exclusive residual versions of the matrix method are higher than those provided by χ^2 minimization. This behaviour warrants the examination of the matrix method using exclusive residuals separately from the other three methods.

Method Accuracy over varying True Layer 3 Rotations

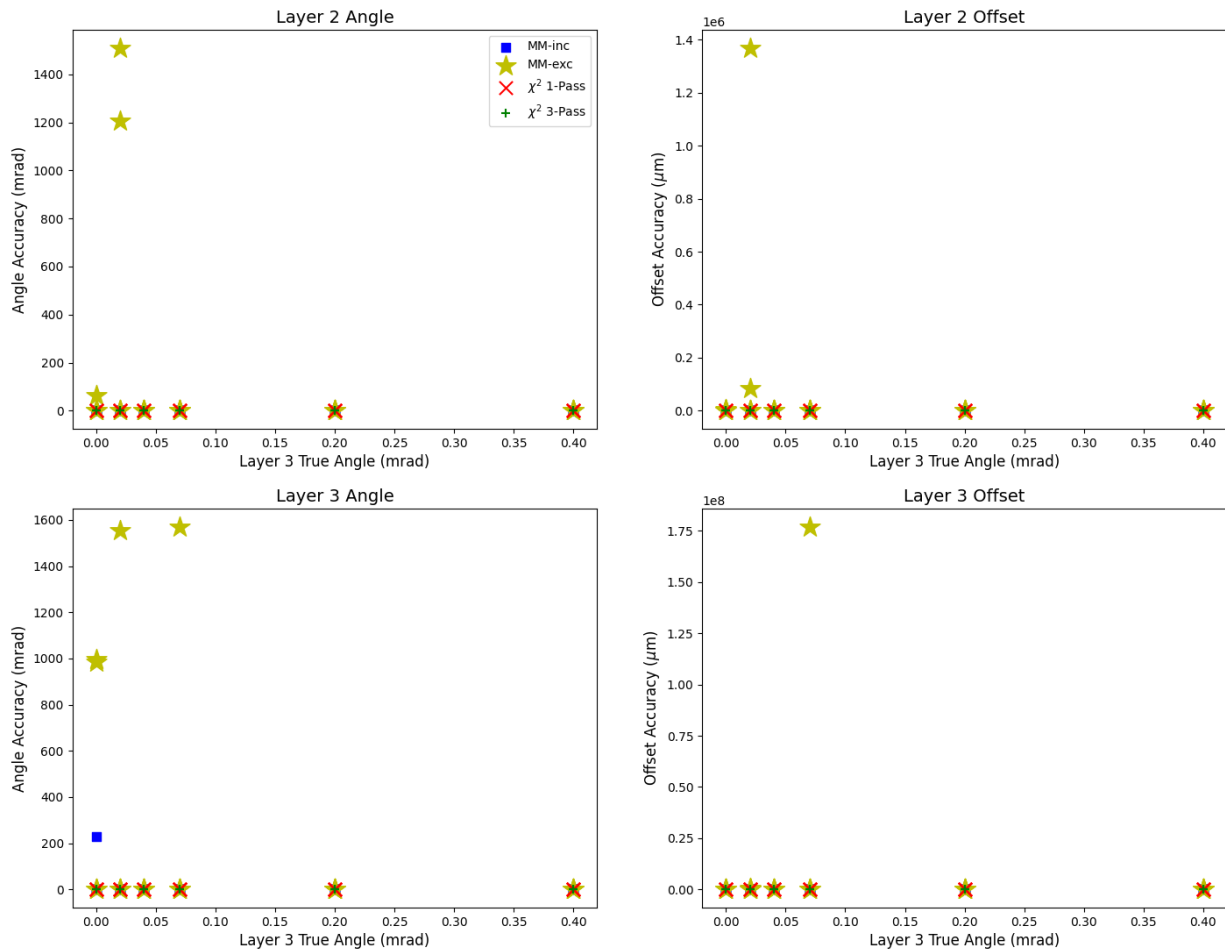


Figure 6.3: Accuracy Results from all four methods as true angle varies from 0.00 to 0.40 mrad. Several large outliers from the matrix method using exclusive residuals make interpretation difficult.

Matrix Method using Exclusive Residuals

The results from the matrix method using Exclusive residuals are shown in Figure 6.6. The large absolute differences present here strongly suggest that this method is too inconsistent

Method Accuracy over varying True Layer 3 Offsets

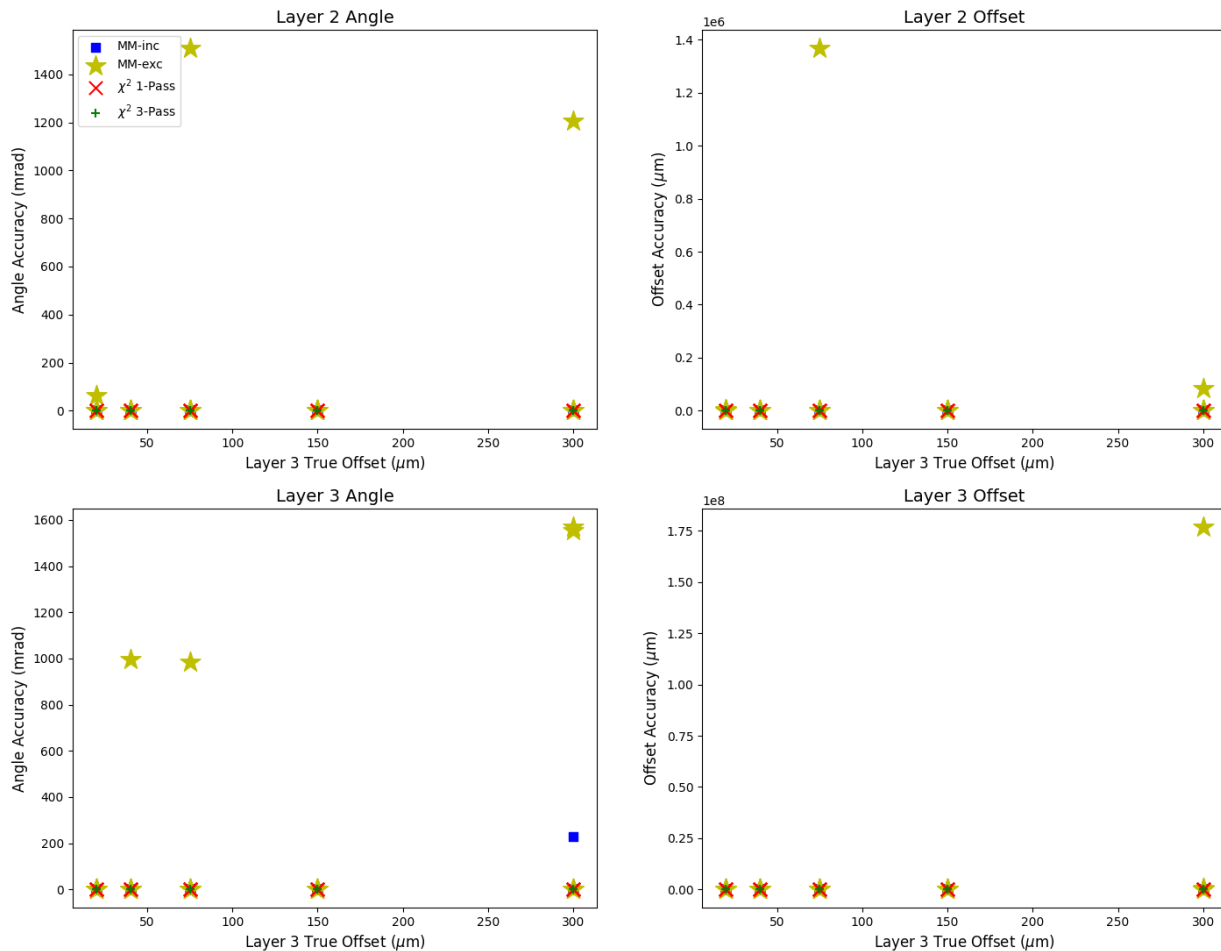


Figure 6.4: Accuracy Results from all four methods as true offset varies from 0 to 300 μm . Several large outliers from the matrix method using exclusive residuals make interpretation difficult.

to be of use when characterizing the sTGCs. Furthermore, the errors, as seen in Figure C.3 are, again, too large too inconsistently. Notably, the Layer 3 Offset plot as it varies with offset has a shape that could potentially be a log graph. A linear scale plot is shown in

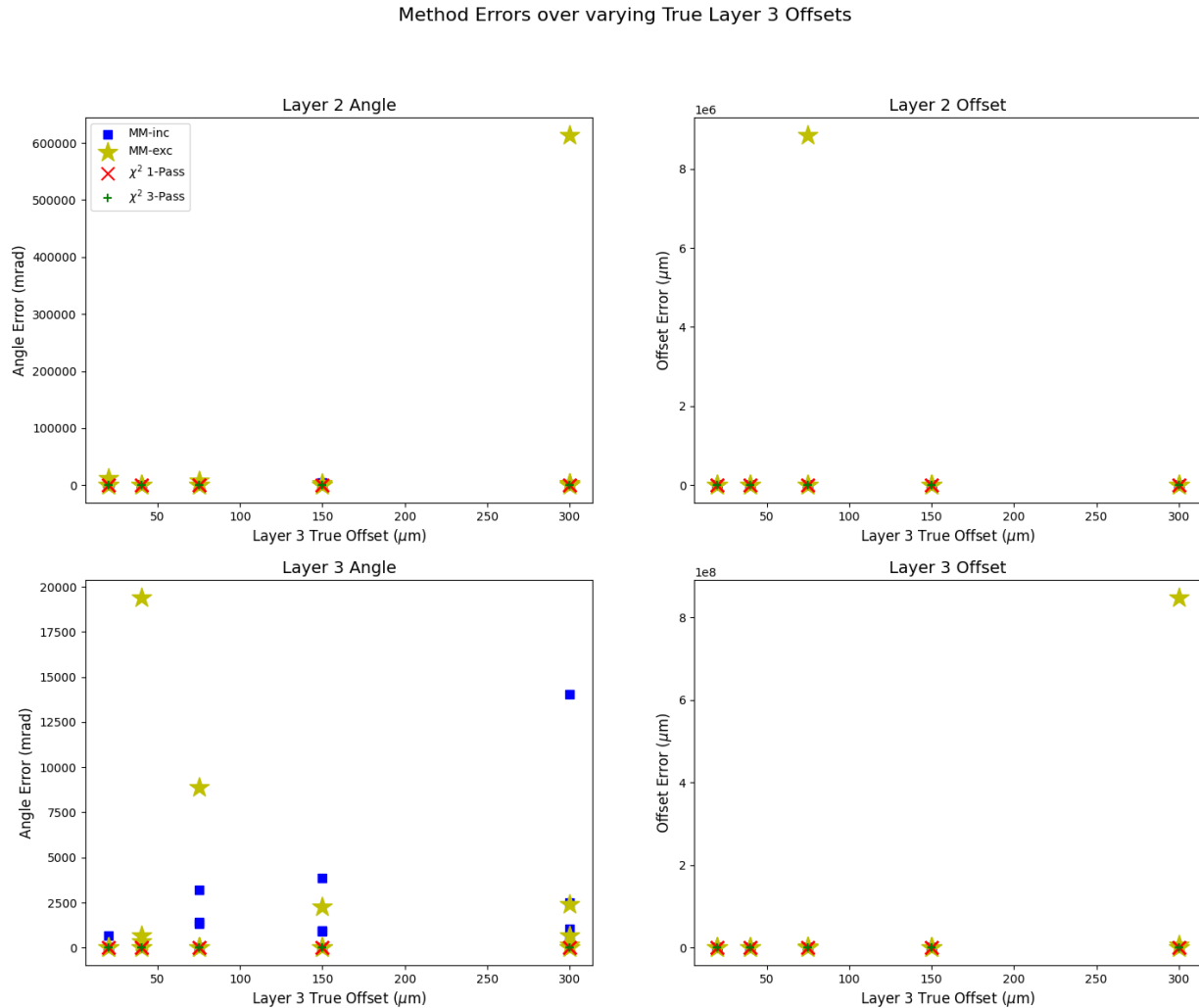


Figure 6.5: Errors from all four methods as true angle varies from 0.00 to 0.40 mrad. As with Figures 6.3 and 6.4, a large outlier in the matrix method using exclusive residuals make interpretation difficult. Plot with varying true offset in Appendix C.

Figure C.5.

By removing the matrix method using exclusive residuals from Figure 6.4, we can now compare the other three methods more closely. This is done in Figure 6.7, and two

Method Accuracy over varying True Layer 3 Offsets

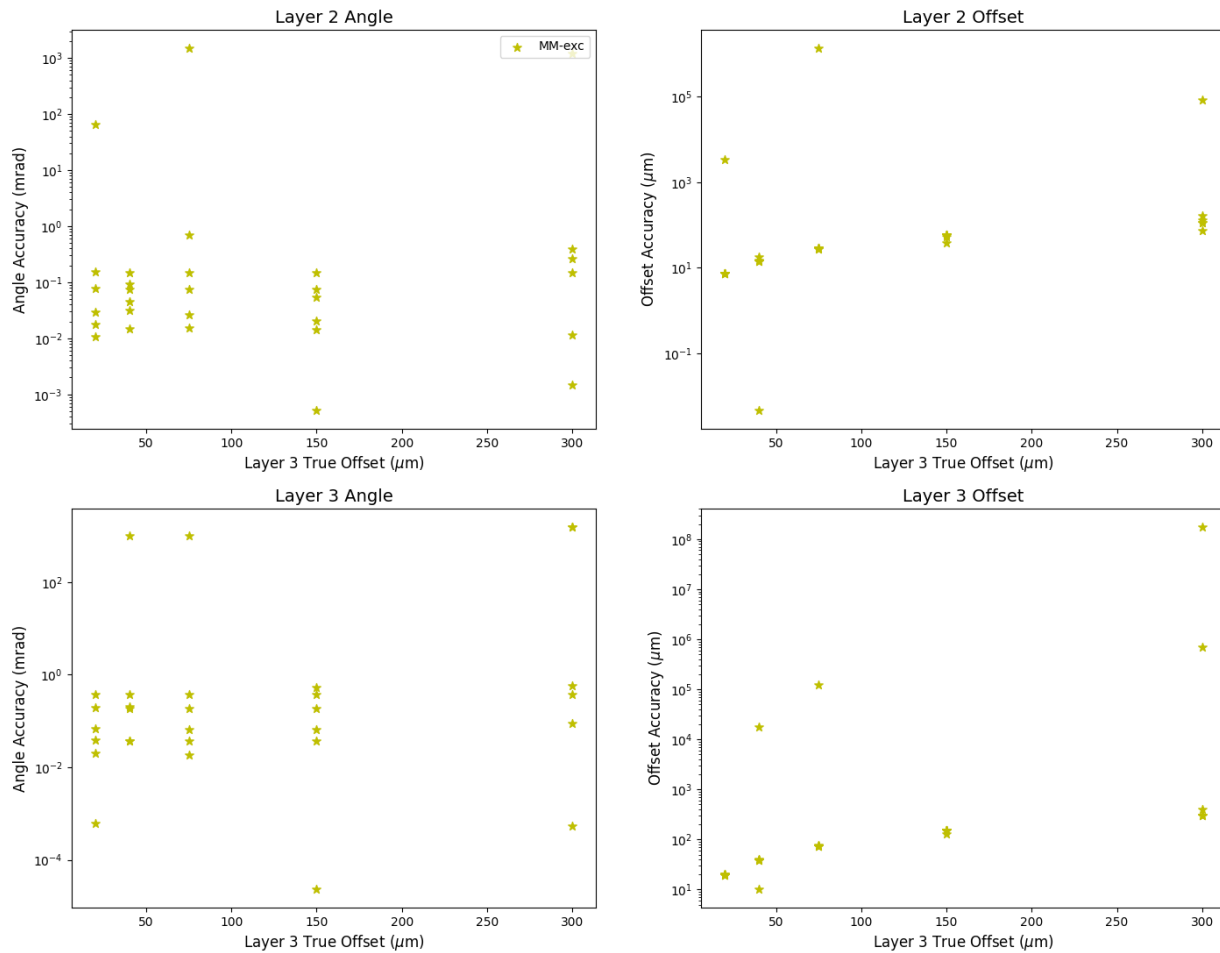


Figure 6.6: Semi-log plot of accuracy results from the matrix method using only exclusive residuals. Results span a wide range of magnitudes. Plot with varying true angle in Appendix C.

observations are made. First, there seems to be very little difference between the 1-Pass and 3-Pass χ^2 minimization results. This warrants further investigation by examining just the two χ^2 -based methods alone. Second, a large outlier exists for the remaining matrix

Method Accuracy over varying True Layer 3 Offsets

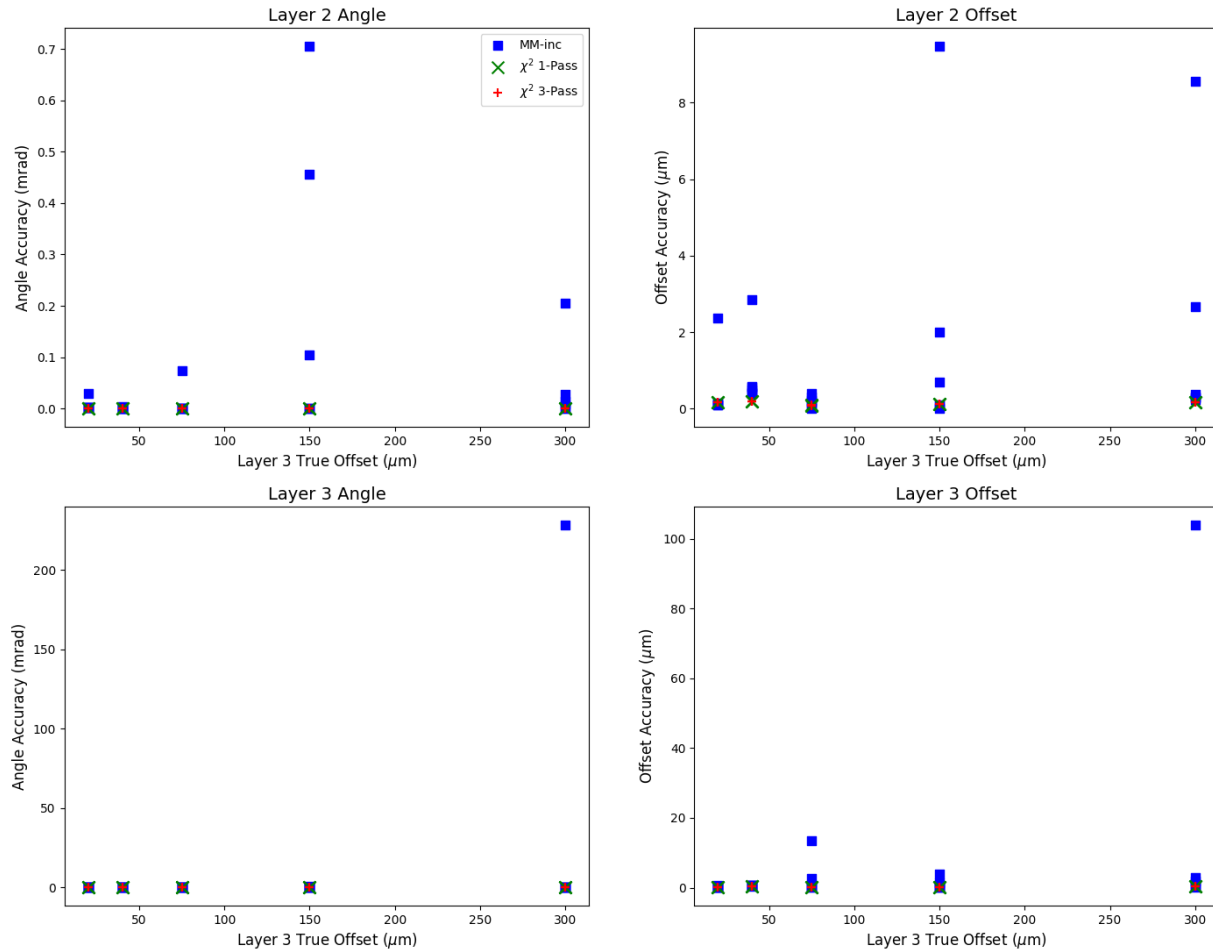


Figure 6.7: Accuracy results from the matrix method using inclusive residuals and the χ^2 -based methods, varying over Layer 3 Offsets. A large outlier for the matrix method suggests potential consistency issues. The similarities between the χ^2 -based methods warrant further investigation.

method at (0 mrad, 300 μm). It is easy to dismiss these results as outliers; however, this result should also be kept in mind, as it could indicate a potential consistency issue with

this method.

1-Pass and 3-Pass χ^2 Minimization Methods

Method Accuracy over varying True Layer 3 Rotations

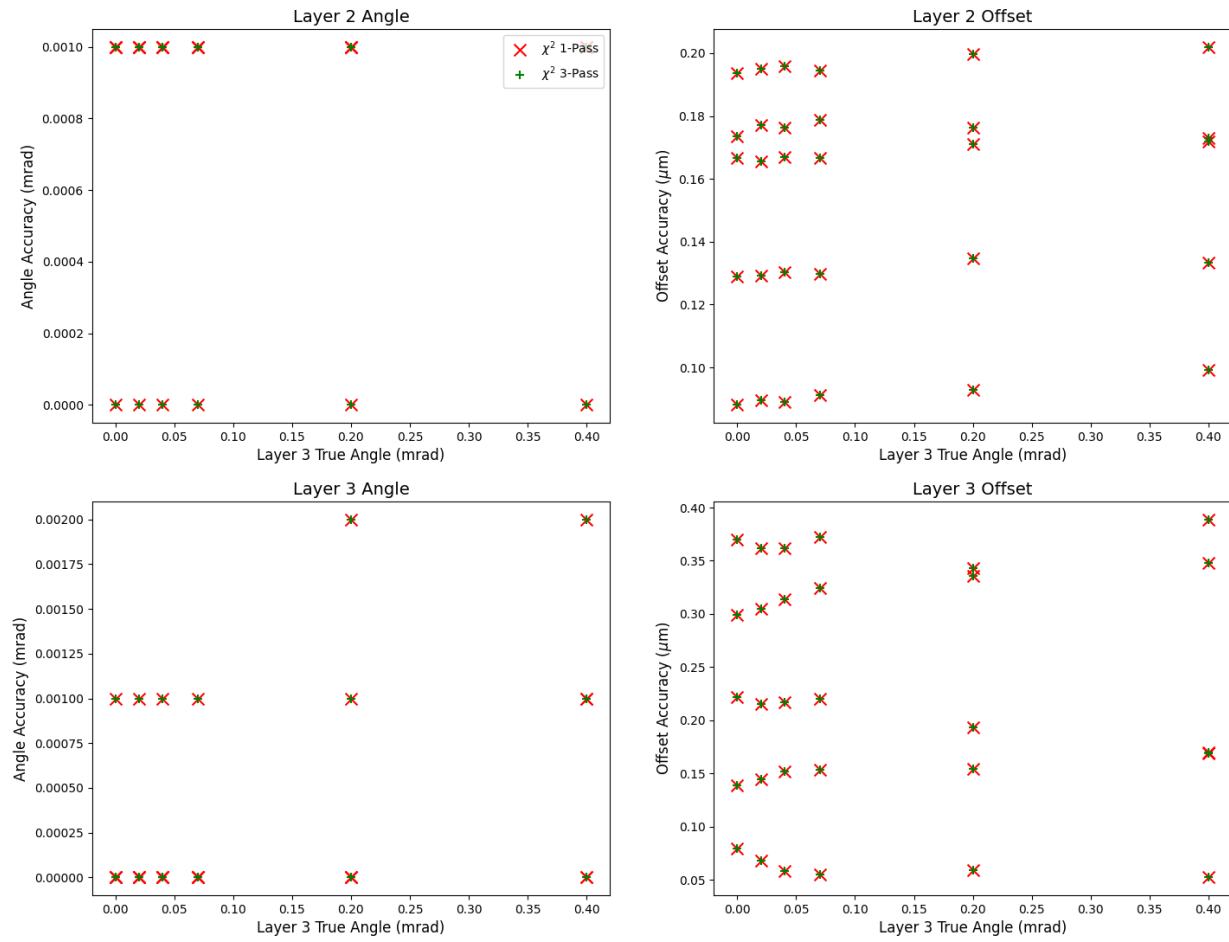


Figure 6.8: Accuracy of the χ^2 -based methods over varying Layer 3 rotation. Note the complete overlap of the points. Plot with varying true offset in Appendix C.

The accuracies of the 3-Pass and 1-Pass methods are compared in Figure 6.8. Figure 6.8

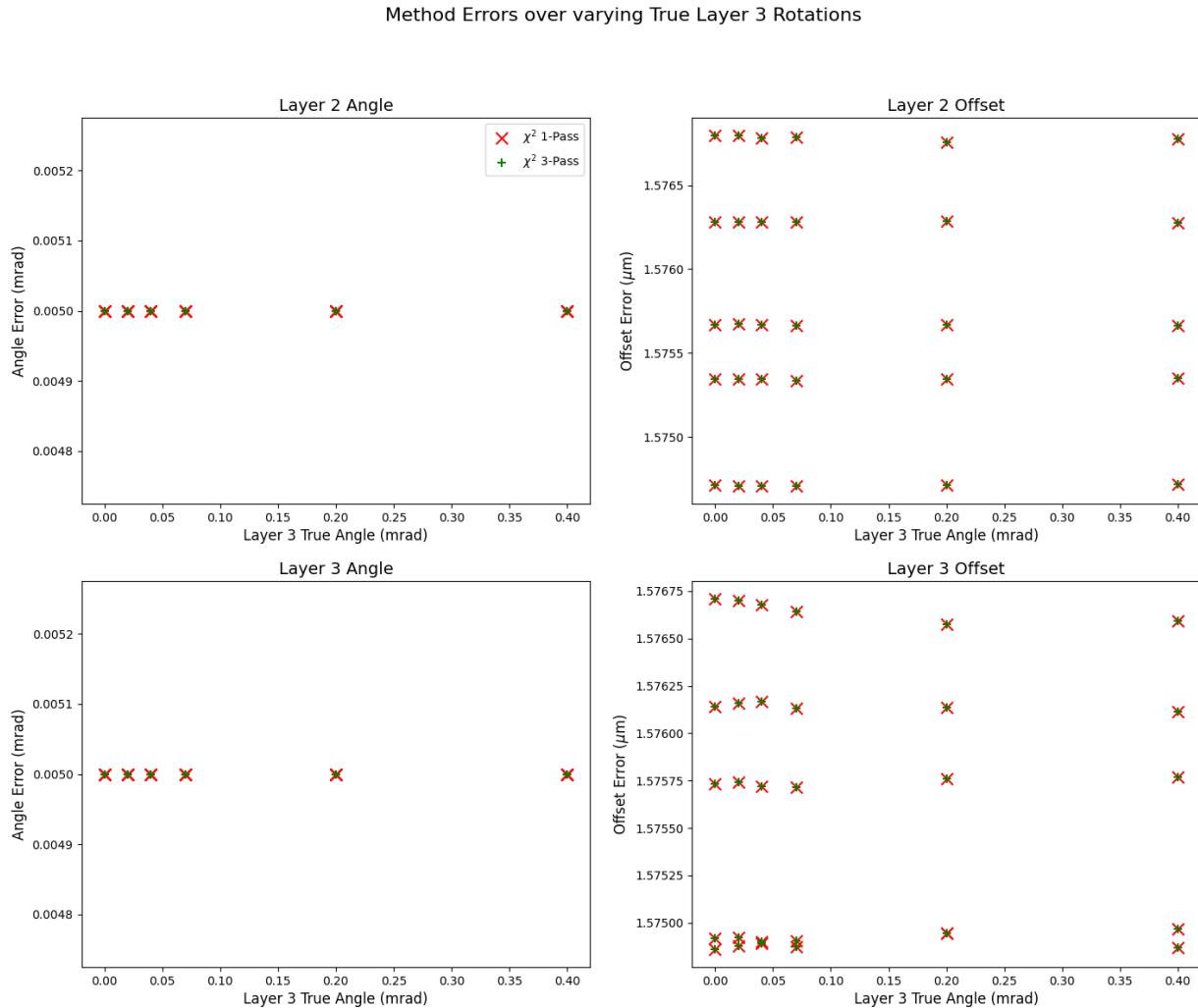


Figure 6.9: Errors of the χ^2 -based methods over varying Layer 3 rotation. Similar to Figure 6.8, note the complete overlap of the points. Plot with varying true offset in Appendix C.

shows no meaningful difference between the two, and an examination of the raw data also shows the exact same results between the two. At worst, the accuracy of the methods in predicting the Layer 2 zero-misalignment is around 0.001 mrad and about 0.2 μm , while the accuracies of the methods in predicting the Layer 3 misalignments are about 0.002 mrad and

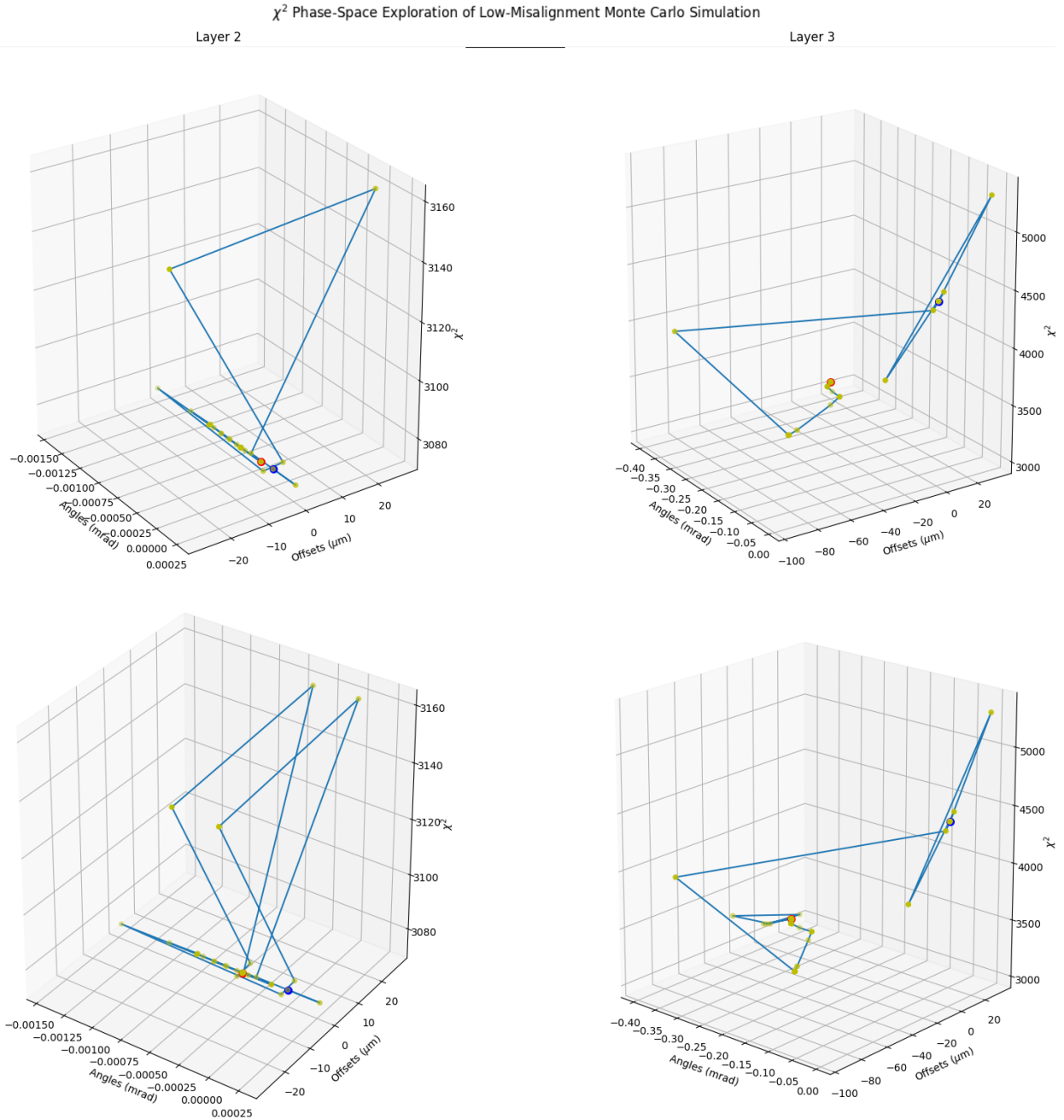


Figure 6.10: Phase Space Exploration of the (top) 1-Pass and (bottom) 3-Pass χ^2 minimizations. The third minimization is seen as the second triangle in the χ^2 -Offset plane.

0.4 μm . Furthermore, across all results, accuracy does not seem to behave monotonically. The results with accuracy of 0.0000 shows that the program agrees with truth up to the precision of TMinuit.

Similar results are found when comparing errors, as in Figure 6.9. When comparing the 1-Pass to 3-Pass data points, there is no difference between the errors. Additionally, the errors are remarkably consistent across all the runs, being 0.005 mrad for angle across all 36 simulations and between 1.5745 and 1.5770 μm for offset. Again, examination of the raw data shows the exact same predictions made by both methods. To ensure the χ^2 3-Pass method was indeed performing all three minimizations, the (θ, y_0) trajectory was plotted, as shown in Figure 6.10. When TMinuit explores a phase space, it varies the parameters one at a time before starting a general minimization. The second triangle present in the 3-Pass plot and not in the 1-Pass is the univariate exploration in the offset direction of the third minimization. This will be further discussed in Subsection 6.2.3.

Moving forward, the two methods are treated as functionally identical. We can now turn to the matrix method using inclusive residuals.

Matrix Method with Inclusive Residuals

The matrix method with inclusive residuals, henceforth referred to simply as the matrix method, had an outlier that is clearly visible in Figure 6.7. This outlier had no effect on Layer 2, but had an absolute difference of approximately 250 mrad and 100 μm in Layer

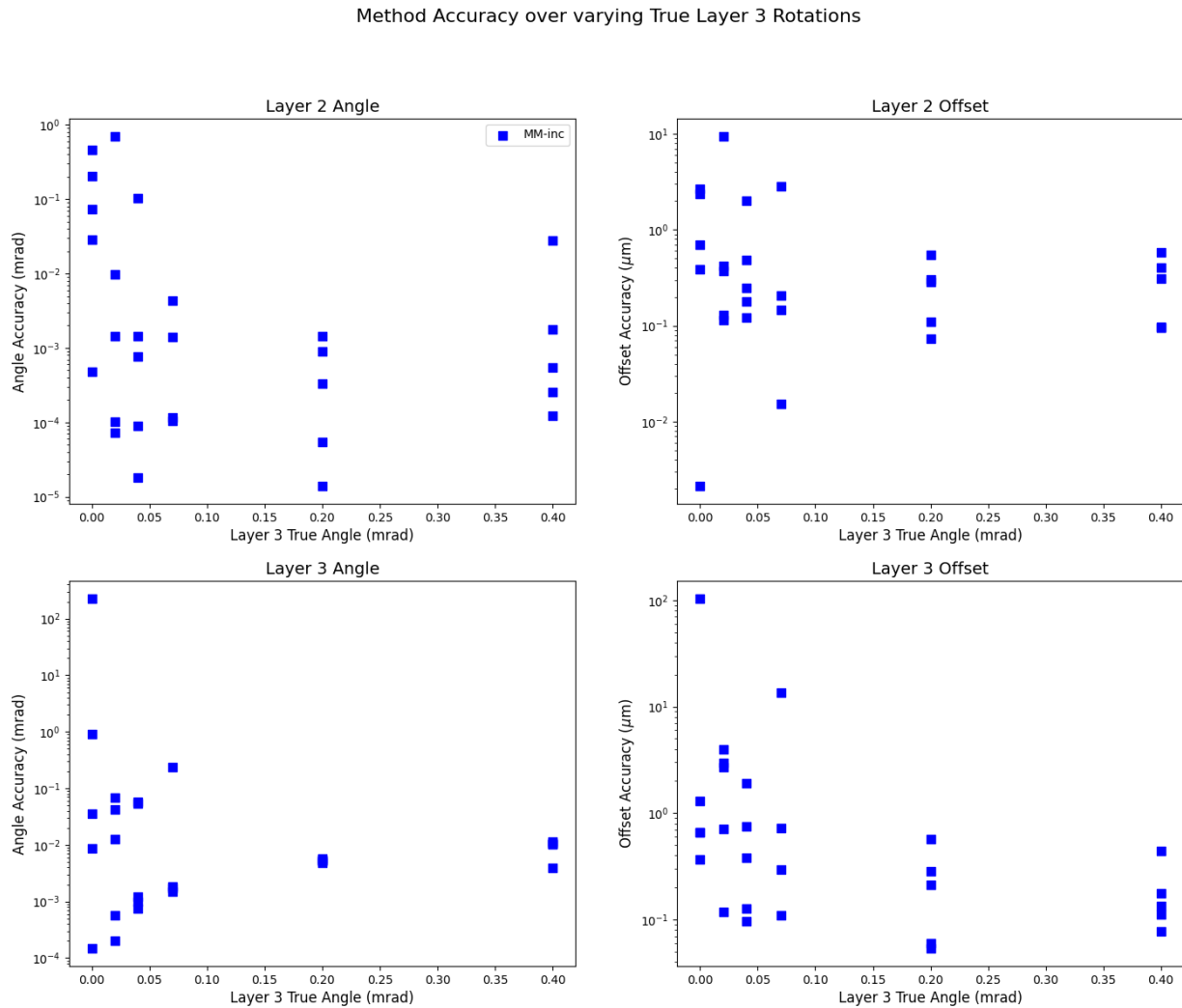


Figure 6.11: Accuracy of matrix method using inclusive residuals over varying Layer 3 rotation. Comparatively large method absolute differences are mostly present at low angles. Plot with varying true offset in Appendix C.

3. In continuing this analysis, we can remove this outlier, but keep the outlier noted as a potential inconsistency in performance.

The outlier is removed and the matrix method is isolated in Figure 6.11, showing that

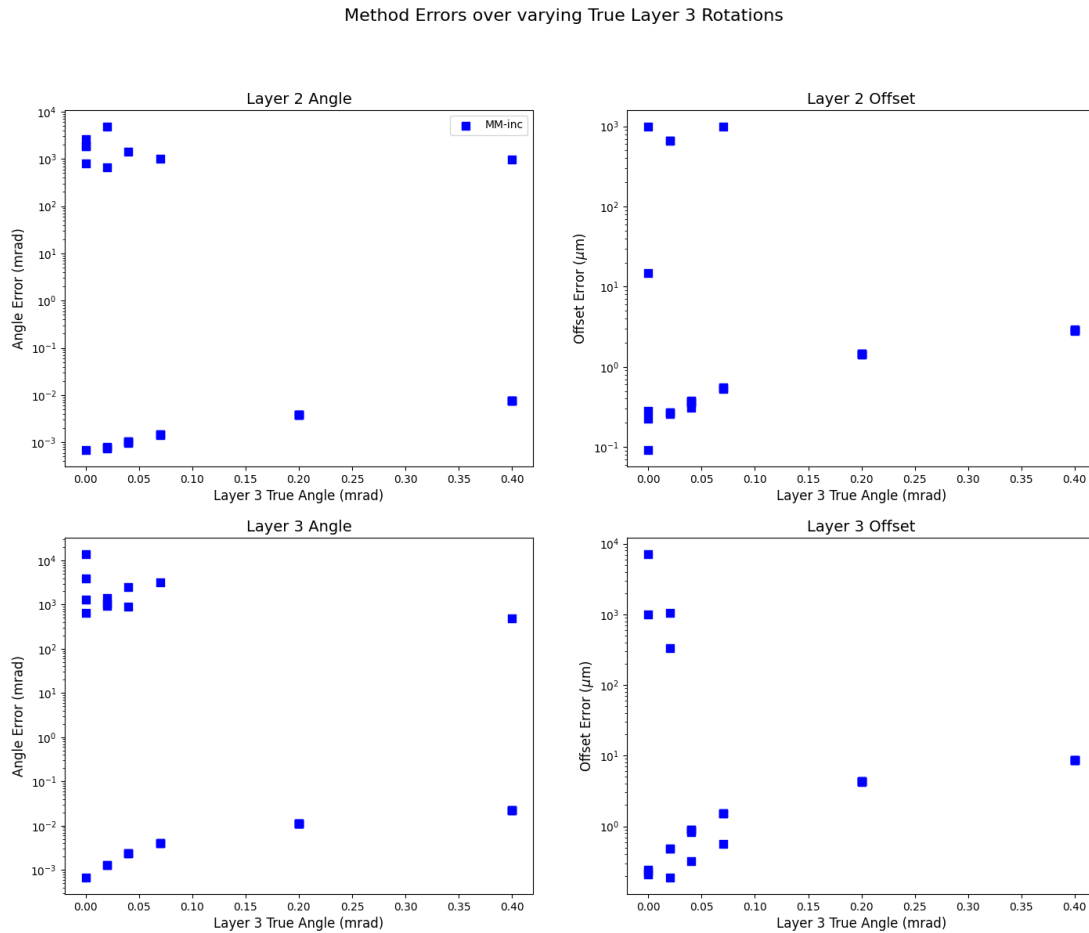


Figure 6.12: Errors of the matrix method using inclusive residuals over varying Layer 3 rotation. Similar to Figure 6.11, comparatively large method errors are mostly present at low angles. Plot with varying true offset in Appendix C.

this data is more consistent. At worst, the accuracy of the matrix method in predicting the Layer 2 zero-misalignment is around 0.8 mrad and about 10 μm, while the accuracy of the matrix method in predicting the Layer 3 misalignments is about 1 mrad and 14 μm. Furthermore, like the χ^2 methods, accuracy does not seem to behave monotonically.

However, the errors of the matrix method are not as well-behaved. The angle errors span several orders of magnitude from 10^{-4} to 10^3 mrad. Furthermore, there are large errors over more than just one outlier, which is problematic when considering consistency. To complicate things further, the worst errors are outside of tolerance, making any predictions from the matrix method worthless.

At this point, when comparing using inclusive vs. exclusive residuals in the matrix method, inclusive residuals outperform the exclusive residuals. However, the errors of both versions are seemingly too imprecise to draw any meaningful conclusions. Nevertheless, as we continue to compare the matrix method to the χ^2 minimization method, only the matrix method using inclusive residuals will be considered.

Comparing χ^2 Minimization to the Matrix Method

The data presented in Figures 6.13, 6.14, 6.15 and 6.16 are reiterations of data already presented, with the purpose of having the data side-by-side for comparison's sake. Two sets of offset values are of interest. Looking at Figures 6.13 and 6.14, the more inaccurate predictions of the matrix method become apparent. However, the matrix method also sometimes performs really well, with angular accuracy around 10^{-4} mrad and offset accuracy of $10^{-1}\mu\text{m}$. With one exception (ie. Layer 3 Angle Predictions at 0.2 mrad), the χ^2 predictions seem to be more consistent than the matrix method. The χ^2 method also seems to perform similarly across most offset and angle values, displaying a lower spread in

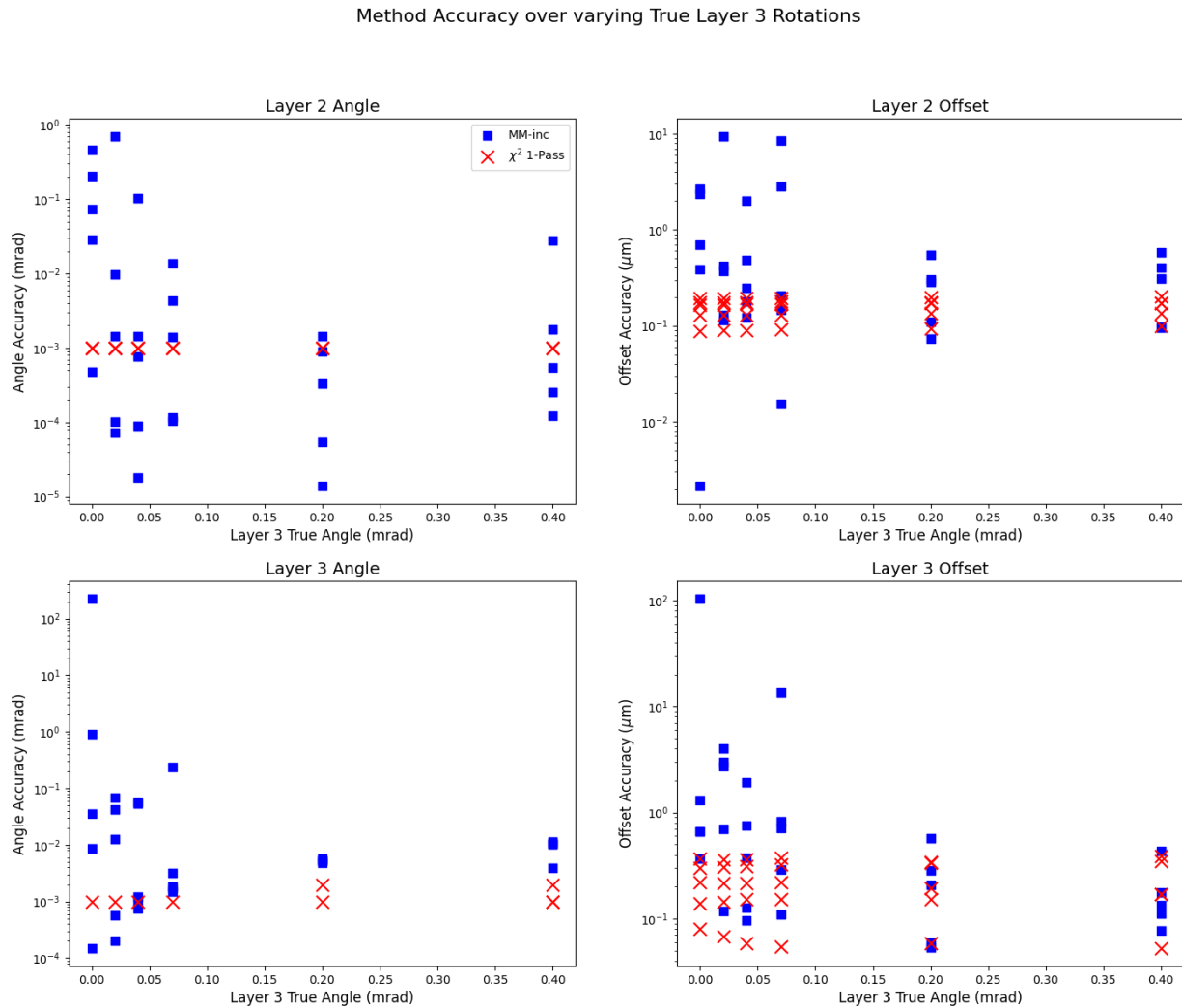


Figure 6.13: Semi-log plot of accuracy of the χ^2 1-Pass Method and matrix method using inclusive residuals over varying Layer 3 rotation.

their predictions when compared to the matrix method.

Figures 6.15 and 6.16 show that the errors of the χ^2 method are consistently lower than in the matrix method. Furthermore, the errors in the matrix method seem to get more

Method Accuracy over varying True Layer 3 Offsets

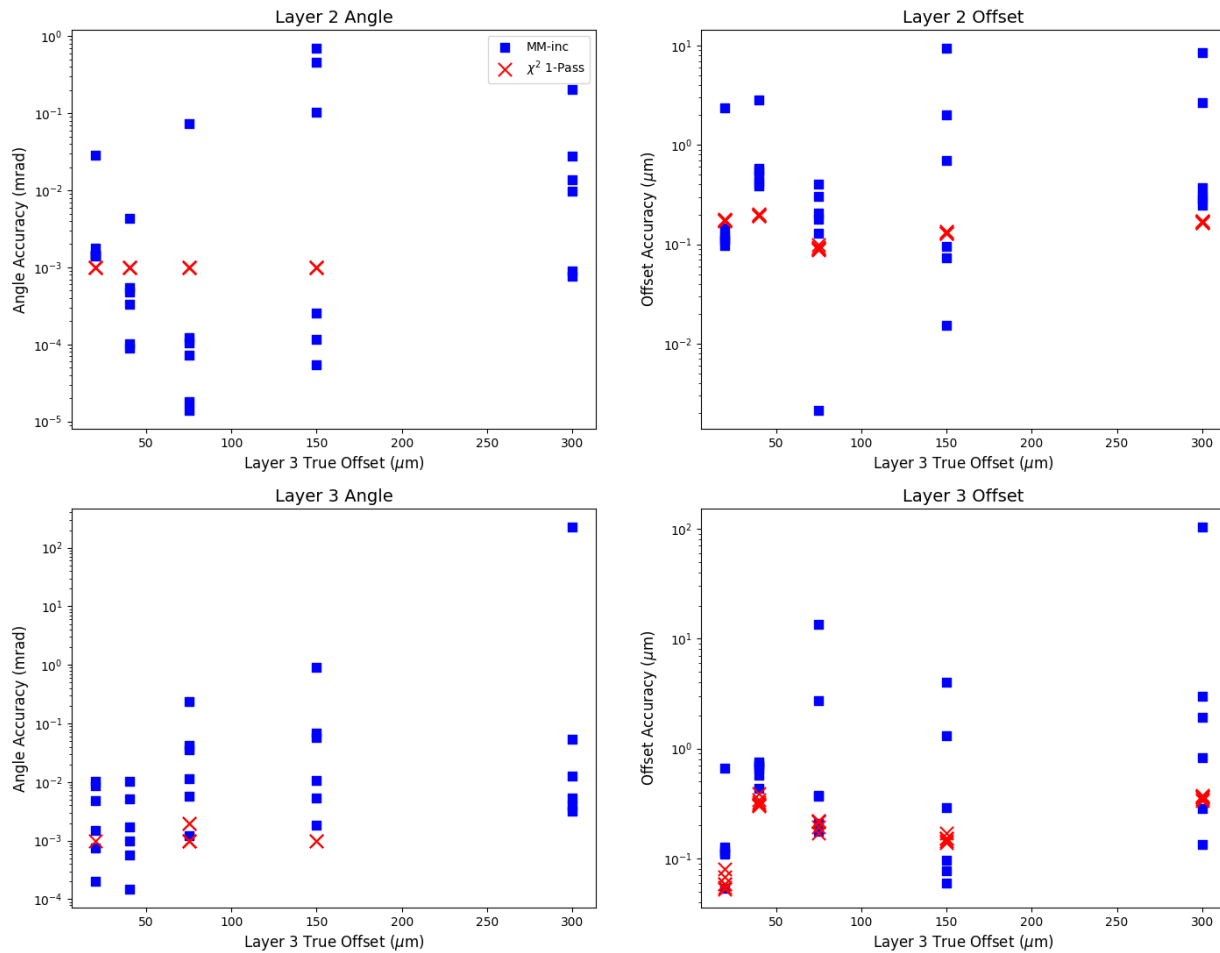


Figure 6.14: Semi-log plot of accuracy of the χ^2 1-Pass Method and matrix method using inclusive residuals over varying Layer 3 offset.

inconsistent with higher Layer 3 Offset. The matrix method performs relatively well at 0 μm Layer 3 offset, with errors as low as 10^{-3} mrad and 10^{-1} μm .

Method Errors over varying True Layer 3 Rotations

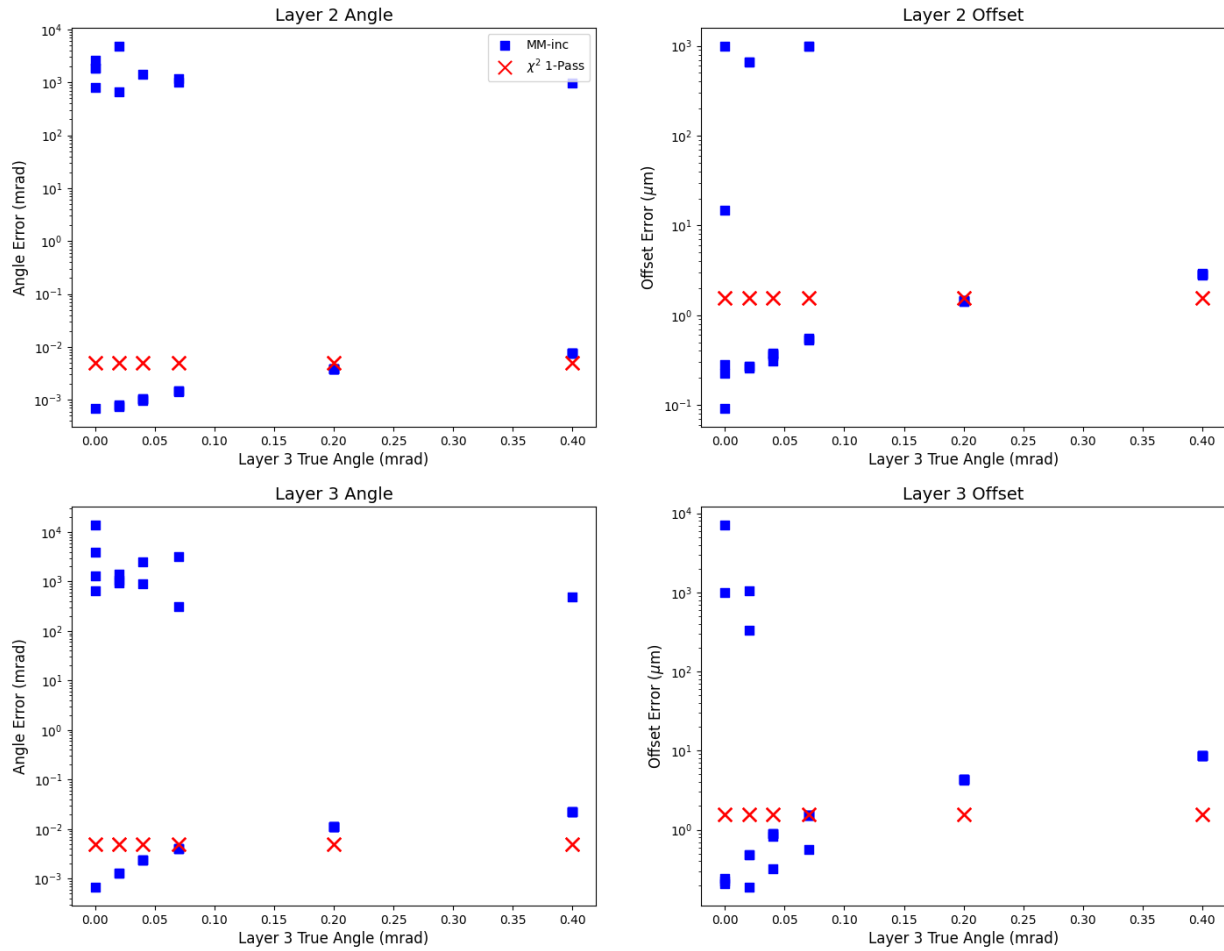


Figure 6.15: Semi-log plot of the errors of the χ^2 -based methods over varying Layer 3 rotation.

Method Errors over varying True Layer 3 Offsets

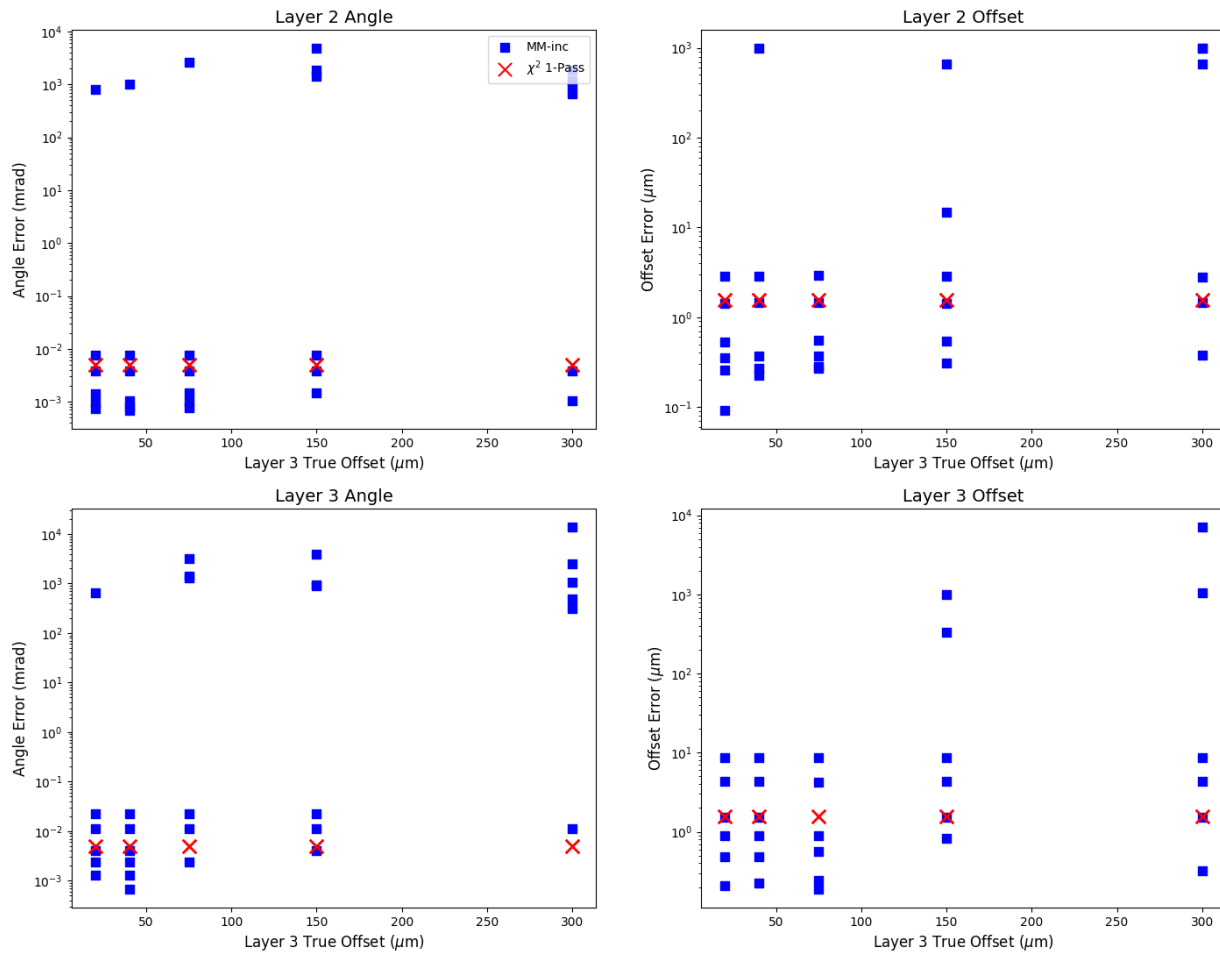


Figure 6.16: Semi-log plot of the errors of the χ^2 -based methods over varying Layer 3 offset.

6.2.3 Discussion

Matrix Methods

The hypothesis that the matrix method would perform better at lower angles is not supported by the evidence, as accuracy does not seem to increase at low Layer 3 rotations. The initial

reasoning for this hypothesis is that because the matrix method relies on a small-angle approximation, larger angles would lead to a breakdown in this method. However, at the angles in question, the small-angle approximation may still be appropriate. As a comparison, $\tan 0.001 \approx 0.001 + 3.3 \times 10^{-10}$. In other words, the assertion that $\tan \theta \approx \theta$ is well supported at values above those tested in this experiment.

χ^2 Methods

The 1-Pass and 3-Pass χ^2 minimizations were shown to be functionally identical across all 36 Monte Carlo simulations, once again subverting expectations. This suggests that neither reducing the step size of TMinuit nor initializing a minimization closer to the true value has an effect on error size. With that being said, it can be concluded that χ^2 1-Pass is the most consistent over all the methods. While the matrix method had low absolute differences that were at times lower than χ^2 , the χ^2 method was much more consistent in its results. The errors were also always the same with the χ^2 method, although this could be because the data are all idealized Monte Carlo simulations.

The reasons for the higher consistency of the χ^2 method is unclear, but one possibility are the checks and cuts implemented in the code. Across all simulations, 85% of events were analyzed, similar to the result from the original implementation experiments described in Subsection 5.3.3. Although the cuts and checks reduce the available data set, the data that are left behind are more likely to be “good” data. The matrix method does not perform

these checks and cuts, and therefore may use a substandard data set.

With respect to the χ^2 minimization method, several other things are of note. The accuracy of the method seems to vary only with offset, and not so much with rotation. Even so, there does not seem to be a clear correlation between accuracy and known offset. Additionally, as seen in the x -axis offset plots, the accuracy of the Layer 2 misalignment predictions (zero offset, zero rotation) does not seem to vary with changes in Layer 3 angle. At the bottom of Figure 6.14, there does not seem to be much variation in the accuracy of the angle prediction, despite each x -value having six different Monte Carlo simulations. This is as expected, as the χ^2 method treats the unfixed layers separately. In other words, the Layer 2 misalignment should not consider Layer 3.

6.3 Characterization of sTGC Quadruplets using χ^2 Minimization

Now equipped with the 1-Pass χ^2 minimization method, the Canadian-made sTGC quadruplet can be characterized in terms of their misalignments using real cosmic ray data. The program was run over the 3100 V CosmicsAnalysis data of all quadruplets tested at McGill, and the results were binned in Figure 6.17. The results show good consistency across all quadruplets, with the misalignments being on the same order of magnitude as those manufactured by the Chinese NSW group [89]. Average misalignment values are

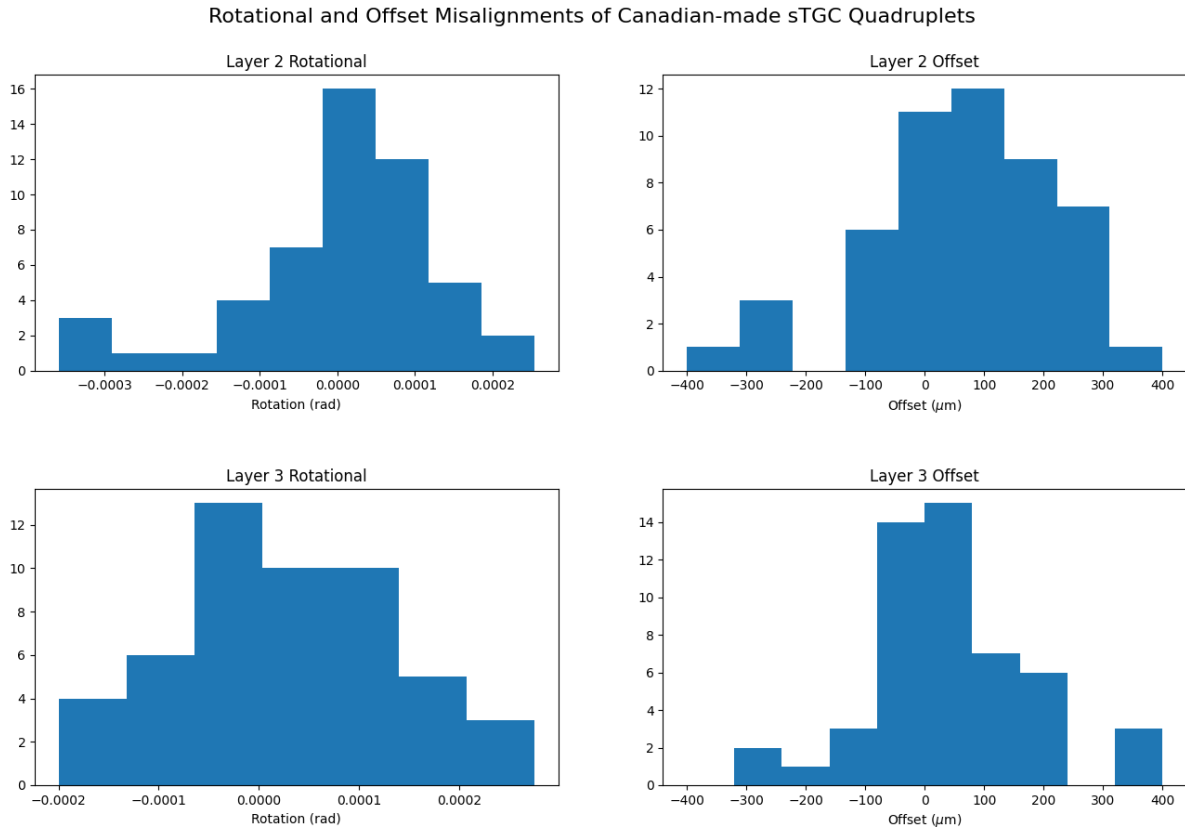


Figure 6.17: Distribution of Misalignments of Canadian-made sTGC Quadruplets, as calculated by the χ^2 minimization method. 52 quadruplets are represented here.

listed in Table 6.3. Furthermore, the errors on almost all quadruplets are around 0.03 mrad for the angle and 10 μm for the offset. A full table of results is given in Appendix B.

For various reasons, some quadruplet data were not included in the histogram. These excluded quadruplets are listed in Table 6.4. Because only 3100 V data was considered for the presented data analysis, the 2900 V data was also checked for these runs. All quadruplets that had problems at 3100 V also had problems at 2900 V. Quadruplets were skipped over if they had an absolute predicted rotation that was too high (defined as 0.6 mrad or higher),

Misalignment	Value
Layer 2 Rotation	0.003 ± 0.130 mrad
Layer 2 Offset	130 ± 393 μm
Layer 3 Rotation	0.027 ± 0.113 mrad
Layer 3 Offset	28 ± 147 μm

Table 6.3: Average Misalignments of Canadian-made sTGC quadruplets, as calculated by the χ^2 minimization method.

an offset that was too high (defined as eight-times tolerance ($600 \mu\text{m}$) or higher), or an offset error that was too high. 0.6 mrad was chosen because the χ^2 minimization program does not explore beyond ± 0.6 mrad.

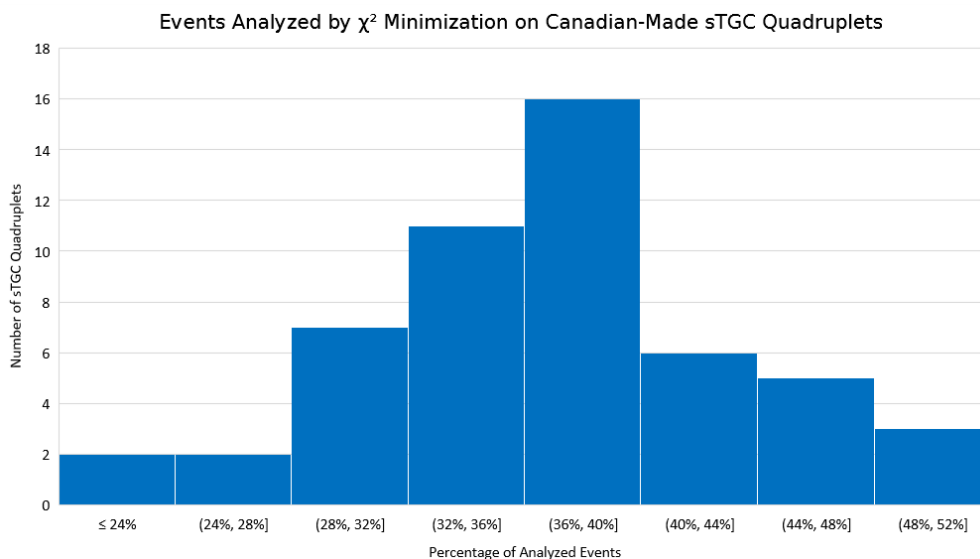


Figure 6.18: Distribution of percentage of events analyzed by the χ^2 minimization method over all the sTGC quadruplets. The average over all runs is 38%. 52 quadruplets are represented here. QS3P01 and QS3P05 are omitted from this graph.

Before attempting to explain the anomalies in the predicted misalignments, it is useful

Skipped Quadruplet - Reason	Value (mrad or μm)	Error (mrad or μm)
QS3P01 - L2 Offset Error too high	0	10000
QS3P01 - L3 Offset Error too high	0	10000
QS3P04 - L2 Nonsense Rotation	0.6	0.001
QS3P04 - L3 Nonsense Rotation	0.6	0.001
QS3P05 - No Data	–	–
QS3P13 - L2 Large Offset	2640	20
QL2C12 - L2 Large Offset	652	2

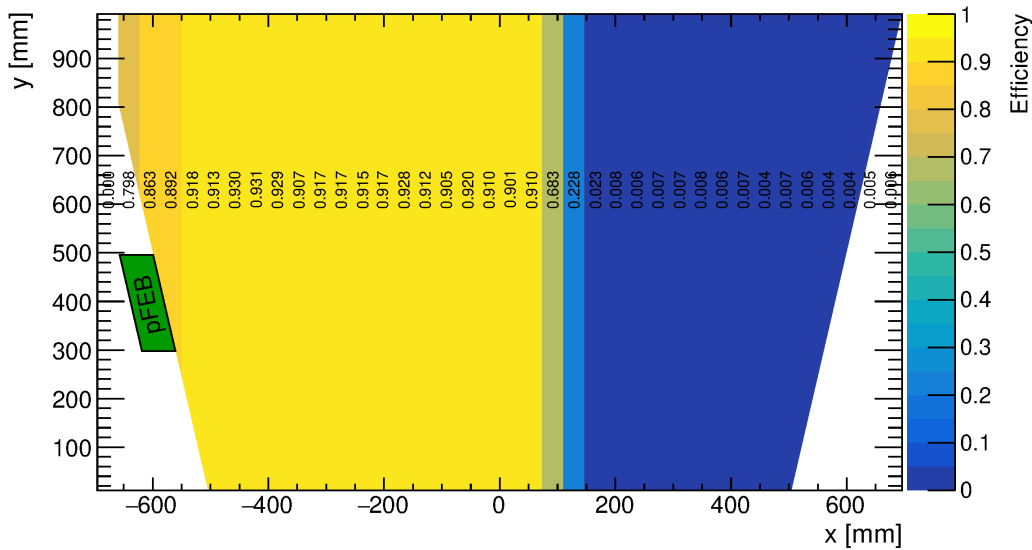
Table 6.4: Skipped sTGC Quadruplets from Figure 6.17.

to determine the percentage of events analyzed by the χ^2 minimization method. Figure 6.18 shows the distribution of percentages of analyzed events over all quadruplets. A quadruplet with an anomalous result may be explainable by a lower percentage of accepted events.

The reasons for skipping most of these runs can be explained. The files for QS3P01 contain no track data, and would exit out of χ^2 minimization program with 0/0 events analyzed. This is consistent with the fact that the χ^2 value was 0 across all tested parameters. QS3P05 had no data files associated with it.

QS3P04 had nonsense rotations that exceed the bounds of the χ^2 minimization method for both layers. Upon further investigation, it was discovered that almost one-third of the Layer 4 Wires were disconnected at Carleton University due to damage. Because the analysis assumed Layers 1 and 4 were fixed, this presumably decreased the number of eligible tracks available for analysis. The impact of these disconnections is shown in Figure 6.19, an efficiency plot of Layer 4. Indeed, only approximately 15% of the 452 741 events

were analyzed. Presumably, one could attribute the rotation being too high to the removal of many tracks. The offsets for QS3P04 were outside of tolerance (Layer 2: $-244 \pm 4 \mu\text{m}$; Layer 3: $-407 \pm 4 \mu\text{m}$).



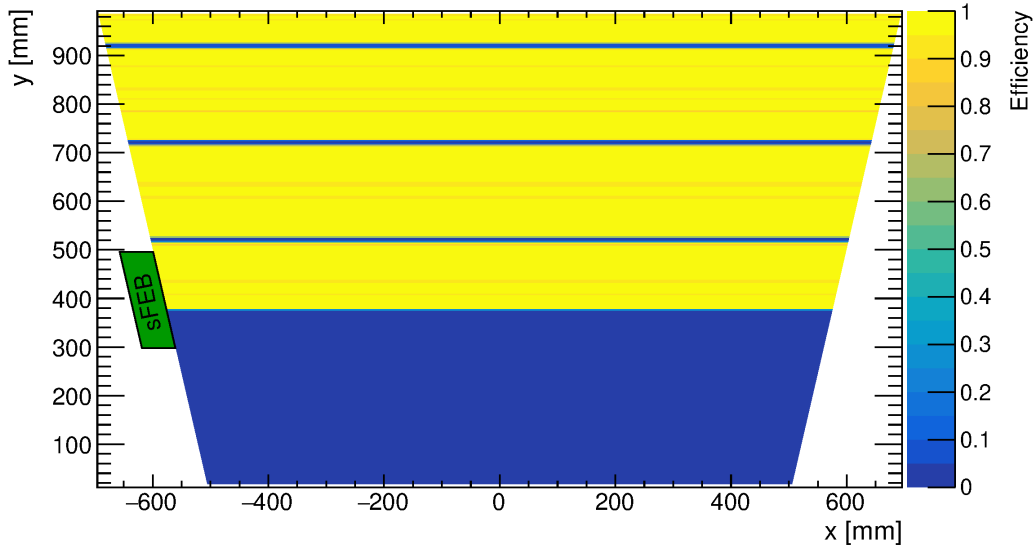


Figure 6.20: Efficiency plot of QS3P13's Layer 2 strips. An entire section of the quadruplet has near zero-efficiency.

Finally, QL2C12 had a large Layer 2 offset ($652 \pm 2 \mu\text{m}$). Testing shows that two wires in Layer 2 showed 0 hits during cosmics run testing, as show in Figure 6.21. However, other quadruplets had two or more wires disconnected (eg. QL2C8, QL2P5) and still gave reasonable results. This suggests that the disconnected wires cannot be the sole reason for the large offset. That being said, the offset is still in the same order of magnitude as some other misalignments, and therefore may just be the product of systematic variation in construction. Further investigation may be required.

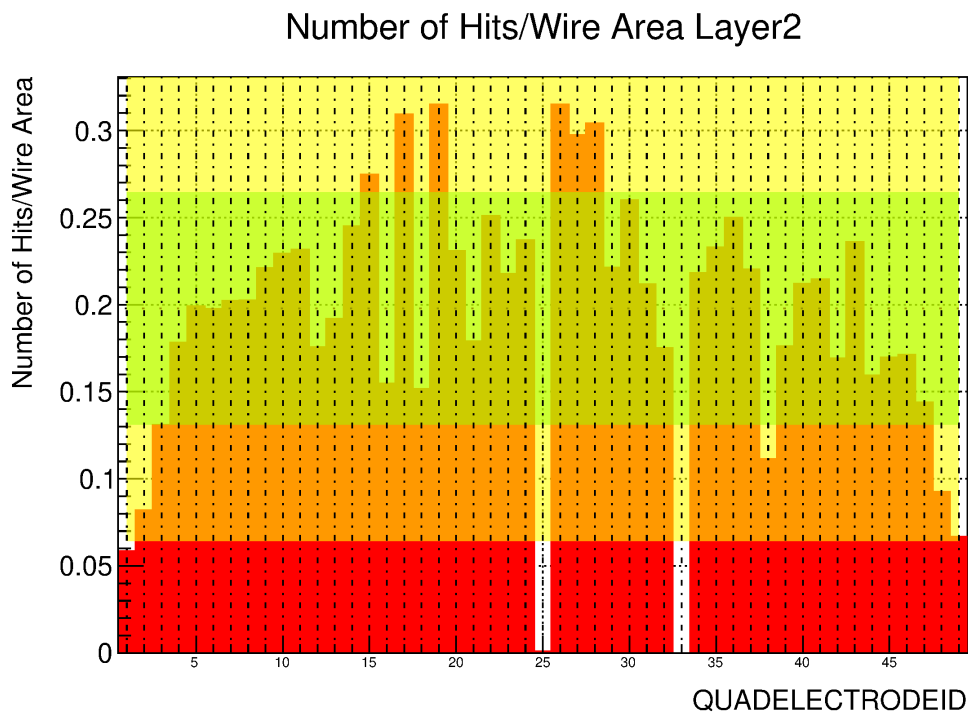


Figure 6.21: Number of Hits / Wire Area plot of QL2C12’s Layer 2 wires. Two wires registered zero hits during cosmic testing. However, this behaviour is seen with other quadruplets with reasonable misalignment values.

6.3.1 Future Work

Future work could go into abstracting the χ^2 minimization code. Currently, the code uses four different χ^2 functions, as described in Subsection 5.3.2. Pragmatically, these functions perform well; aesthetically, the code is simply inelegant. Future work in improving the program could go into abstracting the four χ^2 functions into one function with another parameter.

Throughout this project, it was assumed that only rotation and offset would play a role

in misalignments. However, the other possible misalignments outlined in Figure 4.4, pitch scale and non-parallelism, can still be present in a quadruplet layer. These misalignments are harder to characterize, as there is no easy physical interpretation of a pitch scale or non-parallelism, other than one-off construction errors on certain wires. One could envision potentially characterizing the pitch scale and non-parallelism of each individual wire of a quadruplet. This would provide a more accurate model of the misalignments.

Finally, these results can be compared to data collected by X-ray alignment studies at CERN. The misalignments reported in this work are relative misalignments: misalignments of Layers 2 and 3 with respect to an internal reference frame, Layers 1 and 4. In CERN's alignment studies, X-rays take the place of cosmic ray muons. Because these X-rays come from a known, well-characterized source fixed on an external reference frame, these results have the potential to provide absolute misalignment measurements with respect to the alignment platform [90].

Analysis of the X-ray results by χ^2 minimization is currently an ongoing project at McGill. Lia Formenti is comparing the X-ray strip misalignment results with McGill's cosmics strip misalignment results by comparing mean residuals across area bins. Recent results suggest that there is a good correlation between X-ray and cosmics data results. However, the results from the X-ray studies have high uncertainties and are binned into small areas; cosmics data have lower uncertainties and higher statistics. Thus, there is interest in using cosmics data to validate the X-ray studies and the resultant absolute misalignment measurement. Paul

Deguire, a summer undergraduate student, has continued working on this project, using X-ray data and a χ^2 function with Lagrange multipliers to examine wire misalignments.

Chapter 7

Summary and Conclusion

To this day, the Standard Model serves as the pillar of physicists' understanding of the fundamental building blocks of matter. The desire to explore the subatomic realm described by the Standard Model led the international physics community to build the LHC and ATLAS, which resulted in groundbreaking results. Yet, with vast expanses of energy and luminosity regimes still unexplored, ATLAS and the LHC continued to upgrade their apparatus, leading to the development of the New Small Wheel and, ultimately, the sTGC quadruplets upon which this thesis is based.

Over the course of Long Shutdown 2, Monte Carlo simulations were used to develop, characterize, and evaluate two methods of determining the relative misalignments of sTGC quadruplets with respect to their outermost layers. By considering accuracy, errors, and consistency, the χ^2 minimization method was chosen to characterize these quadruplets.

With this method, the misalignments of the Canadian-made sTGC quadruplets formed the distribution shown in Figure 6.17. These misalignment results, compiled in Appendix B, will hopefully be cross-checked with X-ray tests performed at CERN, and consequently used to correct track information acquired from the New Small Wheel when the LHC powers on for Run 3.

At the time of writing, the New Small Wheels have already been lowered into the ATLAS cavern underground. The LHC will soon restart and with it, the hope that the future will shed some new light upon humanity's understanding of the natural world. As one meager component in this historical endeavour, the sheer magnitude of human effort and collaboration required by this undertaking comes to mind upon conclusion of this project. Thousands of people from across space and time have worked to bring to fruition, not only the New Small Wheel, not only the Hi-Luminosity LHC, but the forward march of scientific progress. One can feel humbled after this realization. However, it is through the tireless efforts of people, both meager and brilliant, ordinary and extraordinary, that science presses on. We can only hope that as the annals of history are written by the denizens of future eras, they too can look favourably into their future standing on the shoulders of giants.

Appendix A

Gitlab Links

Entire project available in the AlignmentStudies branch of the McGill-sTGC Gitlab:

https://gitlab.cern.ch/McGill-sTGC/tgc_analysis/-/blob/AlignmentStudies

Matrix Method source code available at:

https://gitlab.cern.ch/McGill-sTGC/tgc_analysis/-/blob/AlignmentStudies/

MatrixMethod/MM.cpp

χ^2 minimization source code available at:

https://gitlab.cern.ch/McGill-sTGC/tgc_analysis/-/blob/AlignmentStudies/

TrackAnalysisTemplate/TrackAnalysis.cpp

Appendix B

Misalignment Results of Modules

Table B.1: Misalignments of Canadian-made sTGC quadruplets using cosmics data

Run	L2 Angle (mrad)	L2 Ang Err (mrad)	L2 Offset (μm)	L2 Off Err (μm)	L3 Angle (mrad)	L3 Ang Err (mrad)	L3 Offset (μm)	L3 Off Err (μm)
QL2C01	-0.017	0.007	149	2	-0.026	0.007	60	2
QL2C02	0.149	0.007	232	2	-0.038	0.007	86	2

Table B.1 continued from previous page

Run	L2 Angle	L2 Ang Err	L2 Offset	L2 Off Err	L3 Angle	L3 Ang Err	L3 Offset	L3 Off Err
QL2C03	0.098	0.007	247	2	0.256	0.007	13	2
QL2C04	0.082	0.008	302	3	-0.131	0.008	-292	3
QL2C05	0.105	0.007	136	2	0.157	0.007	-221	2
QL2C06	0.034	0.006	108	2	0.112	0.006	-51	2
QL2C07	0.008	0.006	-18	2	-0.082	0.006	7	2
QL2C08	0.254	0.007	115	2	0.012	0.007	-97	2
QL2C09	0.075	0.007	217	2	0.064	0.007	-52	2
QL2C10	0.08	0.007	111	2	0.163	0.007	-56	2
QL2C11	0.033	0.006	-7	2	0	0.007	45	2
QL2C12	-0.327	0.005	658	2	-0.192	0.007	373	2
QL2C13	-0.232	0.006	306	2	-0.127	0.007	324	2

Table B.1 continued from previous page

Run	L2 Angle	L2 Ang Err	L2 Offset	L2 Off Err	L3 Angle	L3 Ang Err	L3 Offset	L3 Off Err
QL2C14	-0.358	0.006	297	2	-0.051	0.007	136	2
QL2C15	0.235	0.008	-45	3	0.159	0.008	-129	3
QL2C16	-0.082	0.007	-39	2	-0.2	0.007	-50	2
QL2C17	0.068	0.006	149	2	0.14	0.007	129	2
QL2C18	0.051	0.006	-369	2	0.089	0.007	141	2
QL2P01	-0.076	0.007	170	2	-0.018	0.007	60	2
QL2P02	-0.056	0.007	127	2	-0.049	0.007	-68	2
QL2P03	-0.044	0.007	323	2	0.058	0.007	41	2
QL2P04	0.047	0.006	38	2	-0.01	0.006	21	2
QL2P05	0.046	0.007	137	2	0.3	0.4	20	60
QL2P06	0.039	0.007	200	2	0.065	0.007	38	2

Table B.1 continued from previous page

Run	L2 Angle	L2 Ang Err	L2 Offset	L2 Off Err	L3 Angle	L3 Ang Err	L3 Offset	L3 Off Err
QL2P07	0.045	0.007	36	2	0.091	0.007	-15	2
QL2P08	0.131	0.007	93	2	0.059	0.007	49	2
QL2P09	0.069	0.007	-24	2	0.118	0.007	-268	2
QL2P10	0.168	0.006	94	2	0.132	0.008	378	2
QL2P11	-0.024	0.006	219	2	-0.198	0.006	-24	2
QL2P12	-0.006	0.006	167	2	-0.13	0.007	102	2
QL2P13	-0.068	0.007	82	2	-0.07	0.007	-76	2
QL2P14	0.062	0.006	-66	2	0.079	0.007	-36	2
QL2P15	0.091	0.007	-250	3	0.094	0.009	64	3
QL2P16	-0.002	0.006	93	2	-0.001	0.006	7	2
QL2P17	0.132	0.006	39	2	0.17	0.007	195	2

Table B.1 continued from previous page

Run	L2 Angle	L2 Ang Err	L2 Offset	L2 Off Err	L3 Angle	L3 Ang Err	L3 Offset	L3 Off Err
QL2P18	-0.199	0.006	3	2	-0.008	0.007	111	2
QS3P01	0	0.9	0	10000	0	0.9	0	10000
QS3P02	-0.1	0.2	-100	60	-0.2	0.2	-140	70
QS3P03	-0.011	0.009	59	3	-0.003	0.009	-2	3
QS3P04	0.6	0.001	-244	4	0.6	0.001	-407	4
QS3P05	–	–	–	–	–	–	–	–
QS3P06	0.011	0.007	1	2	0.113	0.007	106	2
QS3P07	0.027	0.008	235	2	0.096	0.008	28	2
QS3P08	-0.01	0.007	-81	2	-0.024	0.007	-14	2
QS3P09	-0.05	0.007	123	2	0.037	0.007	-12	2
QS3P10	-0.097	0.008	-54	3	0.012	0.008	-48	3

Table B.1 continued from previous page

Run	L2 Angle	L2 Ang Err	L2 Offset	L2 Off Err	L3 Angle	L3 Ang Err	L3 Offset	L3 Off Err
QS3P11	-0.111	0.007	13	2	-0.062	0.007	-115	2
QS3P12	0.16	0.008	80	3	0.231	0.008	160	3
QS3P13	-0.4	0.4	2640	20	0.023	0.007	-40	2
QS3P14	0.022	0.007	98	2	0.129	0.007	231	2
QS3P15	-0.09	0.007	-16	2	-0.004	0.007	170	2
QS3P16	-0.127	0.007	-52	2	-0.074	0.007	163	2
QS3P17	0.032	0.006	-248	2	0.059	0.007	61	2
QS3P18	0.071	0.006	-92	2	0.048	0.007	41	2
QS3P19	0.085	0.007	257	2	-0.155	0.004	171	2

Appendix C

Supplementary Plots

Method Errors over varying True Layer 3 Rotations

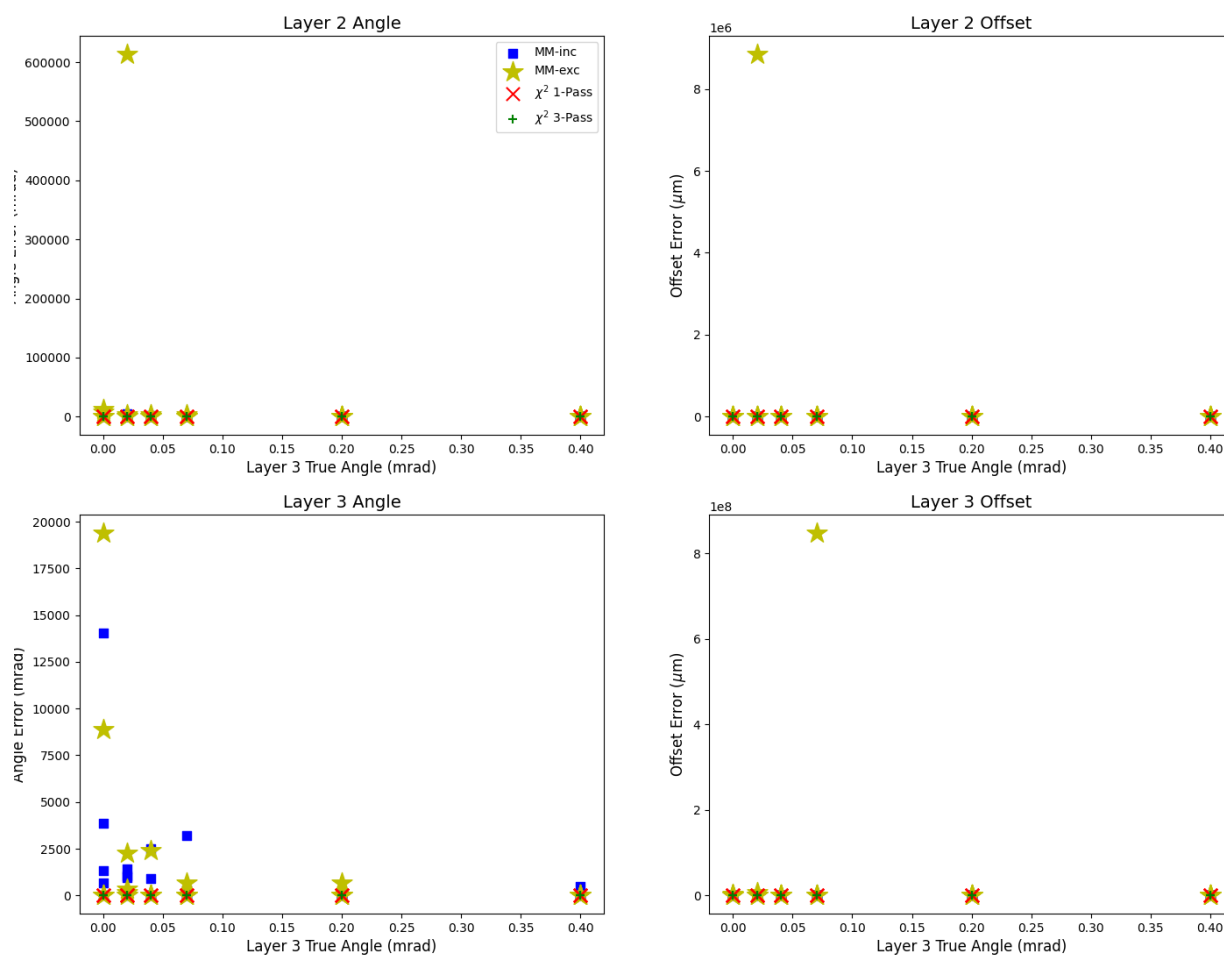


Figure C.1: Errors from all four methods as true angle varies from 0.00 to 0.40 mrad. Offset version shown in Figure 6.5.

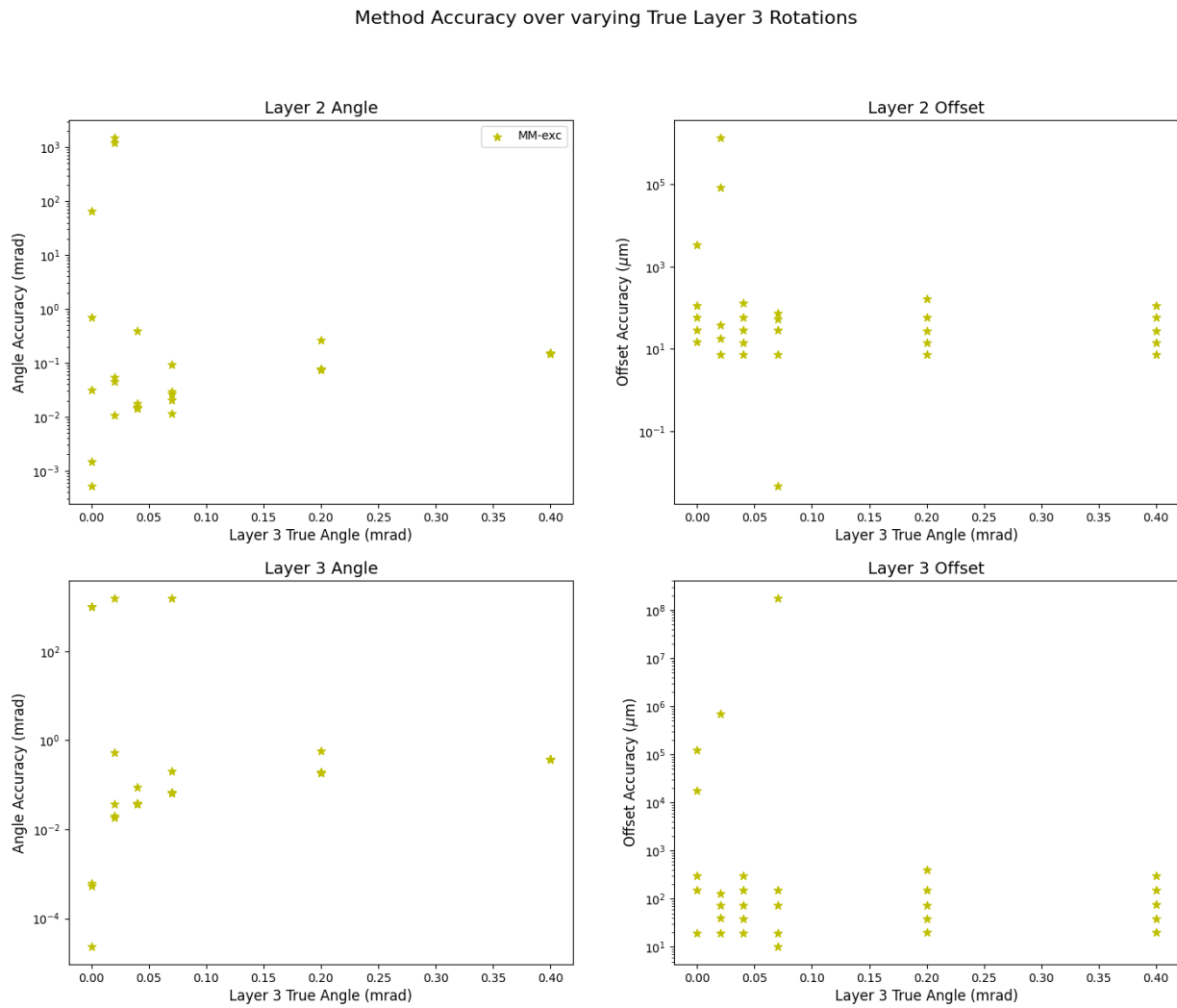


Figure C.2: Semi-log plot of accuracy results from the matrix method using only exclusive residuals. Results span a wide range of magnitudes. Offset version shown in Figure 6.6.

Method Errors over varying True Layer 3 Offsets

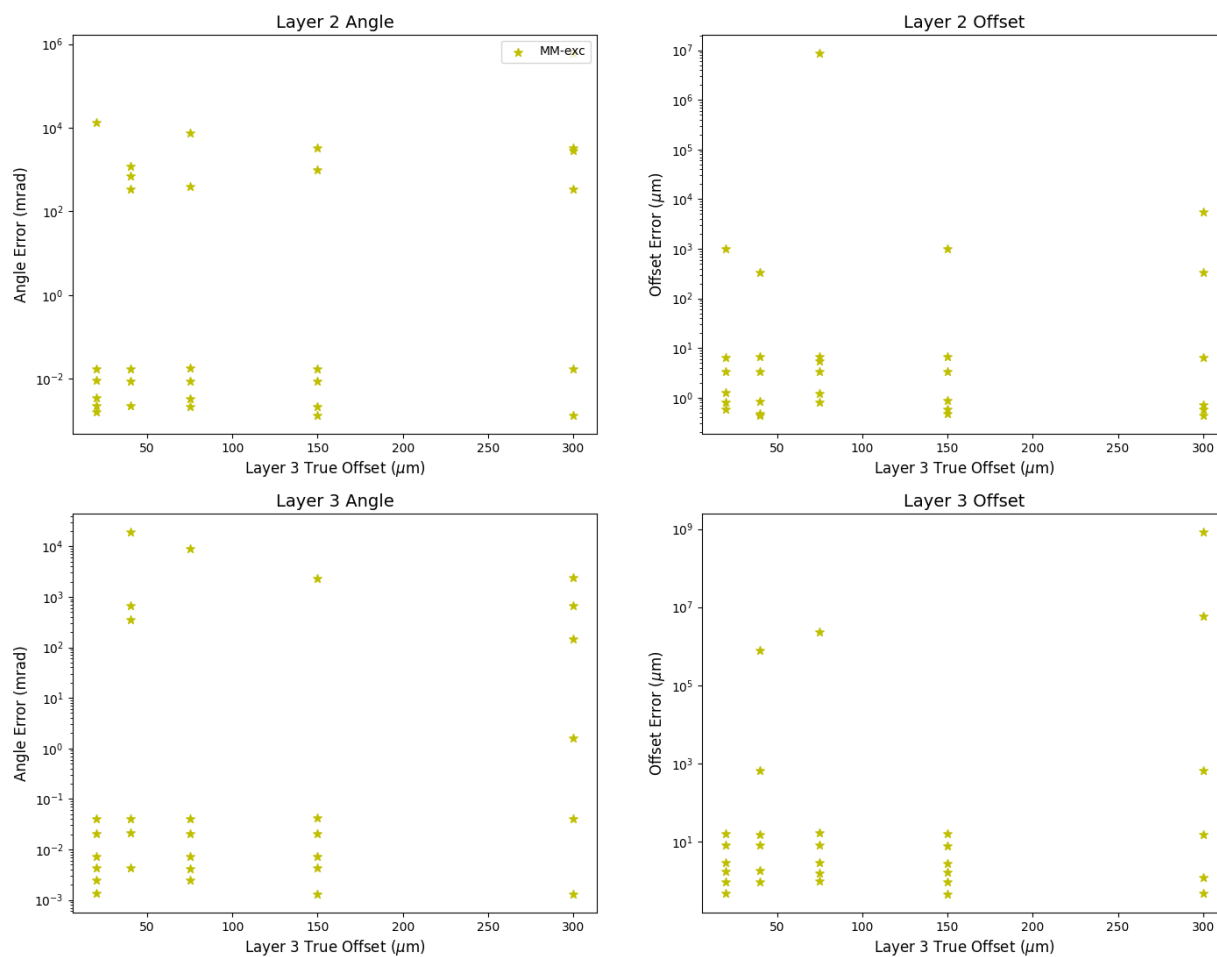


Figure C.3: Semi-log plot of errors from the matrix method using only exclusive residuals. Similar to Figure 6.6, errors span a wide range of magnitudes. Plot with varying true angle in Appendix C.

Method Errors over varying True Layer 3 Rotations

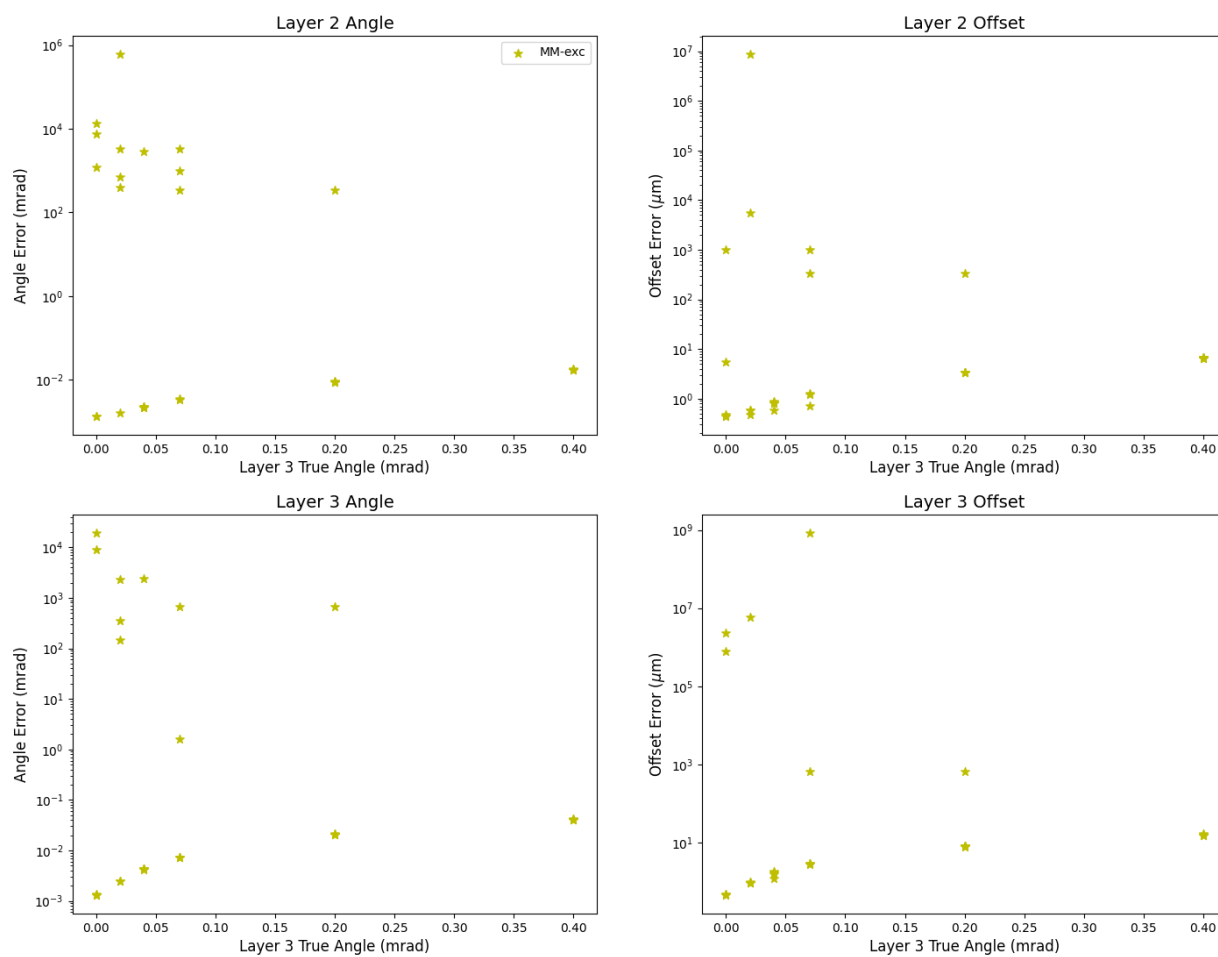


Figure C.4: Semi-log plot of errors from the matrix method using only exclusive residuals. Offset version shown in Figure C.3.

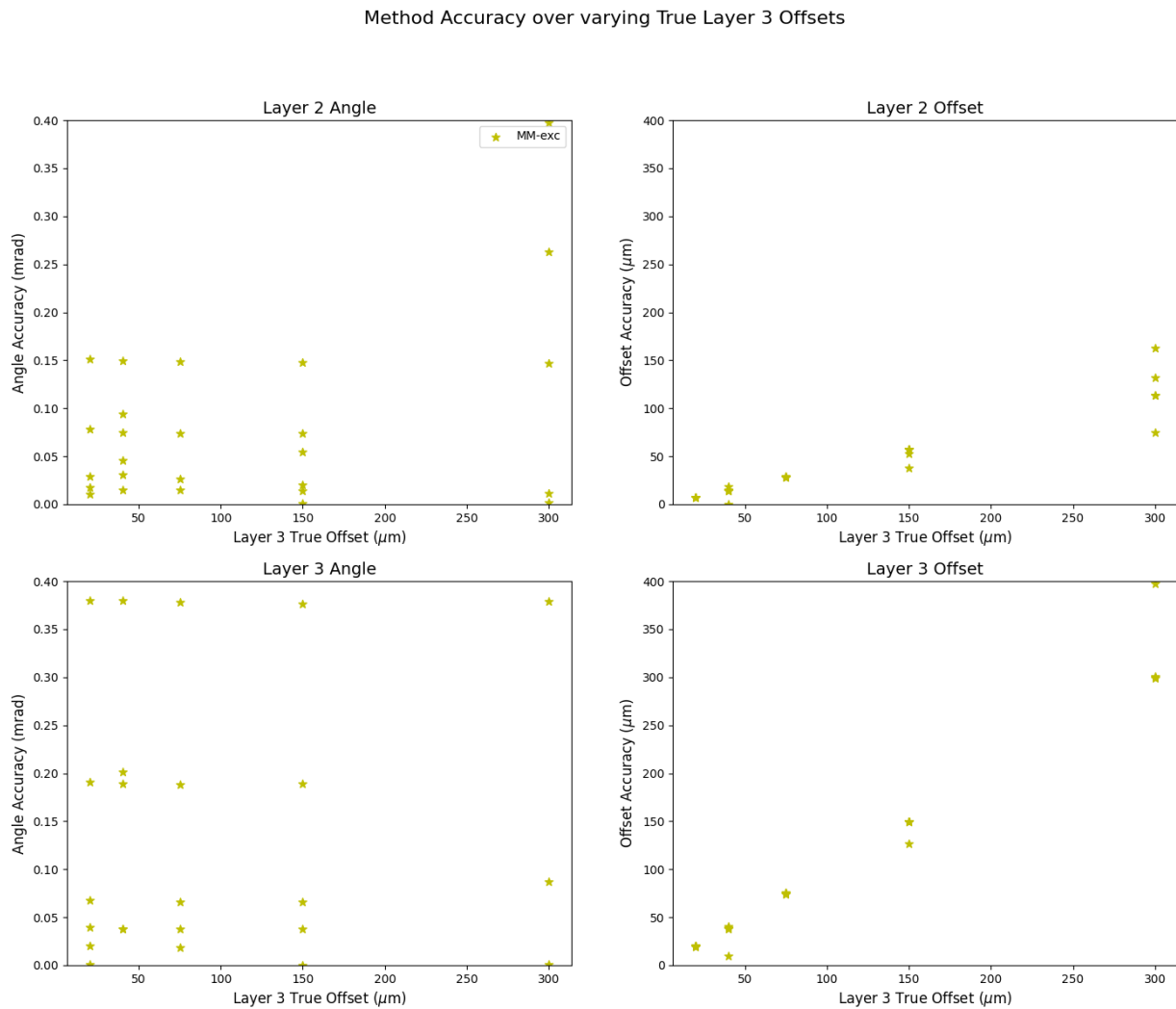


Figure C.5: Re-scaled accuracy results from the matrix method using only exclusive residuals. A linear pattern emerges in Layer 2 and Layer 3 Predictions.

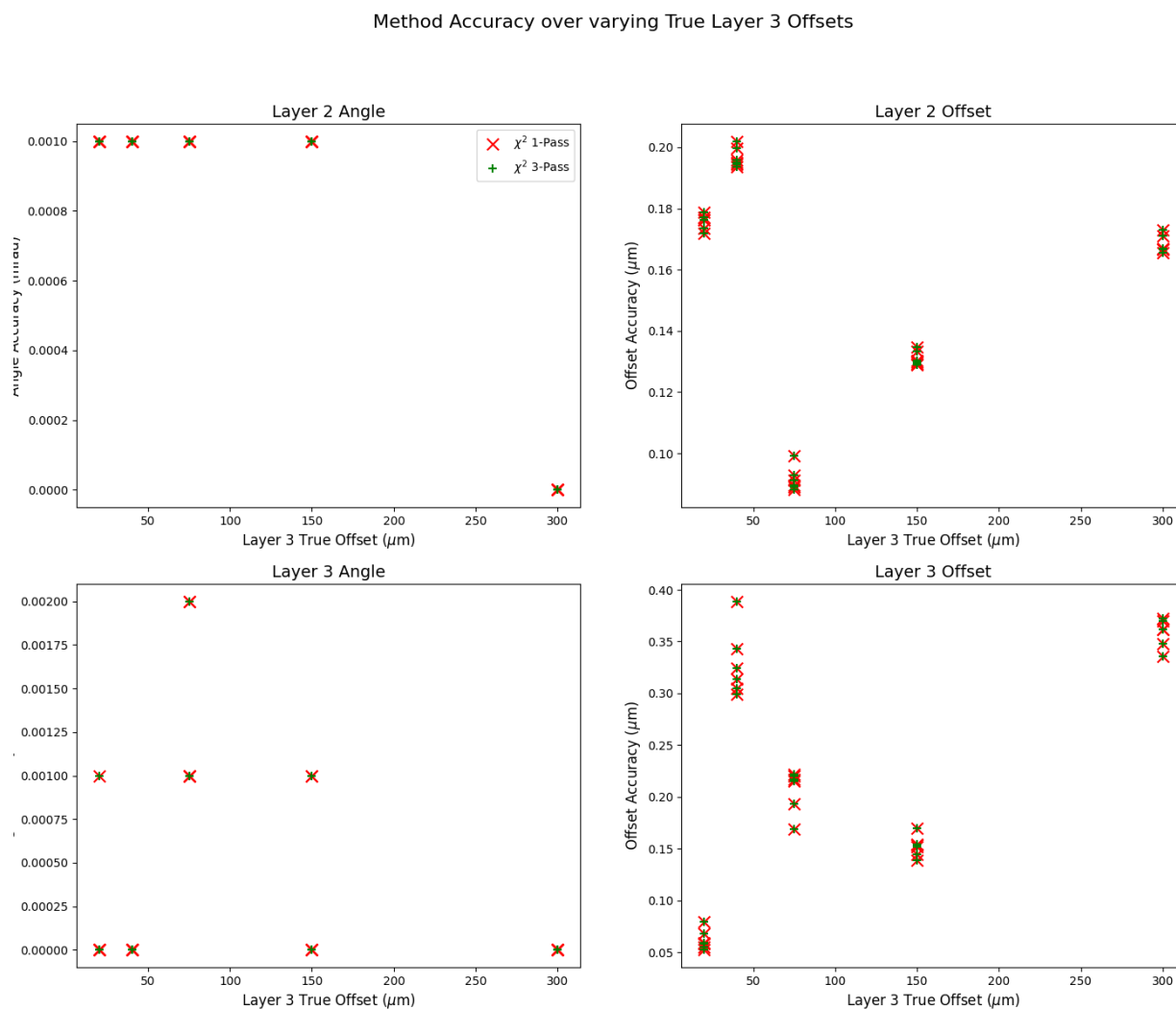


Figure C.6: Accuracy of the χ^2 -based methods over varying Layer 3 offset. Note the complete overlap of the points. Angle version shown in Figure 6.8.

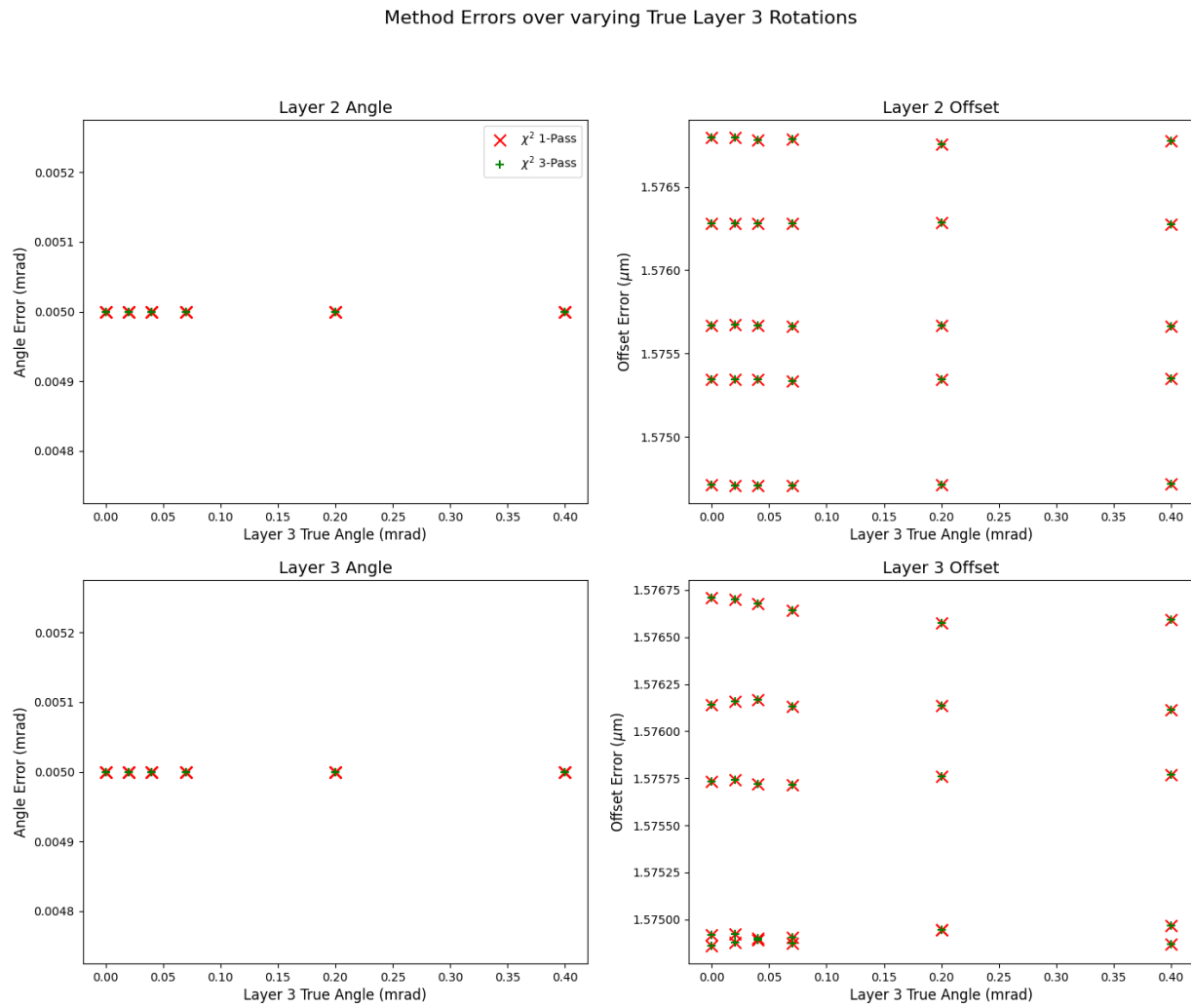


Figure C.7: Errors of the χ^2 -based methods over varying Layer 3 rotation. Similar to Figure 6.8, note the complete overlap of the points. Offset version shown in Figure 6.9.

Method Accuracy over varying True Layer 3 Offsets

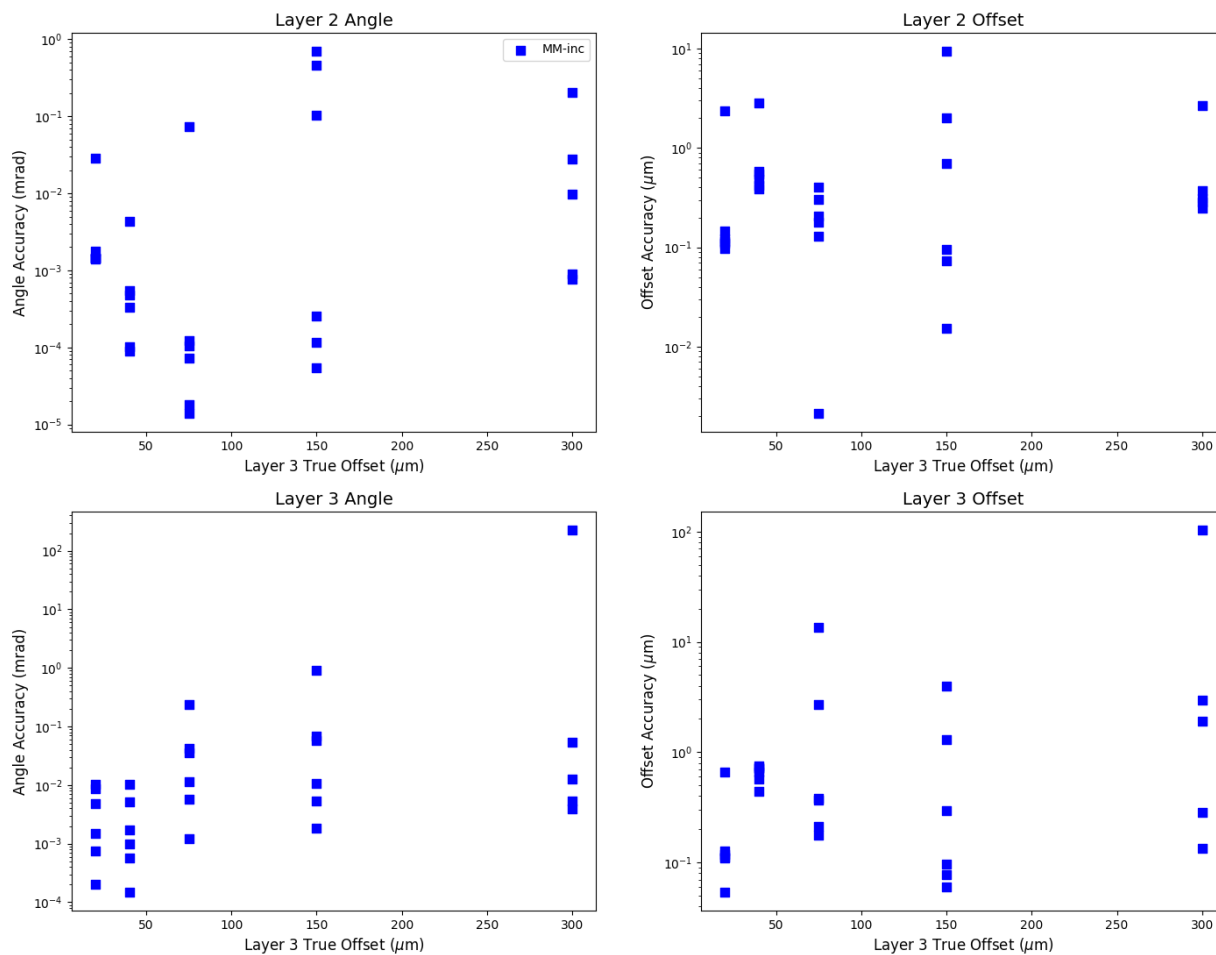


Figure C.8: Accuracy of matrix method using inclusive residuals over varying Layer 3 offset. Comparatively large method absolute differences are mostly present at low angles. Angle version shown in Figure 6.11.

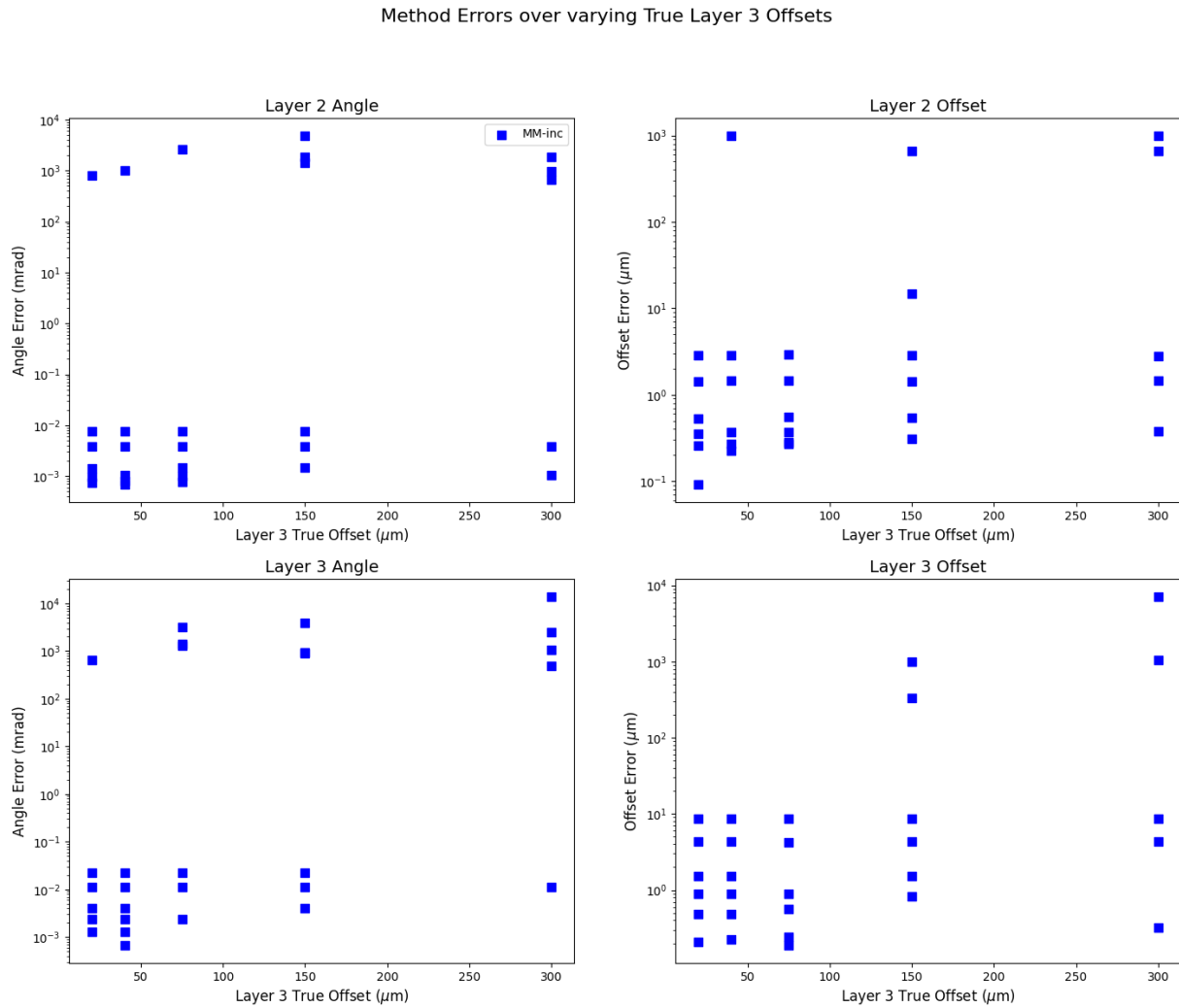


Figure C.9: Errors of the matrix method using inclusive residuals over varying Layer 3 offset. Similar to Figure 6.11, comparatively large method errors are mostly present at low angles. Angle version shown in Figure 6.12.

Bibliography

- [1] MissMJ. *Standard Model of Elementary Particles*. Sept. 2019. URL: https://upload.wikimedia.org/wikipedia/commons/0/00/Standard_Model_of_Elementary_Particles.svg (visited on 10/31/2021).
- [2] A. Zee. *Quantum field theory in a nutshell*. Vol. 7. Princeton university press, 2010.
- [3] M.E. Peskin and D.V. Schroeder. *An Introduction to Quantum Field Theory*. Advanced book classics. Avalon Publishing, 1995. ISBN: 9780201503975. URL: <https://books.google.ca/books?id=i35LALN0GosC>.
- [4] P.A.M. Dirac. “The quantum theory of the electron”. In: *P R Soc. Lond. A-Conta.* 117.778 (1928), pp. 610–624. DOI: 10 . 1098 / rspa . 1928 . 0023. URL: <https://royalsocietypublishing.org/doi/abs/10.1098/rspa.1928.0023>.
- [5] D.J. Griffiths. *Introduction to elementary particles*. John Wiley & Sons, 2020.
- [6] D.J. Griffiths. *Introduction to electrodynamics*. 2005.
- [7] J.D. Jackson. *Classical electrodynamics*. 1999.

- [8] S. Carlip. “Quantum gravity: a progress report”. In: *Rep. Prog. Phys.* 64.8 (July 2001), pp. 885–942. ISSN: 1361-6633. DOI: 10.1088/0034-4885/64/8/301. URL: <http://dx.doi.org/10.1088/0034-4885/64/8/301>.
- [9] . Giesel K and H. Sahlmann. 2013. arXiv: 1203.2733 [gr-qc]. URL: https://www.researchgate.net/publication/221679586_From_Classical_To_Quantum_Gravity_Introduction_to_Loop_Quantum_Gravity.
- [10] T. Thiemann. “Canonical Quantum Gravity, Constructive QFT, and Renormalisation”. In: *Aip. Conf. Proc.* 8 (2020), p. 457. ISSN: 2296-424X. DOI: 10.3389/fphy.2020.548232. URL: <https://www.frontiersin.org/article/10.3389/fphy.2020.548232>.
- [11] K.R. Dienes. “String theory and the path to unification: A review of recent developments”. In: *Phys. Rep.* 287.6 (1997), pp. 447–525. ISSN: 0370-1573. DOI: [https://doi.org/10.1016/S0370-1573\(97\)00009-4](https://doi.org/10.1016/S0370-1573(97)00009-4). URL: <https://www.sciencedirect.com/science/article/pii/S0370157397000094>.
- [12] A. Einstein. “Die Grundlage der allgemeinen Relativitätstheorie”. In: *Ann. Phys.* 354.7 (1916), pp. 769–822. DOI: <https://doi.org/10.1002/andp.19163540702>. eprint: <https://onlinelibrary.wiley.com/doi/pdf/10.1002/andp.19163540702>. URL: <https://onlinelibrary.wiley.com/doi/abs/10.1002/andp.19163540702>.

- [13] R. Webb. *General relativity*. URL: <https://www.newscientist.com/definition/general-relativity/> (visited on 07/15/2021).
- [14] A. Warburton. Personal Communication. Feb. 2, 2021.
- [15] B. Greene. *The elegant universe: Superstrings, hidden dimensions, and the quest for the ultimate theory*. The Folio Society, 2010.
- [16] K. G. Wilson. “Confinement of quarks”. In: *Phys. Rev. D* 10 (8 Oct. 1974), pp. 2445–2459. DOI: 10.1103/PhysRevD.10.2445. URL: <https://link.aps.org/doi/10.1103/PhysRevD.10.2445>.
- [17] N. Cabibbo. “Unitary Symmetry and Leptonic Decays”. In: *Phys. Rev. Lett.* 10 (12 June 1963), pp. 531–533. DOI: 10.1103/PhysRevLett.10.531. URL: <https://link.aps.org/doi/10.1103/PhysRevLett.10.531>.
- [18] M. Kobayashi and T. Maskawa. “CP-Violation in the Renormalizable Theory of Weak Interaction”. In: *Prog. of Theor. Phys.* 49.2 (Feb. 1973), pp. 652–657. ISSN: 0033-068X. DOI: 10.1143/PTP.49.652. eprint: <https://academic.oup.com/ptp/article-pdf/49/2/652/5257692/49-2-652.pdf>. URL: <https://doi.org/10.1143/PTP.49.652>.
- [19] S. W. Herb. “Observation of a Dimuon Resonance at 9.5 GeV in 400-GeV Proton-Nucleus Collisions”. In: *Phys. Rev. Lett.* 39.5 (Jan. 1977). ISSN: 0031-9007. DOI: 10.1103/PhysRevLett.39.252. URL: <https://www.osti.gov/biblio/1155396>.

- [20] F. Abe et al. “Observation of Top Quark Production in $p\bar{p}$ Collisions with the Collider Detector at Fermilab”. In: *Phys. Rev. Lett.* 74.14 (Apr. 1995), pp. 2626–2631. ISSN: 1079-7114. DOI: 10.1103/physrevlett.74.2626. URL: <http://dx.doi.org/10.1103/PhysRevLett.74.2626>.
- [21] Nobel Foundation. *The Nobel Prize in Physics*. 2008. URL: <https://www.nobelprize.org/prizes/physics/2008/summary/> (visited on 07/15/2021).
- [22] *Neutrino (n.)* 2021. URL: <https://www.etymonline.com/word/neutrino> (visited on 07/15/2021).
- [23] J. J. Thomson. “XL. Cathode Rays”. In: *Lond. Edinb. Dubl. Phil. Mag* 44.269 (1897), pp. 293–316. DOI: 10.1080/14786449708621070. URL: <https://doi.org/10.1080/14786449708621070>.
- [24] M. Agostini et al. “Test of Electric Charge Conservation with Borexino”. In: *Phys. Rev. Lett.* 115.23 (Dec. 2015). ISSN: 1079-7114. DOI: 10.1103/physrevlett.115.231802. URL: <http://dx.doi.org/10.1103/PhysRevLett.115.231802>.
- [25] S. H. Neddermeyer and C. D. Anderson. “Note on the Nature of Cosmic-Ray Particles”. In: *Phys. Rev.* 51 (10 May 1937), pp. 884–886. DOI: 10.1103/PhysRev.51.884. URL: <https://link.aps.org/doi/10.1103/PhysRev.51.884>.
- [26] J. C. Street and E. C. Stevenson. “New Evidence for the Existence of a Particle of Mass Intermediate Between the Proton and Electron”. In: *Phys. Rev.* 52 (9 Nov. 1937),

- pp. 1003–1004. DOI: 10.1103/PhysRev.52.1003. URL: <https://link.aps.org/doi/10.1103/PhysRev.52.1003>.
- [27] P. A. et al. Zyla. “Review of Particle Physics”. In: *Prog. of Theor. and Exp. Phys.* 2020.8 (Aug. 2020). 083C01. ISSN: 2050-3911. DOI: 10.1093/ptep/ptaa104. eprint: <https://academic.oup.com/ptep/article-pdf/2020/8/083C01/34673722/ptaa104.pdf>. URL: <https://doi.org/10.1093/ptep/ptaa104>.
- [28] “Detailed report of the MuLan measurement of the positive muon lifetime and determination of the Fermi constant”. In: *Phys. Rev. D* 87 (5 Mar. 2013), p. 052003. DOI: 10.1103/PhysRevD.87.052003. URL: <https://link.aps.org/doi/10.1103/PhysRevD.87.052003>.
- [29] M. L. et al. Perl. “Evidence for Anomalous Lepton Production in $e^+ - e^-$ Annihilation”. In: *Phys. Rev. Lett.* 35 (22 Dec. 1975), pp. 1489–1492. DOI: 10.1103/PhysRevLett.35.1489. URL: <https://link.aps.org/doi/10.1103/PhysRevLett.35.1489>.
- [30] “Measurement of the τ -lepton Lifetime at Belle”. In: *Phys. Rev. Lett.* 112 (3 Jan. 2014), p. 031801. DOI: 10.1103/PhysRevLett.112.031801. URL: <https://link.aps.org/doi/10.1103/PhysRevLett.112.031801>.
- [31] T. Kajita. “Atmospheric neutrino results from Super-Kamiokande and Kamiokande — Evidence for $\nu - \mu$ oscillations”. In: *Nucl. Phys. B* 77.1 (1999), pp. 123–132. ISSN:

- 0920-5632. DOI: [https://doi.org/10.1016/S0920-5632\(99\)00407-7](https://doi.org/10.1016/S0920-5632(99)00407-7). URL: <https://www.sciencedirect.com/science/article/pii/S0920563299004077>.
- [32] “Direct Evidence for Neutrino Flavor Transformation from Neutral-Current Interactions in the Sudbury Neutrino Observatory”. In: *Phys. Rev. Lett.* 89 (1 June 2002), p. 011301. DOI: 10.1103/PhysRevLett.89.011301. URL: <https://link.aps.org/doi/10.1103/PhysRevLett.89.011301>.
- [33] M. Aker et al. “Improved Upper Limit on the Neutrino Mass from a Direct Kinematic Method by KATRIN”. In: *Phys. Rev. Lett.* 123.22 (Nov. 2019). ISSN: 1079-7114. DOI: 10.1103/physrevlett.123.221802. URL: <http://dx.doi.org/10.1103/PhysRevLett.123.221802>.
- [34] “Improved Upper Limit on the Neutrino Mass from a Direct Kinematic Method by KATRIN”. In: *Phys. Rev. Lett.* 123 (22 Nov. 2019), p. 221802. DOI: 10.1103/PhysRevLett.123.221802. URL: <https://link.aps.org/doi/10.1103/PhysRevLett.123.221802>.
- [35] F.J. Ynduráin. “Limits on the mass of the gluon”. In: *Phys. Lett. B* 345.4 (1995), pp. 524–526. ISSN: 0370-2693. DOI: [https://doi.org/10.1016/0370-2693\(94\)01677-5](https://doi.org/10.1016/0370-2693(94)01677-5). URL: <https://www.sciencedirect.com/science/article/pii/0370269394016775>.

- [36] D. D. Ryutov. “Using plasma physics to weigh the photon”. In: 49.12B (Nov. 2007), B429–B438. DOI: 10.1088/0741-3335/49/12b/s40. URL: <https://doi.org/10.1088/0741-3335/49/12b/s40>.
- [37] et al. Abbiendi G. “Precise determination of the Z resonance parameters at LEP: “Zedometry””. In: *Eur. Phys. J. C* 19.4 (Mar. 2001), pp. 587–651. ISSN: 1434-6052. DOI: 10.1007/s100520100627. URL: <http://dx.doi.org/10.1007/s100520100627>.
- [38] F. Englert and R. Brout. “Broken Symmetry and the Mass of Gauge Vector Mesons”. In: *Phys. Rev. Lett.* 13 (9 Aug. 1964), pp. 321–323. DOI: 10.1103/PhysRevLett.13.321. URL: <https://link.aps.org/doi/10.1103/PhysRevLett.13.321>.
- [39] P. W. Higgs. “Broken Symmetries and the Masses of Gauge Bosons”. In: *Phys. Rev. Lett.* 13 (16 Oct. 1964), pp. 508–509. DOI: 10.1103/PhysRevLett.13.508. URL: <https://link.aps.org/doi/10.1103/PhysRevLett.13.508>.
- [40] “Observation of a new boson at a mass of 125 GeV with the CMS experiment at the LHC”. In: *Phys. Lett. B* 716.1 (2012), pp. 30–61. ISSN: 0370-2693. DOI: <https://doi.org/10.1016/j.physletb.2012.08.021>. URL: <https://www.sciencedirect.com/science/article/pii/S0370269312008581>.
- [41] “Observation of a new particle in the search for the Standard Model Higgs boson with the ATLAS detector at the LHC”. In: *Phys. Lett. B* 716.1 (2012), pp. 1–29. ISSN:

- 0370-2693. DOI: <https://doi.org/10.1016/j.physletb.2012.08.020>. URL: <https://www.sciencedirect.com/science/article/pii/S037026931200857X>.
- [42] Nobel Foundation. *The Nobel Prize in Physics*. 2013. URL: <https://www.nobelprize.org/prizes/physics/2013/summary/> (visited on 07/15/2021).
- [43] Garyzx. *Standard Model Interactions (Forces Mediated by Gauge Bosons)*. May 2011. URL: https://commons.wikimedia.org/wiki/File:Standard_Model_Feynman_Diagram_Vertices.png (visited on 10/31/2021).
- [44] Lord Rayleigh. “XXXIV. On the transmission of light through an atmosphere containing small particles in suspension, and on the origin of the blue of the sky”. In: *Lond. Edinb. Dubl. Phil. Mag.* 47.287 (1899), pp. 375–384. DOI: 10.1080/14786449908621276. eprint: <https://doi.org/10.1080/14786449908621276>. URL: <https://doi.org/10.1080/14786449908621276>.
- [45] A. H. Compton. “A Quantum Theory of the Scattering of X-rays by Light Elements”. In: *Phys. Rev.* 21 (5 May 1923), pp. 483–502. DOI: 10.1103/PhysRev.21.483. URL: <https://link.aps.org/doi/10.1103/PhysRev.21.483>.
- [46] C. Grupen and B. Shwartz. *Particle Detectors*. 2nd ed. Cambridge Monographs on Particle Physics, Nuclear Physics and Cosmology. Cambridge University Press, 2008. DOI: 10.1017/CB09780511534966.

- [47] A. Powell. *Particle Identification at LHCb. Particle ID in LHCb*. Tech. rep. Jan. 2011, 5 p. URL: <https://cds.cern.ch/record/1322666>.
- [48] J. Caravaca et al. “Characterization of water-based liquid scintillator for Cherenkov and scintillation separation”. In: *Euro. Phys. J. C* 80.9 (2020), pp. 1–10. DOI: 10.1140/epjc/s10052-020-8418-4. URL: <https://link.springer.com/article/10.1140/epjc/s10052-020-8418-4>.
- [49] Th. et al. Siedenburg. “A transition radiation detector for AMS”. In: *Nuc. Phys. B* 113.1 (2002), pp. 154–158. ISSN: 0920-5632. DOI: [https://doi.org/10.1016/S0920-5632\(02\)01835-2](https://doi.org/10.1016/S0920-5632(02)01835-2). URL: <https://www.sciencedirect.com/science/article/pii/S0920563202018352>.
- [50] Michael Schmid. *Electron avalanche*. Dec. 2005. URL: https://upload.wikimedia.org/wikipedia/commons/a/ac/Electron_avalanche.gif (visited on 10/31/2021).
- [51] A. von Engel. “John Sealy Edward Townsend, 1868-1957”. In: *Biographical Memoirs of Fellows of the Royal Society* 3 (1957), pp. 256–272. DOI: 10.1098/rsbm.1957.0018. URL: <https://royalsocietypublishing.org/doi/abs/10.1098/rsbm.1957.0018>.
- [52] K. Kleinknecht. *Detectors for particle radiation*. Cambridge University Press, 1998.
- [53] H. Friedman. “Geiger Counter Tubes”. In: *Proceedings of the IRE* 37.7 (July 1974), pp. 791–808. DOI: 10.1109/JRPROC.1949.234614. URL: <https://ieeexplore.ieee.org/abstract/document/1698087>.

- [54] Doug Sim. *Detector regions*. June 2012. URL: https://upload.wikimedia.org/wikipedia/commons/f/f7/Detector_regions.gif (visited on 10/31/2021).
- [55] G. Charpak et al. “The use of multiwire proportional counters to select and localize charged particles”. In: *Nucl. Instrum. Methods* 62.3 (1968), pp. 262–268. ISSN: 0029-554X. DOI: [https://doi.org/10.1016/0029-554X\(68\)90371-6](https://doi.org/10.1016/0029-554X(68)90371-6). URL: <https://www.sciencedirect.com/science/article/pii/0029554X68903716>.
- [56] Doug Sim. *Wire chamber schematic*. Oct. 2012. URL: https://commons.wikimedia.org/wiki/File:Wire_chamber_schematic.svg (visited on 10/31/2021).
- [57] W. Riegler. *Detector physics and performance: simulations of the MWPCs for the LHCb muon system*. Tech. rep. CERN-LHCb-2000-060, 2000.
- [58] B. Vachon. *Tracking Detectors - PHYS 620*. Feb. 2019.
- [59] G. Charpak, Rahm D., and Steiner H. “Some developments in the operation of multiwire proportional chambers”. In: *Nucl. Instrum. Meth.* 80.1 (1970), pp. 13–34. ISSN: 0029-554X. DOI: [https://doi.org/10.1016/0029-554X\(70\)90293-4](https://doi.org/10.1016/0029-554X(70)90293-4). URL: <https://www.sciencedirect.com/science/article/pii/0029554X70902934>.
- [60] K. Han. “Experimental Tools I: Radiation Detectors”. In: *Encyclopedia of Nuclear Energy*. Ed. by Ehud Greenspan. Oxford: Elsevier, 2021, pp. 133–145. ISBN: 978-0-12-819732-5. DOI: <https://doi.org/10.1016/B978-0-12-819725-7.00057-X>. URL: <https://www.sciencedirect.com/science/article/pii/B978012819725700057X>.

- [61] R. Hofstadter. “The Detection of Gamma-Rays with Thallium-Activated Sodium Iodide Crystals”. In: *Phys. Rev.* 75 (5 Mar. 1949), pp. 796–810. DOI: 10.1103/PhysRev.75.796. URL: <https://link.aps.org/doi/10.1103/PhysRev.75.796>.
- [62] F. Suekane et al. “An overview of the KamLAND 1-kiloton liquid scintillator”. In: *arXiv preprint physics/0404071* (2004). URL: <https://arxiv.org/abs/physics/0404071>.
- [63] G.C. Ball et al. “High-resolution γ -ray spectroscopy: a versatile tool for nuclear β -decay studies at TRIUMF-ISAC”. In: *J. Phys. G Nucl. Partic.* 31.10 (2005), S1491. DOI: 10.1088/0954-3899/31/10/019. URL: <https://doi.org/10.1088/0954-3899/31/10/019>.
- [64] E. Aprile et al. *Noble gas detectors*. John Wiley & Sons, 2006.
- [65] R. Hakamata et al. “Photomultiplier tubes: basics and applications”. In: *Hamamatsu Photonics KK Electron Tube Division, Hamamatsu City* (2006).
- [66] Qwerty123uiop. *PhotoMultiplierTubeAndScintillator*. Nov. 2013. URL: <https://upload.wikimedia.org/wikipedia/commons/e/e8/PhotoMultiplierTubeAndScintillator.svg> (visited on 10/31/2021).
- [67] R. Allen. “The Higgs Bridge”. In: *Phys. Scripta* 89 (Nov. 2013). DOI: 10.1088/0031-8949/89/01/018001. URL: <https://iopscience.iop.org/article/10.1088/0031-8949/89/01/018001/meta>.

- [68] The ATLAS Collaboration. “The ATLAS experiment at the CERN Large Hadron Collider”. In: *J. Inst* 3 (2008), S08003. DOI: 10.1088/1748-0221/3/08/S08003. URL: <http://hal.in2p3.fr/in2p3-00315956>.
- [69] The CMS Collaboration. “The CMS experiment at the CERN LHC”. In: *J. Inst* 3 (2008). DOI: 10.1088/1748-0221/3/08/S08004. URL: <https://www.diva-portal.org/smash/record.jsf?pid=diva2%5C%3A1272639&dswid=-8587>.
- [70] The LHCb Collaboration. “The LHCb Detector at the LHC”. In: *J. Inst* 3.08 (Aug. 2008), S08005–S08005. DOI: 10.1088/1748-0221/3/08/s08005. URL: <https://doi.org/10.1088/1748-0221/3/08/s08005>.
- [71] The ALICE Collaboration. “The ALICE experiment at the CERN LHC”. In: *J. Inst* 3.08 (Aug. 2008), S08002–S08002. DOI: 10.1088/1748-0221/3/08/s08002. URL: <https://doi.org/10.1088/1748-0221/3/08/s08002>.
- [72] Collaboration, ATLAS. “The ATLAS Experiment at the CERN Large Hadron Collider”. In: *J. Inst* 3 (2008). Also published by CERN Geneva in 2010, S08003. 437 p. DOI: 10.1088/1748-0221/3/08/S08003. URL: <https://cds.cern.ch/record/1129811>.
- [73] ATLAS Collaboration. “Studies of the performance of the ATLAS detector using cosmic-ray muons”. In: *Eur. Phys. J. C* 71 (Nov. 2010), pp. 1–36. DOI:

- 10 . 1140 / epjc / s10052 - 011 - 1593 - 6. URL:
<http://dx.doi.org/10.1140/epjc/s10052-011-1593-6>.
- [74] T. Kawamoto et al. *New Small Wheel Technical Design Report*. Tech. rep. ATLAS New Small Wheel Technical Design Report. June 2013. URL: <https://cds.cern.ch/record/1552862>.
- [75] URL: <https://project-hl-lhc-industry.web.cern.ch/content/project-schedule> (visited on 10/31/2021).
- [76] CERN. *CERN Council updates European strategy for particle physics*. May 30, 2013. URL: <https://home.cern/news/news/cern/cern-council-updates-european-strategy-particle-physics> (visited on 07/15/2021).
- [77] M. Raymond. *ATLAS Upgrades : Plans for LS2 and LS3*. Oct. 3, 2015. URL: https://www.google.com/url?sa=t&rct=j&q=&esrc=s&source=web&cd=&ved=2ahUKEwi12tOH8-XxAhXG-J4KHTJlAXkQFjAAegQIBhAD&url=https%5C%3A%5C%2F%5C%2Ffindico.cern.ch%5C%2Fevent%5C%2F524795%5C%2Fcontributions%5C%2F2235423%5C%2Fattachments%5C%2F1346805%5C%2F2031074%5C%2FECFA_2016.pdf&usq=A0vVaw3fZpx01KZMhy3b0SUuyubB (visited on 11/12/2020).
- [78] W. Buttinger. “The ATLAS Level-1 Trigger System”. In: 396.1 (Dec. 2012), p. 012010. DOI: 10.1088/1742-6596/396/1/012010. URL: <https://doi.org/10.1088/1742-6596/396/1/012010>.

- [79] Y. Giomataris et al. “MICROMEAS: a high-granularity position-sensitive gaseous detector for high particle-flux environments”. In: *Nucl. Instrum. Meth. A* 376.1 (1996), pp. 29–35. ISSN: 0168-9002. DOI: [https://doi.org/10.1016/0168-9002\(96\)00175-1](https://doi.org/10.1016/0168-9002(96)00175-1). URL: <https://www.sciencedirect.com/science/article/pii/0168900296001751>.
- [80] M. Bianco. “Micromegas detectors for the muon spectrometer upgrade of the ATLAS experiment”. In: *Nucl. Instrum. Meth. A* 824 (2016). Frontier Detectors for Frontier Physics: Proceedings of the 13th Pisa Meeting on Advanced Detectors, pp. 496–500. ISSN: 0168-9002. DOI: <https://doi.org/10.1016/j.nima.2015.11.076>. URL: <https://www.sciencedirect.com/science/article/pii/S0168900215014503>.
- [81] S. Majewski et al. “A thin multiwire chamber operating in the high multiplication mode”. In: *Research On Particle Imaging Detectors*. World Scientific, 1995, pp. 185–191.
- [82] Xilinx. *Xilinx Kintex-7 FPGA KC705 Evaluation Kit*. URL: <https://www.xilinx.com/products/boards-and-kits/ek-k7-kc705-g.html> (visited on 10/31/2021).
- [83] B. Lefebvre. “Characterization studies of small-strip Thin Gap Chambers for the ATLAS Upgrade”. PhD thesis. McGill University (Canada), 2019.
- [84] R. Keyes et al. “Development and characterisation of a gas system and its associated slow-control system for an ATLAS small-strip thin gap chamber testing facility”. In:

- J. Inst* 12.04 (Apr. 2017), P04027–P04027. DOI: 10.1088/1748-0221/12/04/p04027.
URL: <https://doi.org/10.1088/1748-0221/12/04/p04027>.
- [85] R. Bitter, T. Mohiuddin, and M. Nawrocki. *LabVIEW: Advanced programming techniques*. CRC press, 2000.
- [86] E. V. Bugaev et al. “Atmospheric muon flux at sea level, underground, and underwater”. In: *Phys. Rev. D* 58 (5 July 1998), p. 054001. DOI: 10.1103/PhysRevD.58.054001. URL: <https://link.aps.org/doi/10.1103/PhysRevD.58.054001>.
- [87] NSW sTGC Lab at McGill. lab handbook. Apr. 6, 2019. URL: <https://docs.google.com/document/d/17TAw41BRmsOEAx1a4U1IkowbyT6Qo8aWQvdbSrnXLh0/edit?usp=sharing>.
- [88] R. et al. Brun. *root-project/root: v6.18/02*. Version v6-18-02. Aug. 2019. DOI: 10.5281/zenodo.3895860. URL: <https://doi.org/10.5281/zenodo.3895860>.
- [89] X. Zhao et al. “Cosmic test of sTGC detector prototype made in China for ATLAS experiment upgrade”. In: *Nucl. Instrum. Meth. A* 927 (2019), pp. 257–261. ISSN: 0168-9002. DOI: <https://doi.org/10.1016/j.nima.2019.02.061>. URL: <https://www.sciencedirect.com/science/article/pii/S016890021930244X>.
- [90] L. Formenti. Personal Communication. Aug. 10, 2021.